UM-HE-90-38

PRODUCTION POLARIZATION AND MAGNETIC MOMENT OF ANTI-CASCADE MINUS HYPERON PRODUCED BY 800 GeV/c PROTONS

by

Pak-Ming Ho

A dissertation submitted in partial fulfillment
of the requirements for the degree of
Doctor of Philosophy
(Physics)
in The University of Michigan
1990

Doctoral Committee:

Professor Michael J. Longo, Chairman
Associate Professor Ratindranath Akhoury
Professor Frederick Becchetti
Associate Professor Mary Brake
Professor J. Wehrley Chapman

DEDICATION

To my parents, for their love and their unreserved supports.

ACKNOWLEDGMENTS

I would like first to thank my thesis adviser, Michael Longo, who has introduced me to experimental high energy physics and who has guided me to become a solid physicist. I will aim at this goal for the rest of my physics career.

Without the effort of a team of people, experimental high energy research is impossible to carry out. It was a great pleasure to work with Kam-Biu Luk. I have learned and appreciated much from his enthusiasm about physics, and his ability and unique style to solve a problem. Gina Rameika's contribution to keep the beam line operating smoothly was indispensable to the experiment. I always enjoy the discussion with Ken Heller and find his advice valuable. I would like to thank Bob Handler for the continuous consultation of his reconstruction program. Special thanks also due to Chien-Peng Yuan from whom I have learnt much about physics. It was a valuable experience to work with T. Diehl, J. Duryea, C. James, K. Johns, S. Teige and G. Thomson. I gratefully acknowledge the cooperation of all the operators in the computing department at Fermilab. Thank you all.

Friendship makes my academic life completed. I wish to thank Kam-Biu and his wife, Po-Ling, for their hospitality when I just moved to Fermilab three and a half years ago. Later on, their friendship makes these years enjoyable. The same gratitude goes to Chien-Peng and his wife. I would like to thank Shirley Bryar, who taught me drawing and led me to appreciate the western art. Many thanks also go to the Nguyen's family, An and all his brothers and their parents. I feel like home whenever I come back to Ann Arbor since I moved to Fermilab.

Finally, I greatly appreciate my sister, Mei-Lin, for her consideration, love, and care of our family while I was in graduate school, and letting me concentrate on my study. Without the unreserved supports from my parents and their thoughtful attention to my wish, I would not be able to finish my education in the United States. They know nothing about science, but they are the generators of this work.

TABLE OF CONTENTS

LIST OF TABLES

Tables

LIST OF FIGURES

CHAPTER 1

INTRODUCTION

In 1976 it was shown that Λ hyperons are substantially polarized when produced in the reaction $p + Be \rightarrow \Lambda + X$, where X represents unobserved particles.[1] It was a surprising discovery since polarization effects were believed to be washed out at high energy and small transverse momentum. It indicated that important spin effects exist in high energy collisions. Later on, polarization of comparable magnitude was also found in inclusive production of Σ^0, Σ^+, Σ^-, Ξ^0, and Ξ^- hyperons by protons.[2-9] On the contrary, the polarization of $\overline{\Lambda}$ was found to be consistent with zero.[10-12] The polarization of $\overline{\Xi}^0$ was inconclusive.[13] Models based on the recombination of valence quarks in the projectile with quarks from the sea to form the hyperon can explain the qualitative behavior of the data.[14-16] These models also predict no polarization for particles that do not share any valence quarks with the incoming particle, for example, anti-hyperons such as $\overline{\Xi}^+$.

In the experiment described here at Fermilab, we have discovered that $\overline{\Xi}^+$'s produced by protons have a polarization approximately equal to that of the Ξ^-. The presence of a significant polarization for the $\overline{\Xi}^+$ made possible the first measurement of the magnetic moment of an anti-hyperon.

1.1 Polarization

In general, polarization is defined as the net projection of the spin of a particle, averaged over a whole sample, with respect to a quantization axis. If **P** is the polarization vector and P is the component along such an axis, then

$$\mathbf{P} = \langle \mathbf{S} \rangle$$
$$P = \langle \mathbf{S} \cdot \hat{\mathbf{e}} \rangle \qquad (1.1)$$

where **S** is the spin of the particle, $\hat{\mathbf{e}}$ is the unit vector along the quantization axis and $\langle\ \rangle$ means the expectation value. In the case of a spin 1/2 particle,

$$P = \frac{N_{\uparrow} - N_{\downarrow}}{N_{\uparrow} + N_{\downarrow}} \qquad (1.2)$$

where $N_{\uparrow}$ and $N_{\downarrow}$ are the number of particles with spin parallel and anti-parallel to $\hat{\mathbf{e}}$ respectively.

In our case, the reaction of interest was, p + Be $\rightarrow$ B + X, where p is the incoming proton, B is the outgoing hyperon, and Be is a beryllium target nuclei. In Figure 1.1, $\vec{p}_{\text{beam}}$ and $\vec{p}_{\text{hyperon}}$ are the momenta of the beam proton and the produced hyperon respectively. Protons hit the target at an angle with respect to the z-axis, and $\vec{p}_{\text{hyperon}}$ lies along this axis. This angle is defined as the production angle. The production plane is defined by $\vec{p}_{\text{beam}}$ and $\vec{p}_{\text{hyperon}}$, which is the yz-plane; and x, y, z form a right handed coordinate system. The production normal $\hat{\mathbf{n}}$ is defined as $\vec{p}_{\text{beam}} \times \vec{p}_{\text{hyperon}} / |\vec{p}_{\text{beam}} \times \vec{p}_{\text{hyperon}}|$.

For particles produced in strong interactions, the polarization vector must be normal to the production plane as required by parity conservation. According to the definition $P = \langle \mathbf{S} \cdot \hat{\mathbf{e}} \rangle$, terms like $\langle \mathbf{S} \cdot \hat{\mathbf{y}} \rangle$ violate parity conservation since $\hat{\mathbf{y}}$ is a vector and **S** is a pseudovector under the parity operation $x \rightarrow -x$. On the other

hand, $\langle \mathbf{S} \cdot \hat{\mathbf{n}} \rangle = \langle \mathbf{S} \cdot (\frac{\vec{p}_{\text{beam}} \times \vec{p}_{\text{hyperon}}}{|\vec{p}_{\text{beam}} \times \vec{p}_{\text{hyperon}}|}) \rangle$ is parity conserving since $\hat{\mathbf{n}}$ is now a pseudovector. Thus in order to conserve parity in strong interactions, the polarization vector can have a non-zero component only normal to the production plane, namely,

$$P = \langle \mathbf{S} \cdot (\frac{\vec{p}_{\text{beam}} \times \vec{p}_{\text{hyperon}}}{|\vec{p}_{\text{beam}} \times \vec{p}_{\text{hyperon}}|}) \rangle \qquad (1.3)$$

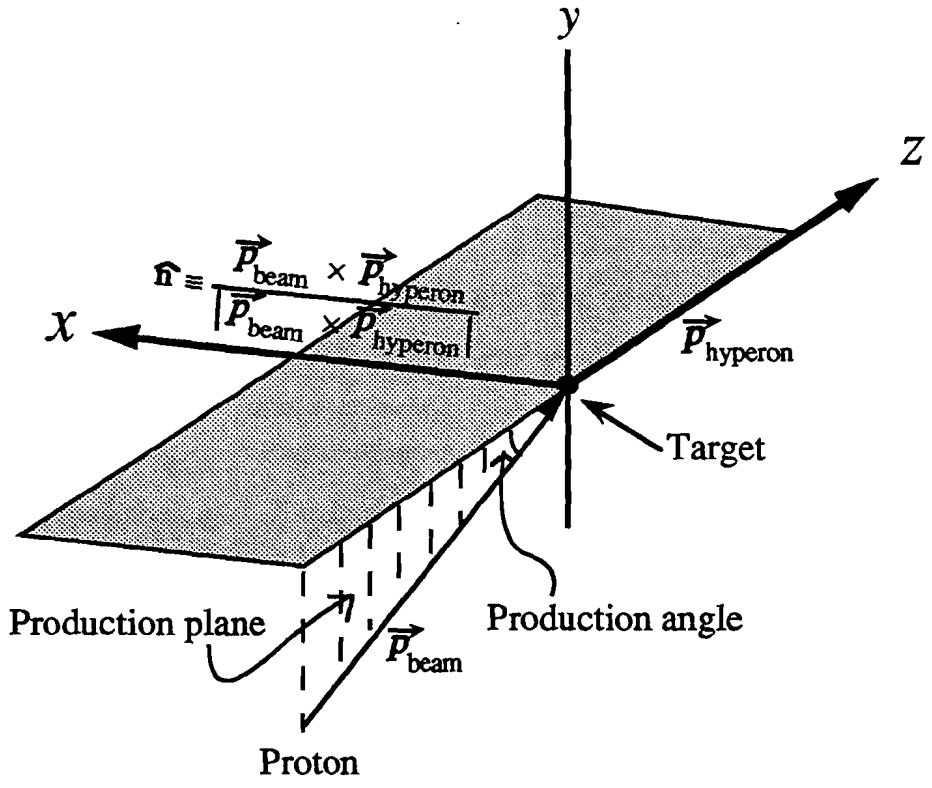

Figure 1.1 Polarization at target.

1.2 Sign Convention for Polarization

The sign of polarization is defined as follows :

" + " polarization if $\mathbf{P}$ is parallel to $+\hat{n}$

" - " polarization if $\mathbf{P}$ is parallel to $-\hat{n}$

" + " production angle if $\hat{n}$ is parallel to $+\hat{x}$

" - " production angle if $\hat{n}$ is parallel to $-\hat{x}$

It is important to point out that the polarization vector will flip sign if the production angle is reversed by a simple symmetry requirement. For example, if P = -0.1 at an production angle = +2.4 mrad, then P = 0.1 for -2.4 mrad. This sign flip of polarization allows the cancellation of biases in the polarization measurement so that the real signal can be extracted.

1.3 Hyperon Production Polarization

Before the discovery of the Λ production polarization, physicists believed that polarization effects would disappear at high energy, say a few GeV. The reasons for this are as follows. First, polarization is a coherent effect, which depends on the amplitudes and phases of the final states. High energy means more possible amplitudes (final states), each with a different phase. Thus polarization decreases because of the increase of incoherent final states. Second, Regge theory, which explained the phenomena at low energies and transverse momentum rather successfully while perturbative QCD failed at this energy regime, also predicted insignificant polarization at high energy.[17]

In 1976, a Fermilab experiment[1] discovered that the Λ hyperon had substantial polarization in $p + Be \rightarrow \Lambda + X$ at 300 GeV/c. It had a negative polarization and increased roughly linearly up to p_t=1.5 GeV/c. This was a surprise because it contradicted what high energy physicists thought about polarization. Two years later, another interesting result came out. In the reaction $p + Be \rightarrow \overline{\Lambda} + X$ at 400 GeV/c, the

polarization of $\overline{\Lambda}$ was consistent with zero.[10] Figure 1.2 shows the comparison of the polarization of Λ and $\overline{\Lambda}$.[10] Since then a great experimental effort has been made in exploring the kinematic dependence of the polarization and searching for similar behaviour in the inclusive production of other hadrons. Experimental data show that polarization is not unique to Λ, but is a rather universal feature of hyperons produced by protons. It has been found that Σ^0, Σ^+, Σ^-, Ξ^0, and Ξ^- produced by protons were all polarized,[2-9] with comparable magnitudes; however the Σ's have opposite sign from the Ξ's. Polarization generally increases with x_F and p_t. x_F is defined as P^*_L/P^*_{max}, where P^*_L is the hyperon momentum parallel to the projectile incident momentum and P^*_{max} is the maximum possible value of that momentum in the center of mass frame. At high energy $x_F \approx P_{hyperon}/P_{inc.proton}$, where $P_{hyperon}$ and $P_{inc.proton}$ are the momenta of the outgoing hyperon and the incident proton in the lab frame. p_t is the transverse momentum of the hyperon. In Figure 1.1, $p_t = P_{hyperon} \times \theta_{prod}$ and $x_F = p_t/(P_{inc.proton} \times \theta_{prod})$, where θ_{prod} is the production angle. For a constant x_F, the polarization increases in magnitude with p_t but flattens above $p_t \approx 1$ GeV/c. Figure 1.3 shows the polarizations of the Σ's and the Ξ's as a function of p_t.

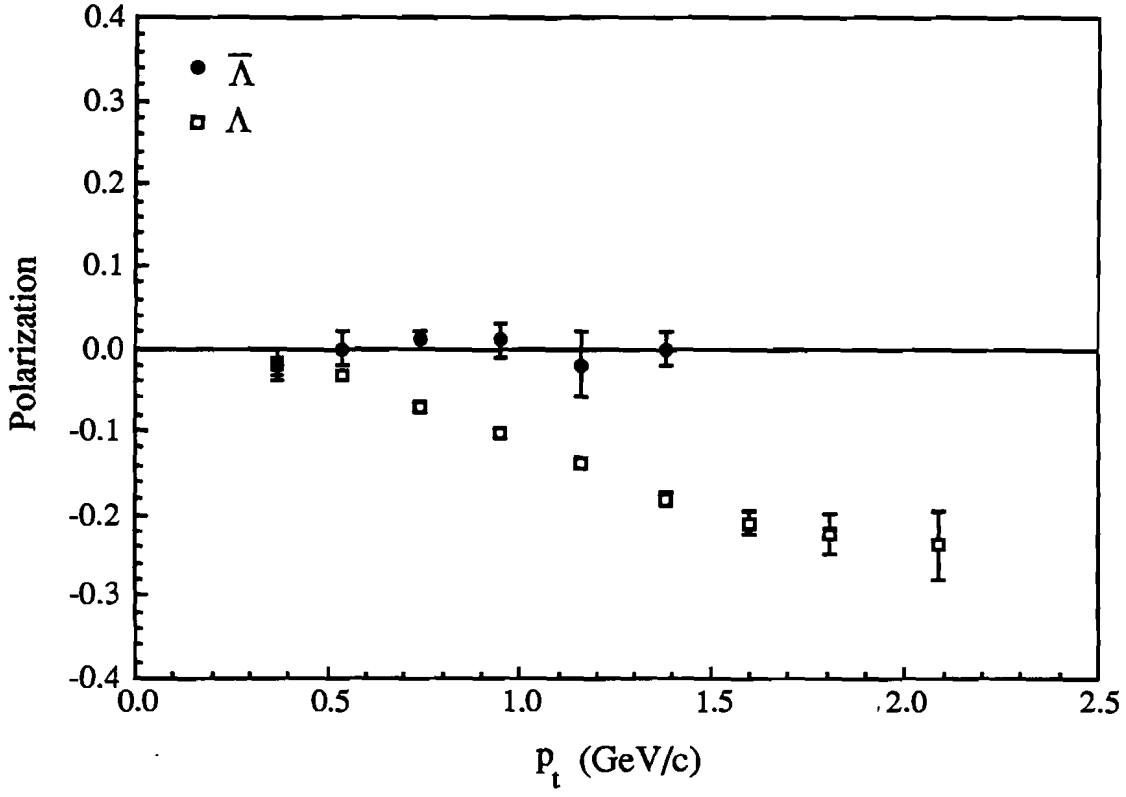

Figure 1.2 Polarization of Λ and $\overline{\Lambda}$ at 400 GeV/c and production angle of 7.2 mrad.

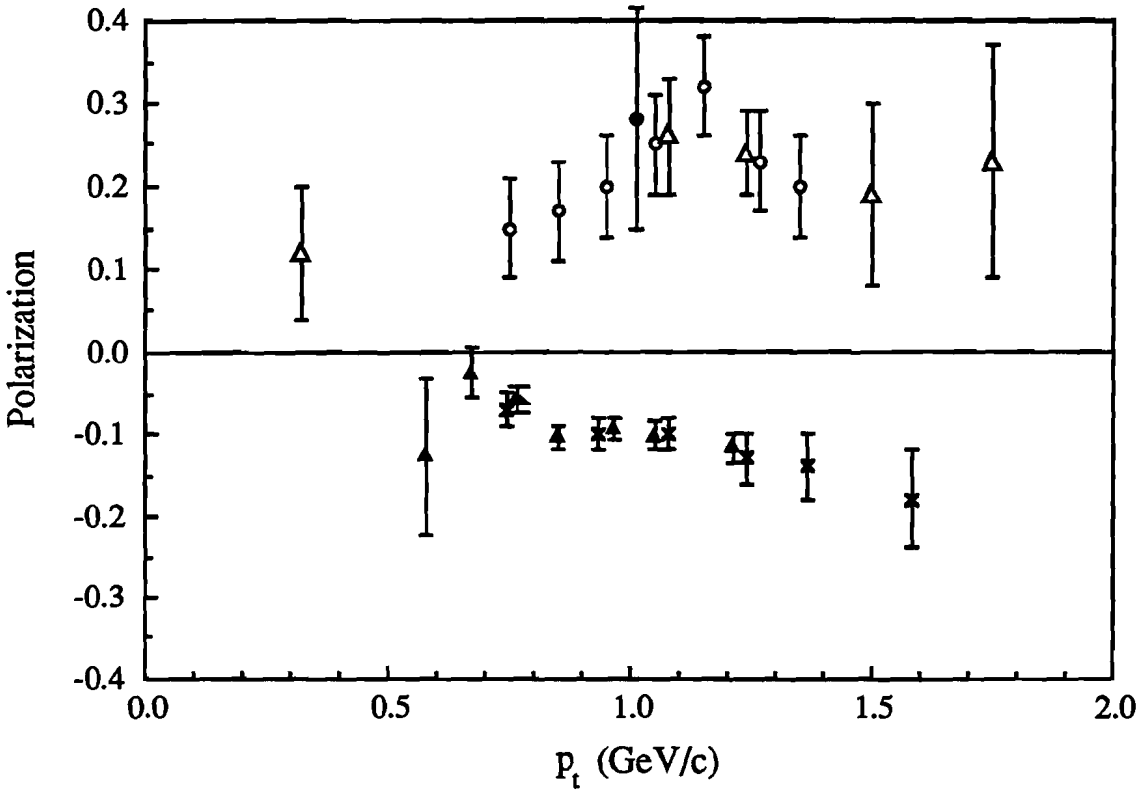

- ○ Σ^+ at 400 GeV/c and 5 mrad on Be target (see Ref. 2)
- △ Σ^- at 400 GeV/c on Cu target (see Ref. 6)
- ● Σ^0 at 28.5 GeV/c on Be target (see Ref. 8)
- × Ξ^0 at 400 GeV/c and 7.2 mrad on Be target (see Ref. 4)
- ▲ Ξ^- at 400 GeV/c and 5 mrad on Be target (see Ref. 7)

Figure 1.3 Polarization of hyperons.

Based on the experimental results before this experiment, most of the hyperons are polarized, where Σ^0, Σ^+, Σ^- have positive polarization and Λ, Ξ^0, and Ξ^- have negative polarizations. Anti-hyperons, namely $\bar{\Lambda}$, are not polarized. It is generally believed that hyperon production polarization is a kind of leading particle effect. That is, the polarization is related to the valence quarks of the incident particle. Thus there should be no polarization for particles that do not share any valence quarks with the incoming projectile. Therefore, Ω^- and the anti-hyperons will not be significantly polarized.

1.4 Theoretical Models

Due to the fact that hyperons produced by protons were polarized, a few models were proposed to explain the phenomenon.

1) Gluon bremsstrahlung

This model was proposed by K. Heller *et al.*[10] In the case of Λ polarization, a valence u quark of the proton is scattered off a target nucleus and radiates a gluon, which consequently fragments into an $s\bar{s}$ pair. If the gluon is polarized, then so is the $s\bar{s}$ pair. This polarized s quark then combines with the spectator u and d quarks of the proton to form a polarized Λ. Figure 1.4 illustrates this mechanism. For the case of $\bar{\Lambda}$, a $\bar{u}$ and $\bar{d}$ quarks must also be produced and combine with the $\bar{s}$ quark to form a $\bar{\Lambda}$. Since the quarks are produced incoherently from the sea, no polarization will be observed.

2) Lund model

The Lund model[14] was proposed by Andersson, Gustafson and Ingelman. A $q\bar{q}$ pair is produced from the breakdown of the stretched color (gluon) field between the collision center and the spectator quarks of the incident particle. The angular momentum of the $q\bar{q}$ pair must be compensated by the spin of the created quarks to conserve total angular momentum. Therefore the sea quarks get polarized. Figure 1.5 shows how Λ gets polarized in this picture. The ud diquark of the incoming

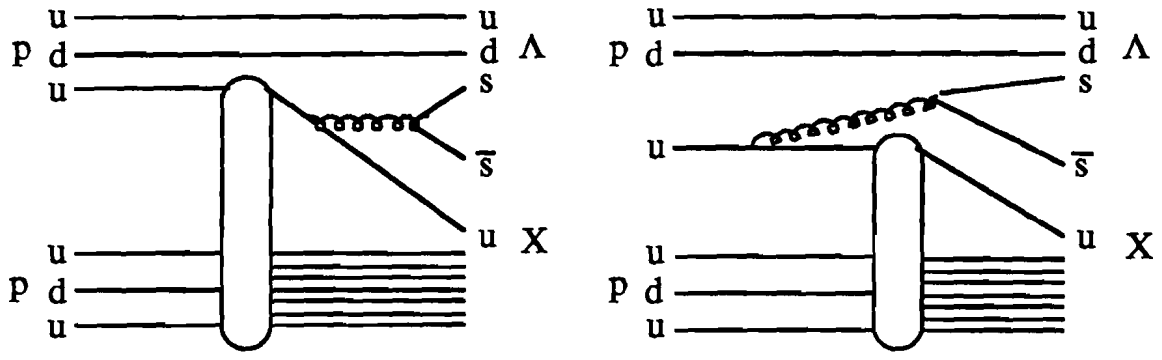

Figure 1.4 Gluon bremsstrahlung mechanism.

proton is scattered in the direction of $\mathbf{p}_\Lambda$, the momentum of the Λ, from the scattering center (the shaded area). The color field is stretched out as the ud diquark moves away from the scattering center and finally breaks down. An $s\bar{s}$ pair is created in this process. The momenta, $\mathbf{k}_\perp$, of the sea quarks form a angular momentum **L** (pointing out of the page) for the $s\bar{s}$ system. In order to conserve total angular momentum, the spin, **S**, of the s and $\bar{s}$ quarks must compensates **L**, i.e., **S** points into the page (this also explains why the polarization of Λ is negative, i.e., anti-parallel to the production normal). This polarized s quark recombines with the ud diquark to form a polarized Λ.

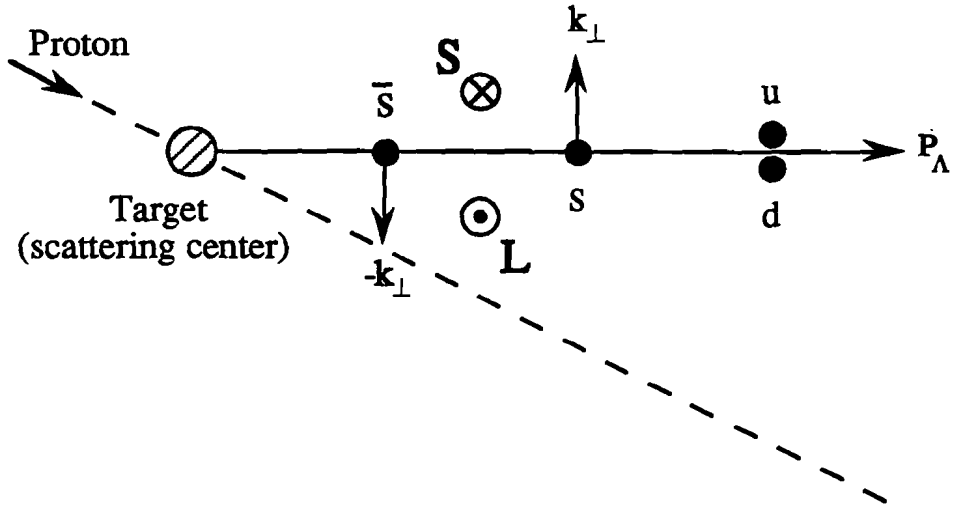

Figure 1.5 Lund model.

3) DeGrand and Miettinen model

Hyperon polarization is due to a Thomas precession effect during the quark recombination process.[15] As in the previous example, a Λ is formed from the recombination of the ud diquarks and the s quark from the sea. The s quark is accelerated by a force **F** representing the color field in this process. Since the velocity, **V**, of the quark and the force do not have the same direction as shown in Figure 1.6, the spin, **S**, of the accelerated quark will feel the effect of the Thomas precession. This leads to a Thomas precession term, $U_T = \mathbf{S} \cdot \boldsymbol{\omega}_T$, in the Hamiltonian, where $\boldsymbol{\omega}_T$ is the Thomas frequency which is proportional to $\mathbf{F} \times \mathbf{V}$. Since the scattering amplitude is proportional to the Hamiltonian and therefore proportional to U_T, the process will then be enhanced if **S** parallel to $\boldsymbol{\omega}_T$. Therefore the Λ gets polarized because of the polarized s quark.

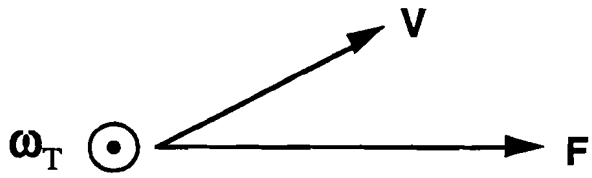

Figure 1.6 DeGrand and Miettinen model.

4) Sea quark scattering

J. Szwed[16] suggested that the sea quark gets polarized by multiple scattering in the color (gluon) field. This is analogous to the polarization of electron in Coulomb scattering process. The polarized sea quark combines with the spectator quarks of the incoming projectile to form a polarized hyperon. The polarization of the quark can be written as

$$\mathbf{P} = \frac{2C\alpha_s m|k|}{E^2} \frac{\sin^3\frac{\theta}{2}\ln(\sin\frac{\theta}{2})}{\left[1-\frac{k^2}{E^2}\sin^2\frac{\theta}{2}\right]\cos\frac{\theta}{2}}\hat{n} \qquad (1.4)$$

where C is a variable depended on the external color field, α_s, θ, and $\hat{n}$ are the strong coupling constant, scattering angle and the production normal respectively; m, k and E are the mass, momentum and energy of the scattered quark. Note that the energy of the sea quark is relatively low, otherwise the polarization would be negligible since the polarization is inversely proportional to E^2. This is the reason why the $\overline{\Lambda}$ is not polarized as all the anti-quarks from the sea have relatively higher energy.

1.5 Magnetic Moment

If a particle is polarized, it is possible to measure its magnetic moment. Since the spin of a particle will precess in an external magnetic field, the precession angle, ϕ, can be measured if its polarization, **P**, is non-zero as shown in Figure 1.7. The precession angle with respect to the particle's momentum, $\vec{p}$, is given by [18]

$$\phi = \frac{q}{\beta mc}\left(\frac{g}{2}-1\right)\int B dl \qquad (1.5)$$

where g, q and m are the gyromagnetic ratio, charge and mass of the particle respectively, $\beta = v/c$ and $\int Bdl$ is the magnetic field integral. By definition the magnetic moment μ can be written as

$$\mu = \frac{g}{2}\frac{q}{mc}S \qquad (1.6)$$

where S is the spin of the particle. From Eqs. (1.5) and (1.6) μ can be related to ϕ as

$$\phi = \frac{2}{\beta}\left(\mu-\frac{q}{2mc}\right)\int B dl \qquad (1.7)$$

for spin 1/2 particle. ϕ is determined in the experiment and then μ can be extracted.

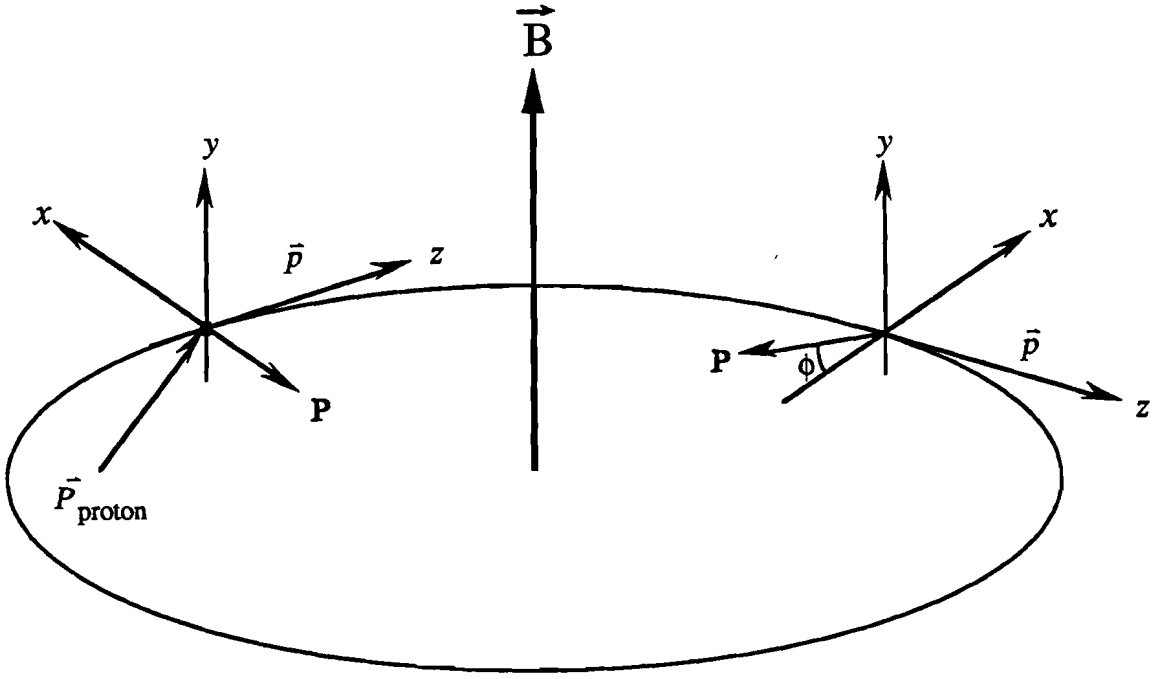

Figure 1.7 Spin precession in magnetic field.

The magnetic moments of Λ, Σ^+, Σ^-, Ξ^0, and Ξ^- were all measured by this spin precession technique.[3,19-24] This thesis presents the first measurement of the magnetic moment of an anti-hyperon, $\bar{\Xi}^+$, by using the same method. The theoretical prediction of μ_{Ξ^-}, based on the SU(6) quark model, is -0.46 nuclear magneton.[30] CPT invariant requires that the magnetic moment of an anti-particle must has the same magnitude but opposite sign as that of its particle. i.e., $\mu_{\bar{\Xi}^+} = -\mu_{\Xi^-}$.

CHAPTER 2

APPARATUS

2.1 Introduction

The experiment was performed in the Proton Center beam line at Fermilab. An 800 GeV/c proton beam was incident on a beryllium target. A secondary beam of charged particles, produced by the protons, was defined by a curved collimator through a magnet. Particles were detected with a spectrometer consisting of scintillation counters, silicon strip detectors, multiwire proportional chambers and an analyzing magnet.

2.2 Proton Beam and Target Area

The Fermilab Tevatron delivered 800 GeV/c protons to each experimental area at a 58 seconds cycle, in a burst of 23 seconds duration during the 1987-88 fixed target run. Such a burst is also called a "beam spill." A proton beam was transported, through a series of bending (dipole) and focusing (quadrupole) magnets, from the Tevatron to the P - Center target area. The proton intensity was monitored by an

argon-filled ionization chamber (IC) and a secondary emission monitor (SEM) 22.2 m upstream of the target. The beam intensity in this experiment ranged from 10^9 to 10^{12} protons / spill and was about 10^{10} for the $\bar{\Xi}^+$ run.

Figure 2.1 shows the beam line set up in the target area. The bending and focusing magnets, controlled by the experimentalists at P - Center, were used to steer the proton beam and hit the target at various production angles. Two segmented wire ion chambers (SWIC) were placed in front of the target to monitor the production angle. These chambers had 0.5 mm pitch and were separated by 175 cm along the proton beam line. This system provided a resolution of about 0.06 mrad in determining the production angle. The beryllium target had dimensions of $2 \times 2 \times 91$ mm^3 (1/4 interaction length for protons) and its center was 21.6 cm upstream of the entrance of the collimator.

2.3 Collimator

After the beam protons interacted with the target, a secondary charged beam was defined by a curved collimator embedded in a 7.316 m long dipole magnet M1 with a uniform vertical field. The collimator was made up of 60 brass and 40 tungsten blocks. The tungsten blocks were used as a dump for the beam protons. The narrowest part of the collimator, 5×5 mm^2 in aperture, was called the defining collimator since it defined the beam size of the secondary particles. Figure 2.2 shows the horizontal and vertical view, and the cross sections of the collimator.

The central orbit of the curved channel had a radius of 497.5 m and a bend angle of 14.7 mrad (the angle defined by the tangents to the central orbit at the entrance and exit of the collimator), which corresponded to the trajectory of a 500 GeV/c particle with charge *e* travelling perpendicular to an uniform magnetic field of 3.35 Tesla.

The field strength of M1 was measured with a Hall probe which was accurate to 1 % . The field integral $\int Bdl$ was set to 15.35 T-m for the $\bar{\Xi}^+$ run (-15.29 T-m for the

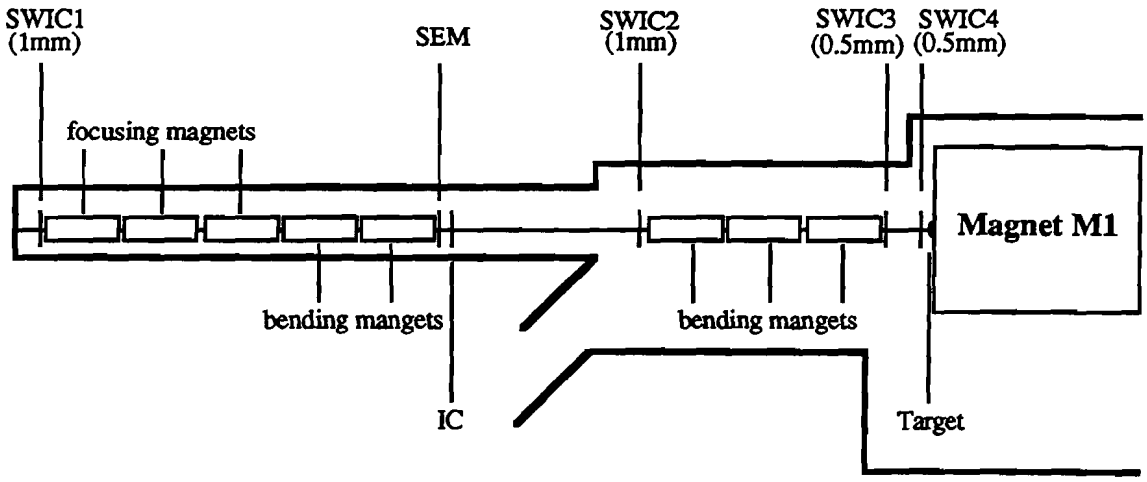

(a) Target area

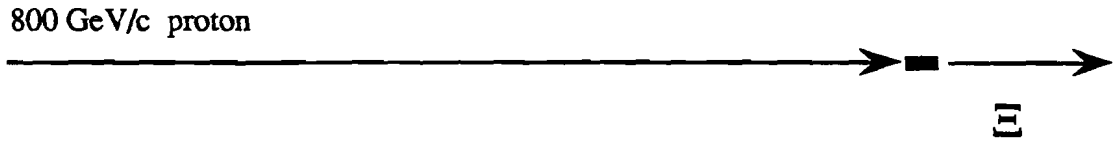

(b) Plan view

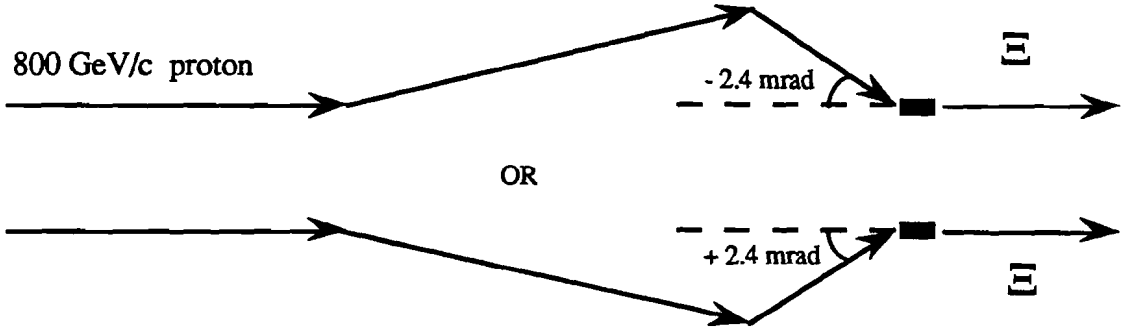

(c) Elevation view

Figure 2.1 (a) Beam line set up at the target area (b) and (c) are plan and elevation view of a proton beam hitting the target with a vertical production angle of -2.4 or +2.4 mrad.

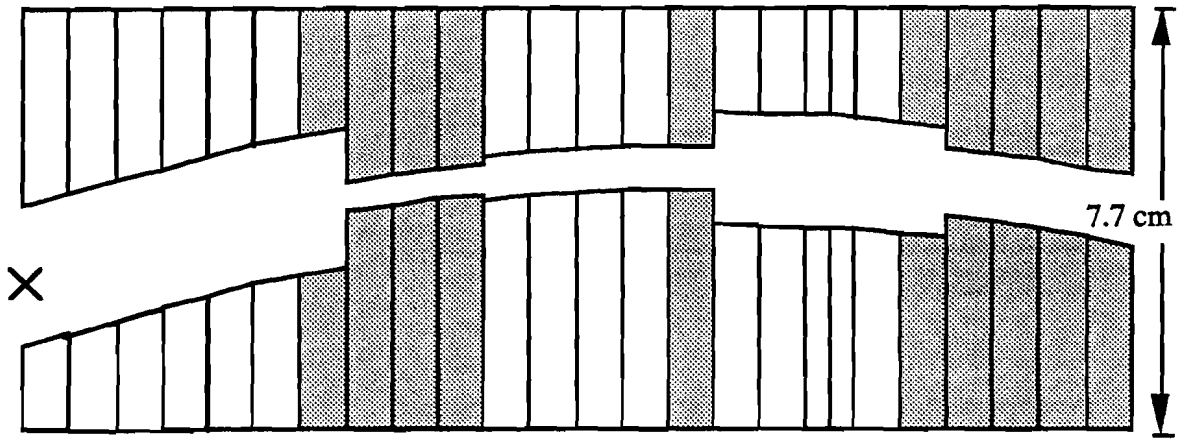

(a) Bend view

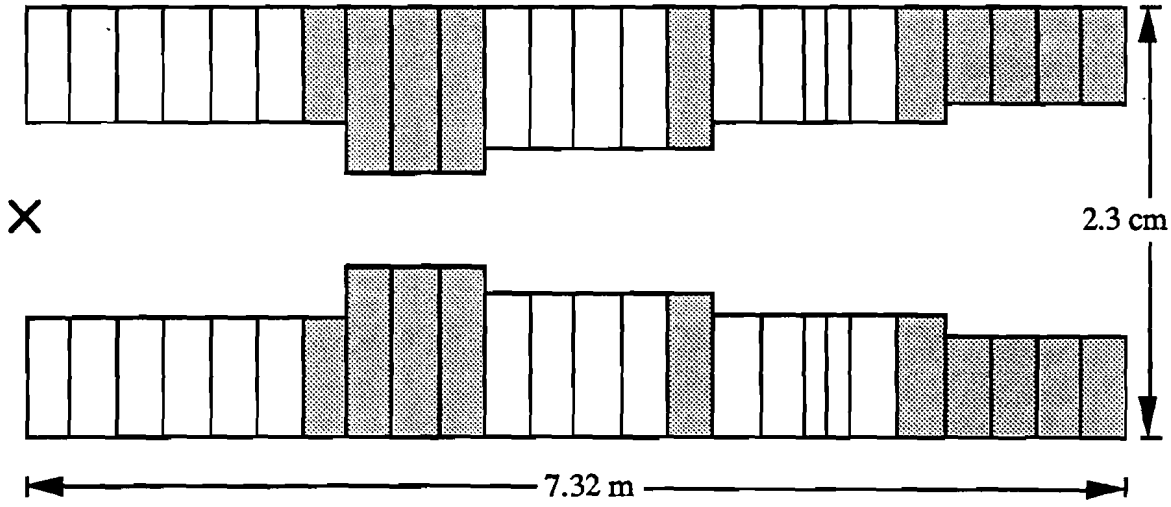

(b) Non - bend view

Brass

Tungsten

The center of the entrance of the collimator

Figure 2.2 (a) and (b) are bend view (magnetic field of M1 perpendicular to this plane) and non-bend view of the collimator.

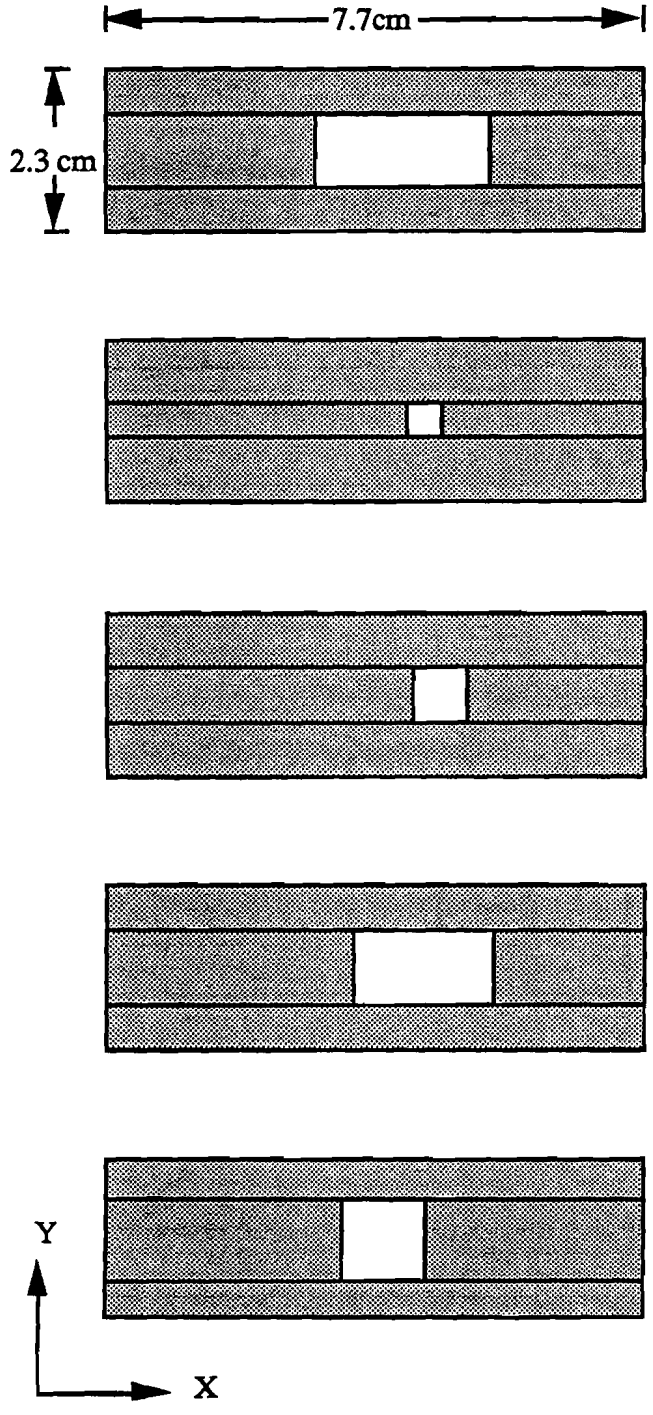

Distance from Entrance (m)	X Width (cm)	Y Width (cm)
2.13	2.54	1.02
3.05	0.50	0.50
4.57	0.76	0.76
6.10	2.00	1.01
7.32	1.22	1.22

Figure 2.2 (c) Cross sections of the collimator.

Ξ^- run). Figure 2.3 shows the channel acceptance as a function of momentum at $\int Bdl$ = 15.35 T-m. This acceptance curve was based on a sample of Monte Carlo events, with charge *e*, generated at the target with a flat production spectrum. The acceptance at each momentum bin is the ratio between the number of events exiting the channel to that of events passing through the defining collimator in the same momentum bin.

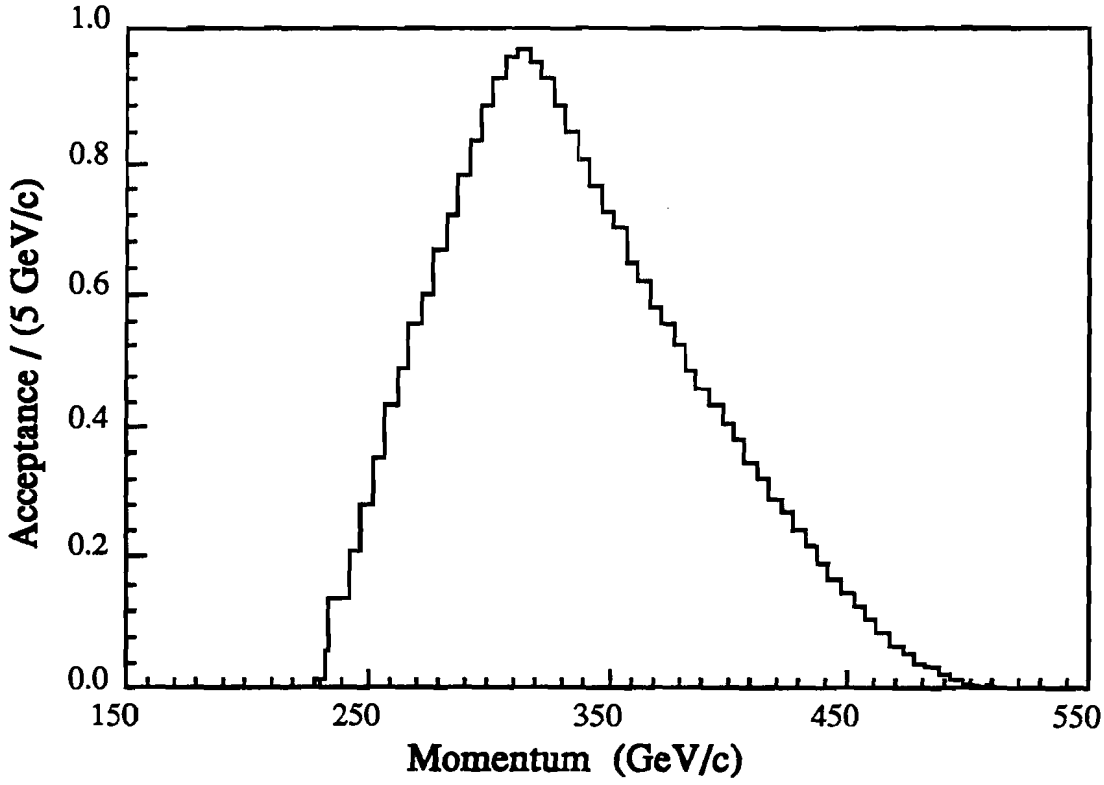

Figure 2.3 Channel acceptance of the collimator at $\int Bdl$ = 15.35 T-m.

2.4 Spectrometer

The charged particles were detected with a spectrometer consisting of five scintillation counters, eight silicon strip detectors (SSD), nine multiwire proportional chambers and an analyzing magnet. A plan view of the spectrometer is shown in

Figure 2.4. Table 2.1 lists the z-position (with respect to the channel exit), dimensions in the x and y view, and pitch of all the essential elements of the spectrometer.

A set of eight SSD planes (four in x and four in y view) was installed right after the M1 exit. The first plane SSD1X was 86 cm downstream of the exit (i.e., z = 86 cm), and then each successive one was labeled 1Y, 2X, 2Y, etc. The separations between planes are listed in Table 2.1. Each plane had 280 strips with each strip 100 μm wide and 3 cm long.

Scintillators S1 and S2 served as a beam counter. V1 and V2 were veto counters to eliminate charged particles which came outside of the beam halo. The pulse height of the multiplicity counter M depended on how many minimum ionizing particles passed through the counter.

C1- C9 were multiwire chambers. C1-3 had 1 mm wire spacing and C4-9 were 2 mm. All chambers had horizontal and vertical signal planes. In C4 the two orthogonal planes were rotated by 45 degrees about the z-axis. There was an additional senseplane rotated by 45 ° counterclockwise in C5 that had a wire spacing of 2.8 mm. The rotated planes were used for associating the x and y views in the event reconstruction.

The chambers were filled with a gas mixture of 99.9% argon and 0.1% freon bubbled through methylal at 0 °C. The operating voltages of the chambers ranged from -2.7 to -4.2 kilovolts. Table 2.1 shows the positions and dimensions of each detector and counter.

The analyzing magnet M2 consisted of two parts. The first part was 2 m long with an aperture of 25×61 cm^2. The second part was also 2 m long but 30×61 cm^2 in aperture. The two magnets was separated by 30 cm. The magnetic field could point either in the $+y$ or $-y$ direction with a total transverse bending power of 1.54 GeV/c in the xz-plane. The magnet was measured by a zip-track technique. The technique is described as follow. A coil, to measure the x, y, and z components of the magnetic field

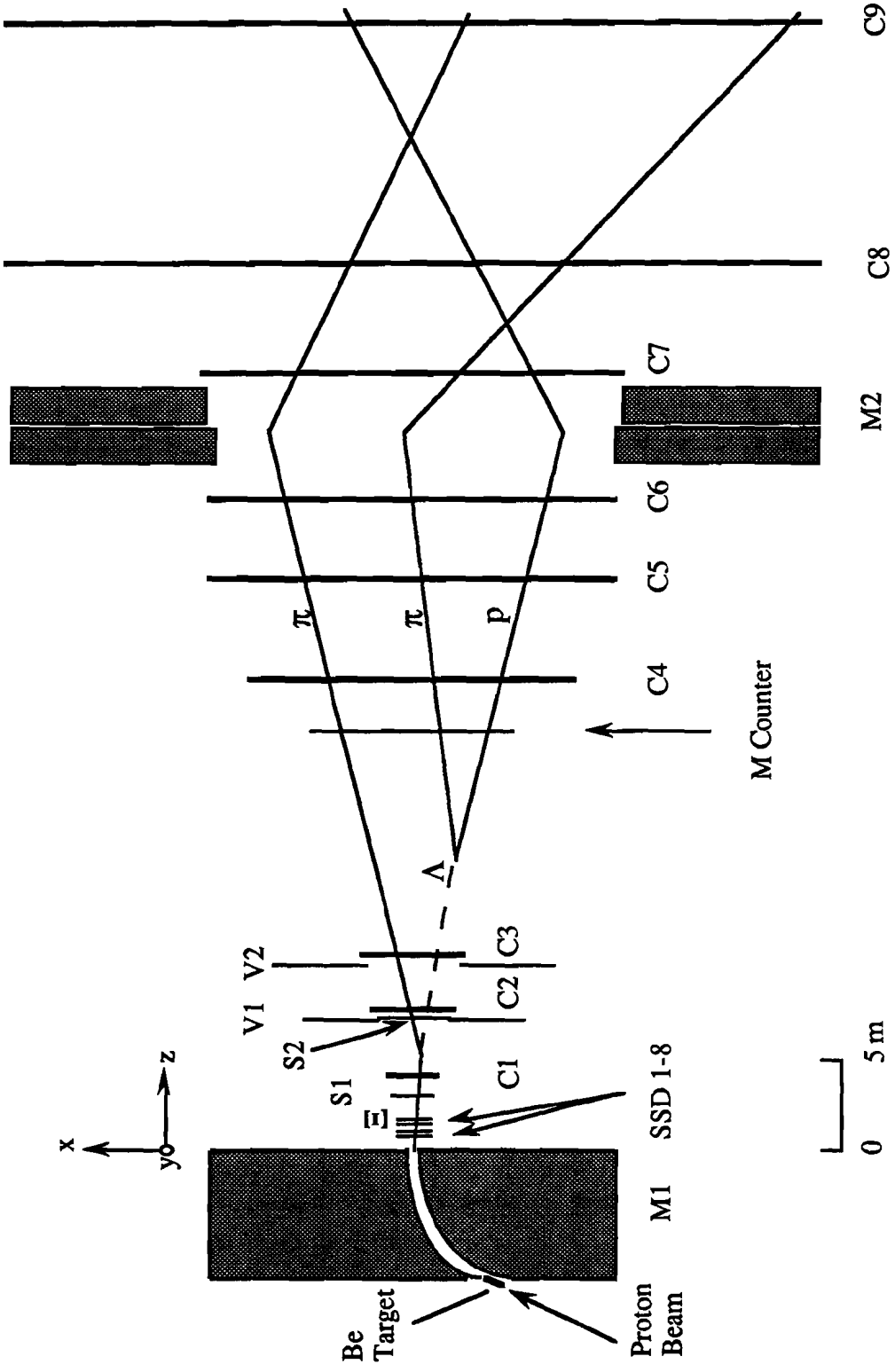

Figure 2.4 Plan view of the spectrometer. Note that the transverse dimensions have been exaggerated. (See Table 2.1)

of M2 , was mounted on a stand which could move along a track parallel to the z-axis. This technique allowed us to map out the magnetic field of M2 at any space point inside the magnet. The calculated bend plane and field integral from the zip-track data were consistent with that determined by real data up to 99 %.

Plastic bags filled with helium gas were installed between chambers in order to minimize the effect of multiple Coulomb scattering to the detected particles.

When the polarity of M1 was set to select a negative beam, the beam mainly consisted of a mixture of π^-, K^-, Σ^-, Ξ^- and Ω^-. A secondary beam with opposite charge was selected when the polarity of M1 was reversed. Therefore, the particles and its anti-particles could be detected under the same conditions except the polarity of the magnets M1 and M2 was reversed. This was an extremely useful tool to cross check all physical measurements and analysis programs in the experiment. For example, the polarization and the magnetic moment of Ξ^- was well measured[7,9,24] but that of the $\overline{\Xi}^+$ was completely unknown before this experiment. If the magnetic moment measurement of Ξ^- can be reproduced in this experiment, the measurement of $\overline{\Xi}^+$ polarization and magnetic moment will be very reliable by using the same analysis method.

From now on, all the symbols without associated with its charge sign apply to both the particles and its anti-particles, e.g., Ξ and Λ means Ξ^- or $\overline{\Xi}^+$, and Λ^0 or $\overline{\Lambda}^0$ respectively. For some special situations, the charge sign will be specified explicitly.

2.5 Trigger Logic and Data Acquisition

For the $\overline{\Xi}^+$ run, the magnetic fields of both M1 and M2 were pointed in the $+y$ direction. The decay sequences of interest were

$$\overline{\Xi}^+ \rightarrow \overline{\Lambda}^0 + \pi^+$$
$$\quad\quad \hookrightarrow \overline{p} + \pi^+$$

(a) SSDs and Chambers

	Z (cm)	X × Y (cm^2)	Pitch (mm)
SSD 1X	86.2	2.8 × 2.8	0.1
SSD 1Y	94.5	2.8 × 2.8	0.1
SSD 2X	114.6	2.8 × 2.8	0.1
SSD 2Y	122.9	2.8 × 2.8	0.1
SSD 3X	143.0	2.8 × 2.8	0.1
SSD 3Y	151.3	2.8 × 2.8	0.1
SSD 4X	171.4	2.8 × 2.8	0.1
SSD 4Y	179.7	2.8 × 2.8	0.1
C 1	405.5	12.8 × 12.8	1.0
C2	753.6	25.4 × 25.4	1.0
C3	1054.7	25.4 × 25.4	1.0
C4	2597.8	51.0 × 25.4	2.0
C5	3154.4	51.0 × 51.0	2.0
C6	3605.1	44.6 × 27.0	2.0
C7	4310.5	63.0 × 25.4	2.0
C8	4897.4	120.0 × 38.2	2.0
C9	6228.0	127.8 × 38.2	2.0

(b) Counters

	Z (cm)	X × Y (cm^2) (outside aperture)	X × Y (cm^2) (inside aperture)
S1	369	6.4 × 3.8	
S2	724	10.8 × 6.4	
V1	723	32.4 × 8.9	10.8 × 6.4
V2	1014	41.9 × 11.4	14.0 × 8.3
M	2331	30.5 × 30.5	

Table 2.1 Z-position, dimensions and pitch of (a) SSDs and Multiwire chambers (b) Counters.

After M2, the π^+'s were bent to the -x direction and $\bar{p}$'s to the +x direction. The trigger required a signal from counters S1 and S2 with no signal from the veto counters V1 and V2. The pulse height from the multiplicity counter M was required to be greater than that corresponding to two (M_{min}) but less than five (M_{max}) minimum ionizing particles. Downstream of M2 at least one hit on the right side (- x) of C8 and one hit on the left side of C9 were required. Thus the final trigger was

$$\Xi = S1 \cdot S2 \cdot \overline{V1} \cdot \overline{V2} \cdot M_{min} \cdot \overline{M}_{max} \cdot C8R \cdot C9L$$

For the Ξ^- run, the fields of M1 and M2 were reversed so that the same trigger was also applied to $\Xi^- \rightarrow \Lambda^0 + \pi^+$, $\Lambda^0 \rightarrow p + \pi^-$ decays.

A single track trigger was mixed with the 3-track Ξ trigger. This trigger was defined as

$$\pi = S1 \cdot S2 \cdot \overline{V1} \cdot \overline{V2}$$

and was prescaled by a factor of 1024 .

A good event was formed if the signal from all the trigger counters and chambers satisfied the above trigger requirements. The relevant information of the good event, namely the wire hits in each MWPC, the pulse heights from all the ADC modules and the latched signals for the various scintillation counters, were read into the on-line PDP-11/45 computer memory via a CAMAC interface and then written onto a magnetic tape. The tapes were later analyzed (event reconstruction) off-line on Fermilab's Cyber computer system.

For the whole $\bar{\Xi}^+$ sample, there were 83 raw data tapes. Each tape had about 4×10^5 triggers consisted of 1×10^5 of π and 3×10^5 of Ξ triggers.

2.6 Detector Alignment and Efficiency

All the chamber and SSD centers were aligned by reconstructing single track events with M2 switched off. Using this method, the chamber centers were determined with an accuracy better than one tenth of a pitch of the detector. The detectors efficiency were constantly monitored by using these single track events. For the entire run, the average efficiency was about 85% for the SSD's, and 98 % for all the chambers, except the y-view plane of C3 which was about 40% efficient.

Some chambers were found to be slightly rotated about the z axis in the alignment process. Only those rotated chambers which affected the tracking resolution were corrected in the reconstruction. These chambers were C5, C12 and C13 with rotation angles of 2.2, 2.5 and 3.5 mrad respectively.

CHAPTER 3

EVENT RECONSTRUCTION AND SELECTION

3.1 Introduction

Raw information of any event satisfying the trigger requirements was written to tape during the data taking period. The trigger requirements were set to a minimum (loose) level to avoid bias on the data sample. Therefore, only some fraction of the raw events were of physical interest. In order to select these events and determine their kinematic information, it is necessary to reconstruct the event from the raw information. A reconstruction program is a computer software package looking for certain track topology and determining all the kinematic variables such as the location of the decay vertex and momentum of each particle. Events that passed through the reconstruction program were 3-track candidates with the topology shown in Figure 2.4. These events were written to other tapes called data summary tapes for second level of analysis. To eliminate all the physical backgrounds, a further filtering process called event selection was applied to these 3-track candidates before the polarization analysis.

3.2 Event Reconstruction

The reconstruction program could be further subdivided into several stages. Events failing the 3-track candidate test would be filtered out at different stages to speed up the computing time. These failed events were categorized as different classes to keep track of what kinds of events were lost. Table 3.1 lists the description of each class of failed events.

Class	Description
1	Three of the four planes of C8 and C9 have less than two hits.
2	Four of the six downstream *y*-views have four or more hits.
3	Four of the six downstream *y*-views have less than two hits.
4	Less than two of the *y*-planes of C8, 10, 11, 12 have two or three hits.
5	Looks like two tracks event in *y*-view.
6	Cannot find three tracks in *y*-view.
7	Cannot find three tracks in *x*-view.
8	Three tracks before M2 but only two tracks after M2.
9	The high momentum track bends the same way as one of the low momentum tracks.
10	Three tracks events, only one hit on one track in *x*-view after M2.
11	The second decay vertex was upstream of the first decay vertex.
12	Geometric $\chi^2 > 130$.
13	Divergence in the geometric fit.
14	Divergence in the kinematic fit.
0	3 - track candidate.

Table 3.1 Description of different class of events in the track finder program.

Stage 1 - Raw Hit Counting :

This stage rejected events which had too few or too many hits by counting the number of hits in each chamber plane. These kinds of events were labelled as class 1, 2, 3, 4, and 5.

Stage 2 - Track Finder :

Since the 3-track trigger demanded that at least three charged particles passed through the multiplicity counter M, three charged tracks should be found from C4 to C9 (all 2 mm chambers). But this was not necessarily true in the front-end detectors (including all SSD planes, C1, C2, and C3) as particles could decay anywhere in this region. If the tracking program could not find three tracks in the y-view by using only six 2 mm chambers, this event was classified as class 6. Similarly, classes 7, 8, 9, and 10 were events which failed in the x-view. After three track segments were found in both x and y views, a correction to the chamber rotation was applied to the raw hit position before a geometric fit was performed.

Stage 3 - Geometric Fit :

All tracks were found independently in stage 2. There was no special requirement for a certain geometric topology. Since the aim was to find 3-track events which had the topology of Figure 2.4 with one parent track, two decay vertices and three daughter tracks, these constraints had to be imposed on the tracks to fit such a topology. There were thirteen variables to be determined in the fit, namely, the three coordinates of the parent particle decay vertex, the separation along the z-axis of the two vertices, and nine slopes for the three tracks. The momenta of each particle was calculated from the bending of the track in the magnet M2. After the fit, events with a second decay vertex upstream of the first decay vertex (i.e., the daughter decayed before its parent) was classified as class 11. Those events which failed to fit the topology of Figure 2.4 would have either a large chi-square or they would not converge in the fitting routine. Chi-square χ^2 is defined as the sum of the squares of the residuals of each track at each detector plane divided by the corresponding resolution of the detector, where the residual of a track at a detector plane is the distance

between the raw position and the fitted position. Class 12 contained events with $\chi^2 >$ 130 (typical degrees of freedom at this stage was 20), and class 13 meant a divergence in the fit. All the surviving events were good 3-track candidates and were temporarily labelled as class 0.

Stage 4 - Front-end Tracking :

At this stage, class 0 events did not include any raw hit information from the front-end detectors. Obviously, this information should be included to improve the resolution. The front-end tracking routines looked for hits, which belonged to the tracks found at stage 3, from the front-end detectors.

The algorithm is the following. Based on the geometric fit of the class 0 event, the *z*-position of the second decay vertex, Z_{2nd}, can be determined. Z_i was defined to be the *z*-position of the most upstream detectors (SSD or chamber) used in the geometric fit and Z_{i-1} to be the z-position of the next detector upstream of Z_i. The following cases would happen.

Case 1. There were detectors between Z_{2nd} and Z_i. These detectors should contain hits belonging to each of the three downstream tracks. See Figure 3.1 (a).

Case 2. There was no detector between Z_{2nd} and Z_i. That meant the second decay vertex was within Z_{i-1} and Z_i, i.e. $Z_{i-1} < Z_{2nd} < Z_i$. Only one track (the parent and the decay daughter track) should be found in the rest of the detectors. If the parent particle decayed within the front-end detectors, a kink might also be found somewhere along this track. See Figure 3.1 (b).

To find out all the hits in case 1, the downstream tracks, one at a time, were extended to the next upstream detector from which the hit closest to this track was found. The geometric fitter would use this hit to refit the whole decay topology and calculate the new chi-square χ^2_{new}. If $\chi^2_{new} < \chi^2_{old} + 10$ and $\chi^2_{new} < 100$, this hit was assigned to the corresponding track, where χ^2_{old} was the chi-square before the new

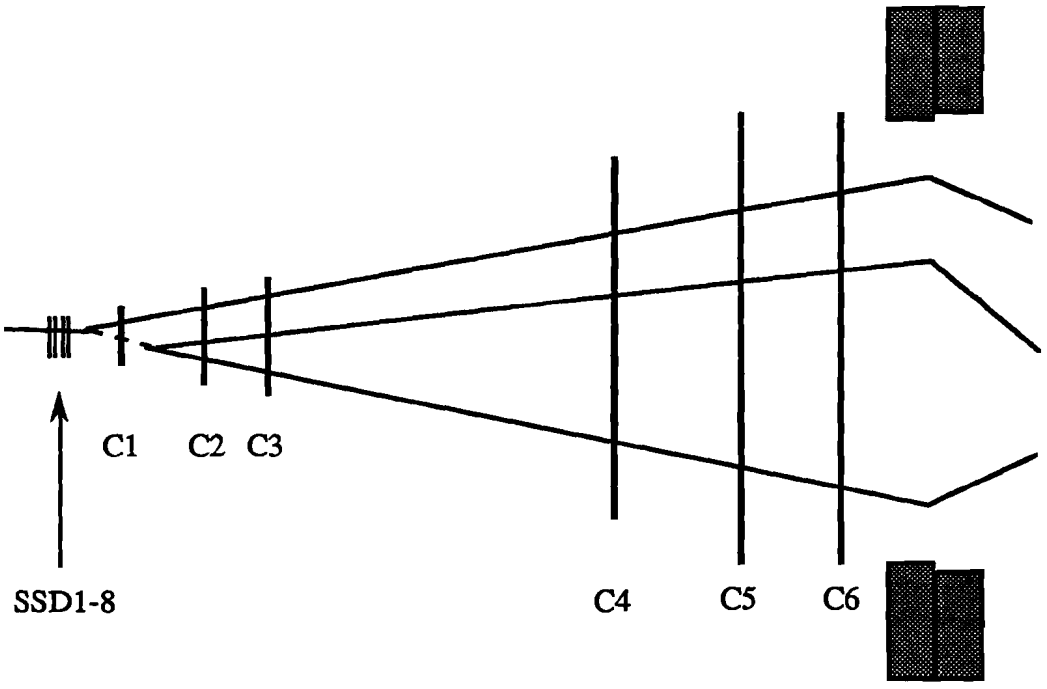

(a)

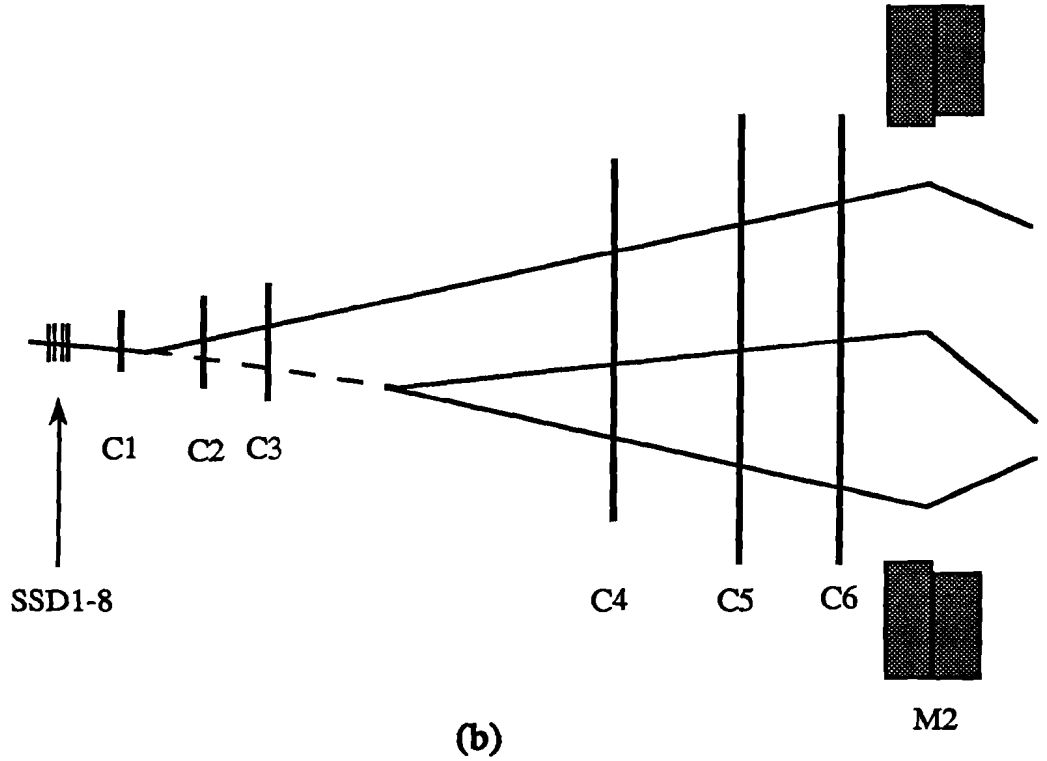

(b)

Figure 3.1 Location of the second decay vertex , example (a) case 1: $Z_i = Z_{C4}$, $Z_{i-1} = Z_{C3}$, $Z_{2nd} < Z_{i-1}$, (b) case 2: $Z_{i-1} < Z_{2nd} < Z_i$.

hit was included. Otherwise, this hit was ignored and all the kinematic variables were kept unchanged. Hits for all the tracks, both in x and y views, were found this way. Once the hits in this detector were found, a new Z_{2nd} was determined and it should be more precise than the old one.

If there were still detectors between the new Z_{2nd} and Z_i, which was case 1, the procedure described in the last paragraph was repeated. Otherwise, hits would be found for case 2.

In case 2, we would like to determine the first decay vertex Z_{1st} more precisely before we searched the hits for the daughter track from the decay parent. Otherwise, the hits belonging to the parent might be assigned to its daughter track since the kink angle could be very small. If Z_{1st} was located after all the SSD planes, a single track segment should be found by using only SSD's. This single track together with the downstream track not associated with the second decay vertex could locate the kink by using the distance of closest approach technique. Hits between the kink and Z_i were assigned to the daughter track. Otherwise, the single downstream track was simply extended to the next front-end detector to look for the closest hit. Like case 1, these hits were assigned to the corresponding track if the χ^2_{new} satisfied the same criteria. The search stopped when a large chi-square was found since it indicated a kink might occur and these hits belonged to the parent track.

Stage 5 - Kinematic Fit :

After all the raw information was used in the 3-track fitting, the two tracks which originated from the second vertex were further constrained to form an invariant mass equal to the Λ mass and then refitted the whole topology to redetermine the momenta of all particles. This fit was called a kinematic fit since the kinematic constraints were imposed in the fit. Class 14 contained those kinds of events which did not converge in the kinematic fit.

All the events which passed through stage 5 were classified as class 0 and were written to a tape for second level analysis. Table 3.2 shows the distribution of

events belonging to different classes for a typical $\bar{\Xi}^+$ run. Events only appeared in one class. Once an event failed no further analysis was performed. About 8.8% of the candidates were good (class 0) 3-track events.

Class	(%)
0	8.8
1	1.0
2	3.3
3	7.2
4	0.6
5	23.8
6	9.3
7	7.6
8	10.4
9	6.3
10	14.3
11	0.7
12	2.5
13	2.3
14	1.9

Table 3.2 Distribution of events (in a typical $\bar{\Xi}^+$ run) belonging to different classes in the reconstruction program.

3.3 Event Selection

Even though all the class 0 events in the data summary tape were good 3-track candidates with topology as shown in Figure 2.4, they were not necessarily the $\Xi \rightarrow \Lambda + \pi$ and $\Lambda \rightarrow p + \pi$ decay sequences since $K \rightarrow 3\pi$, or $\Omega \rightarrow \Lambda + K$ and

$\Lambda \rightarrow p + \pi$ might be present. A second level filtering was necessary to pick out the real Ξ candidates. In order to understand what kinds of 3-track events were rejected, a sequential cut (filtering) was applied as follows.

1) Geometric χ^2 cut

Figure 3.2 shows the geometric χ^2 distribution of all class 0 events. It is obvious that the $\chi^2 < 130$ requirement at the first level filtering was too generous. At this stage, it was required that the χ^2 be less than 70 (the typical degrees of freedom was 26), which was near the tail of the distribution. This cut removed about 9% of the 3-track class 0 events.

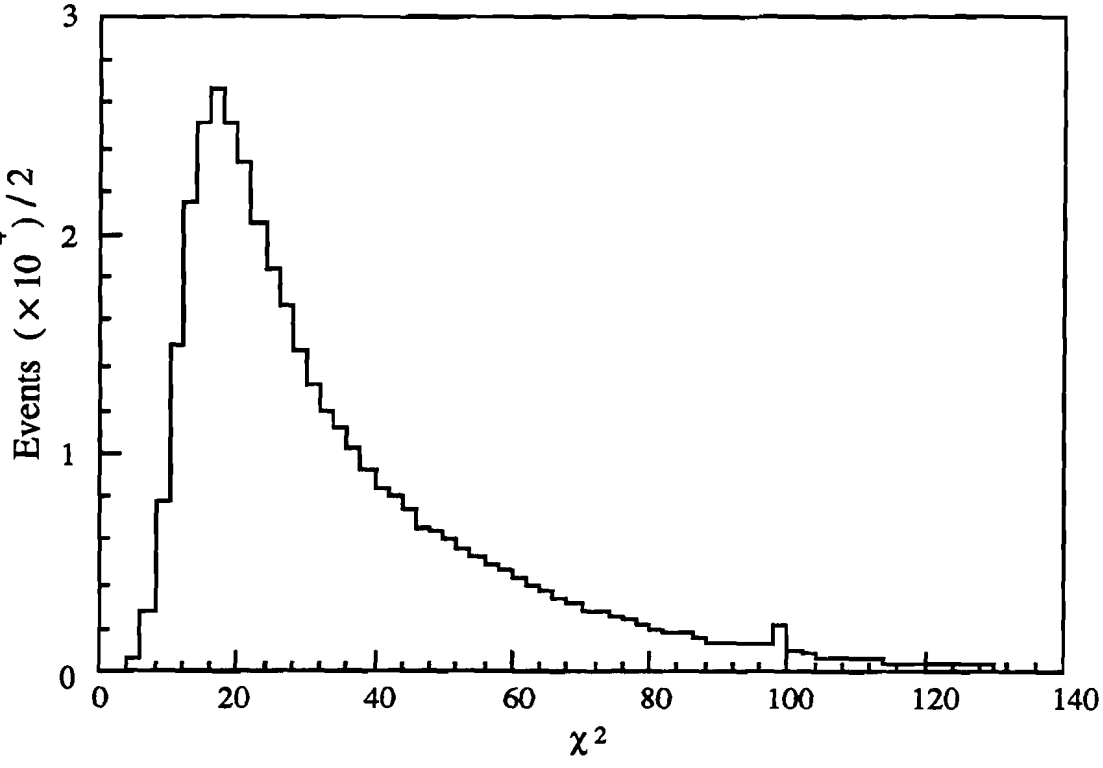

Figure 3.2 Geometric χ^2 distribution of class 0 events (for 20% of the total $\bar{\Xi}^+$ runs).

2) Target Pointing Cut

We not only required a good 3-track event, but an event with the primary particle produced by a proton at the target. The reconstructed momentum of the parent was required to trace back to within 5.5 mm from the target center. To justify this cut, the spread of the proton beam at the target was studied using single tracks in the spectrometer. All the 1-track events with no kinks and good χ^2 of fit were traced back to the target. Figure 3.3 shows the x and y projections of the tracks at the target. The full width at half maximum of the proton beam spot is about 1.4 mm ($\sigma \approx 0.6$ mm). Figure 3.4 shows the R^2 ($= x^2 + y^2$ at the target center) distribution of (a) the 1-track events (b) the 3-track sample after cut 1. Since 3-track events did not have as good resolution as 1-track, the 5.5 mm (or R^2 = 30.3 mm^2) requirement was quite reasonable. This cut removed 80% of the class 0 event sample after cut 1. That meant most of these events were produced somewhere other than the target, e.g., inside the collimator, interactions with material in the spectrometer, etc.

3) Decay Vertex Z Cut

The z position of the decay vertex of the first and second vertices, shown in Figure 3.5, indicated there was a source due to the interaction of the beam particles with the multiplicity counter M at 2331 cm. Therefore, the first and second decay vertices were required to be upstream of M counter, Z_{1st} and $Z_{2nd} < 2300$ cm. The other cut required both decay vertices to be at least 25 cm downstream of the collimator exit to avoid fringe field effects due to the magnet M1. The magnetic field of M1 dropped to a negligible level at this distance.

4) Charge Cut

This required that two particles (corresponding to two pions) bent to the $-x$ direction and the other (corresponding to proton) to the $+x$ direction after the magnet M2.

5) Momentum Cut

Based on the channel acceptance curve shown in Figure 2.3, the accepted momentum range was about 230-500 GeV/c. Events with reconstructed parent

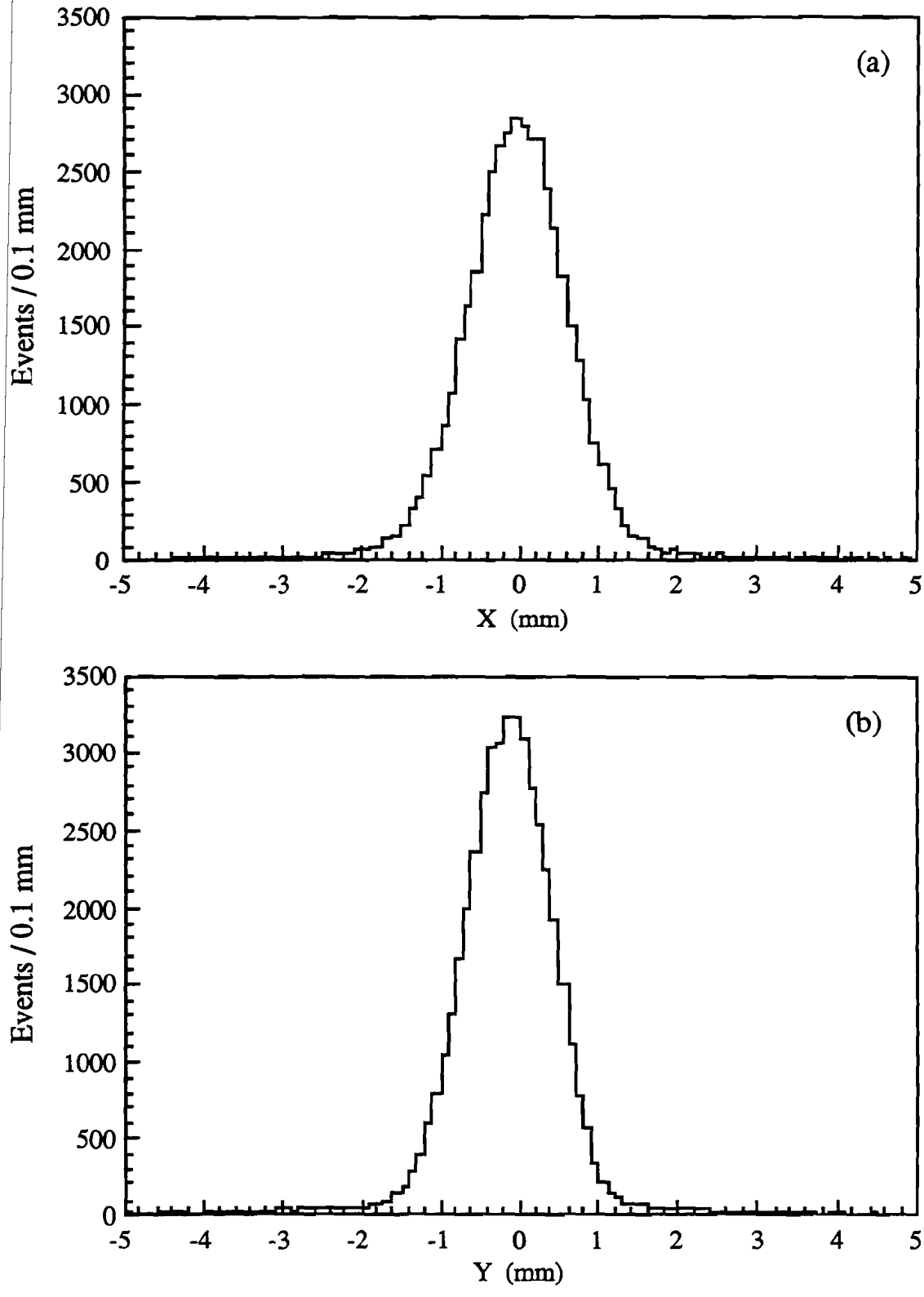

Figure 3.3 Track projection of 1-track events at target in (a) x (b) y view.

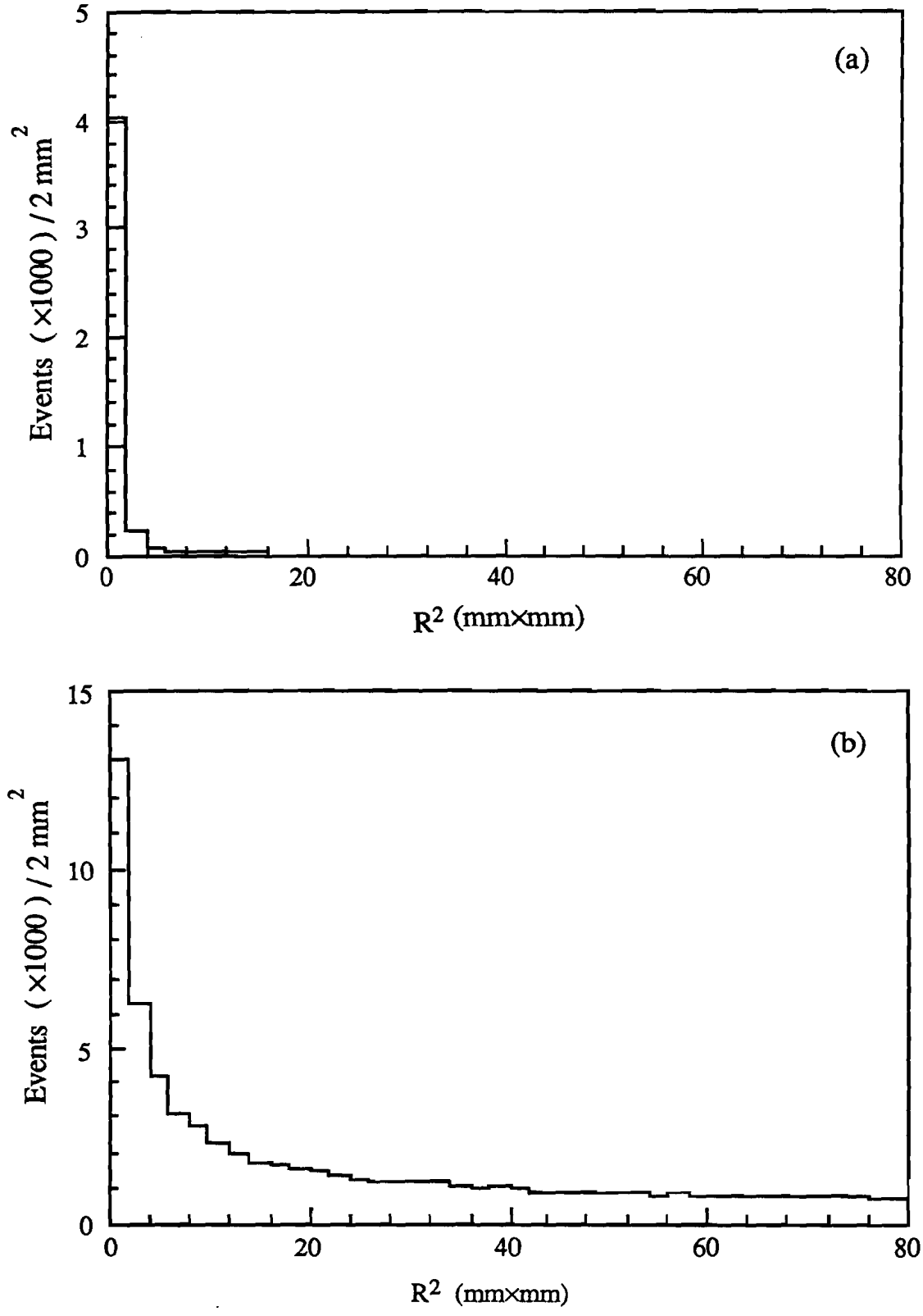

Figure 3.4 R^2 at target (a) 1-track events (b) 3-track events of $\bar{\Xi}^+$ run after Cut 1.

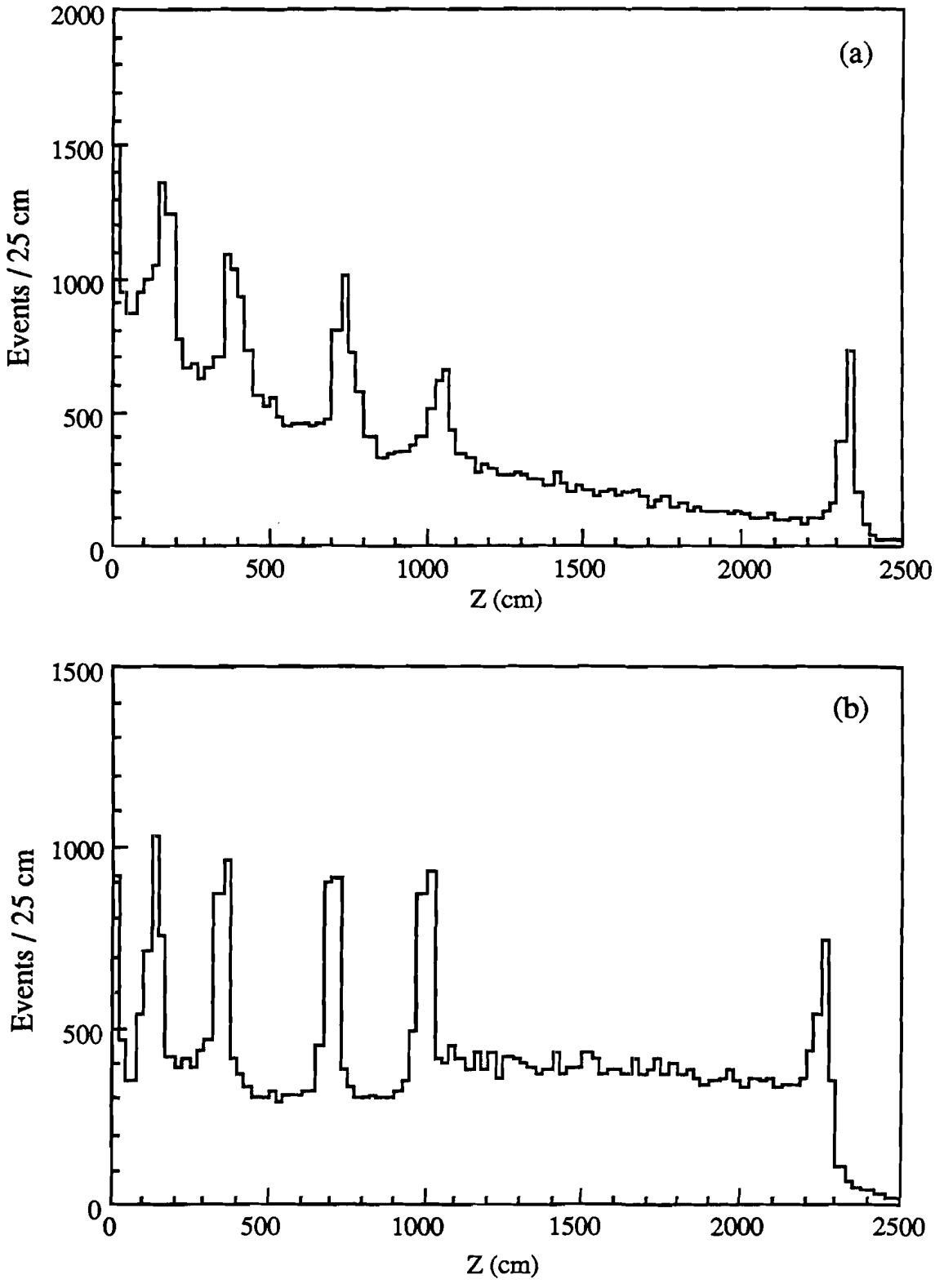

Figure 3.5 Decay vertex Z of (a) parent (b) daughter after Cut 2 (for $\bar{\Xi}^+$ run).

momentum beyond this range might be due to misreconstruction, momentum resolution, or false events. To guarantee a clean sample, only an event with parent momentum within 240-450 GeV/c and the momenta of the daughter particles less then 450 GeV/c was accepted. Figure 3.6 shows the parent momentum distribution before this cut.

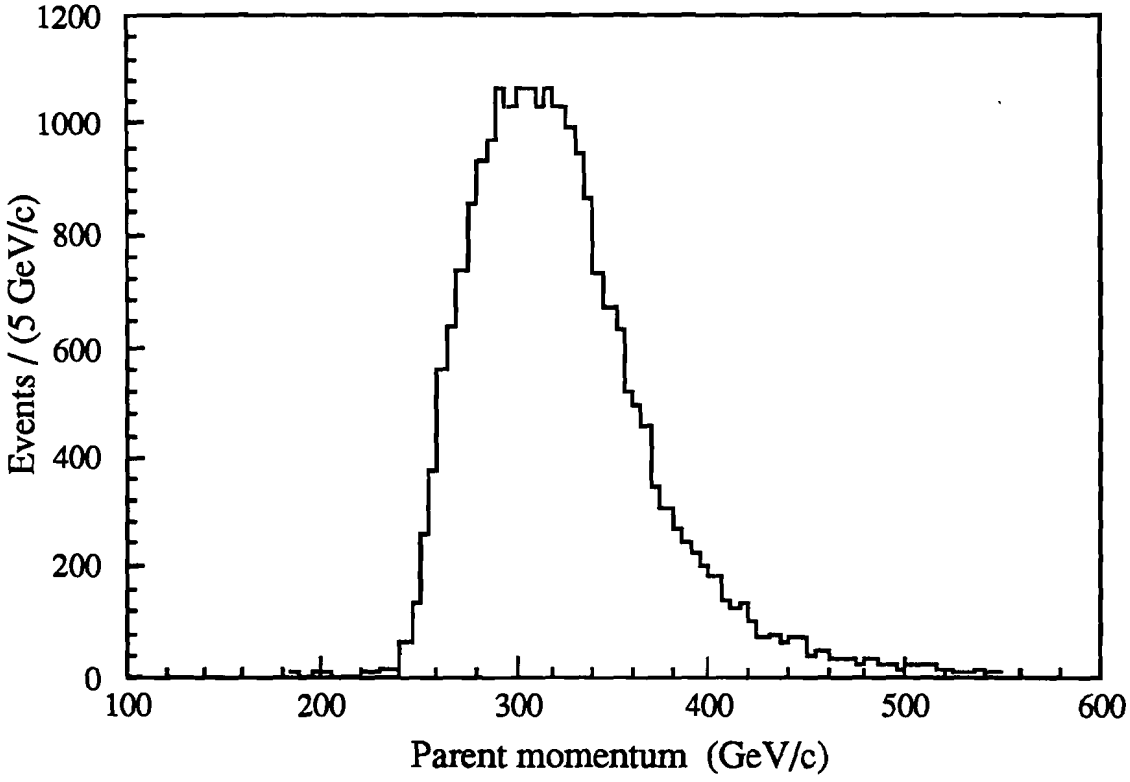

Figure 3.6 Parent momentum distribution after Cut 4 (for $\bar{\Xi}^+$ run).

6) m_Λ Cut

Since a Λ must be present in the decay sequences, the invariant mass of the proton and pion (before kinematic fit) was required to be within 10 MeV/c^2 (5σ) of m_Λ (=1115.6 MeV/c^2). Invariant mass m_{inv} is defined as $m_{inv}^2 = (E_p + E_\pi)^2 - (\mathbf{p}_p + \mathbf{p}_\pi)^2$, where m, E and **p** denote the mass, energy and momentum of the corresponding particle respectively.

7) m_{Ξ} Cut

Similarly, the invariant mass $m_{\Lambda\pi}$ of the event was required to be within 12 MeV/c^2 (5σ) of m_{Ξ} (=1321.3 MeV/c^2) after the kinematic fit.

8) m_K Cut:

At this stage the surviving 3-track events were mostly Ξ candidates. The most likely backgrounds were

$$K \rightarrow 3\,\pi \qquad (3.1)$$

$$\Omega \rightarrow \Lambda + K, \quad \Lambda \rightarrow p + \pi \qquad (3.2)$$

Figures 3.7 (a) and (b) show the invariant mass $m_{3\pi}$ and $m_{\overline{\Lambda}K}$ of the $\overline{\Xi}^+$ sample reconstructed under the hypothesis (3.1) and (3.2) respectively. It is clear that the $\overline{\Omega}^+$ contamination is negligible (m_{Ω^-} = 1.672 GeV/c^2). But a small fraction of $K^+ \rightarrow \pi^+\pi^+\pi^-$ (m_{K^+} = 493.6 MeV/c^2) still existed and was estimated to be less than 0.6% of the $\overline{\Xi}^+$ sample. The requirement of $m_{3\pi} < 510$ Mev/c^2 removed all the K^+ events, but this also removed about 0.5% of the real $\overline{\Xi}^+$. In the case of Ξ^-, both the Ω^- and K^- backgrounds were negligible. Figure 3.8 (a) and (b) show the $m_{3\pi}$ and $m_{\Lambda K}$ when Ξ^- was reconstructed as $K^- \rightarrow \pi^+\pi^-\pi^-$.and $\Omega^- \rightarrow \Lambda K^-$ respectively.

After all these cuts the background in the Ξ sample was estimated to be much less than 1%. Table 3.3 gives the distributions of the 3-track class 0 events cut out in the event selection process.

Figure 3.9 (a) shows the $\Lambda\pi$ invariant mass distribution of the $\overline{\Xi}^+$ after all software cuts except the m_{Ξ} cut, (b) is the same kind of plot of Ξ^- for comparison. Figures 3.10, 11, 12, and 13 show the distributions of the χ^2, R^2, decay vertex of $\overline{\Xi}^+$ and $\overline{\Lambda}$, and momenta of all particles after all software cuts. The two spikes in Figure 3.12, the decay vertex z distribution of $\overline{\Lambda}$, were due to the uneven allocation of the chambers. The z position of these two spikes correspond exactly to that of chamber C2 and C3 respectively. Since the distance between C3 and C4 was about 15 m, while the distance between any two chambers (or SSD) before C3 was about a few meters,

there was a high probability for the reconstruction program to fit the decay vertex close to these chambers.

Cut	(%)
1	9.3
2	79.0
3	2.6
4	3.1
5	0.2
6	0.8
7	0.6
8	0.1

Table 3.3 The distribution of class 0 events (for $\bar{\Xi}^+$ run) cut out in the event selection process.

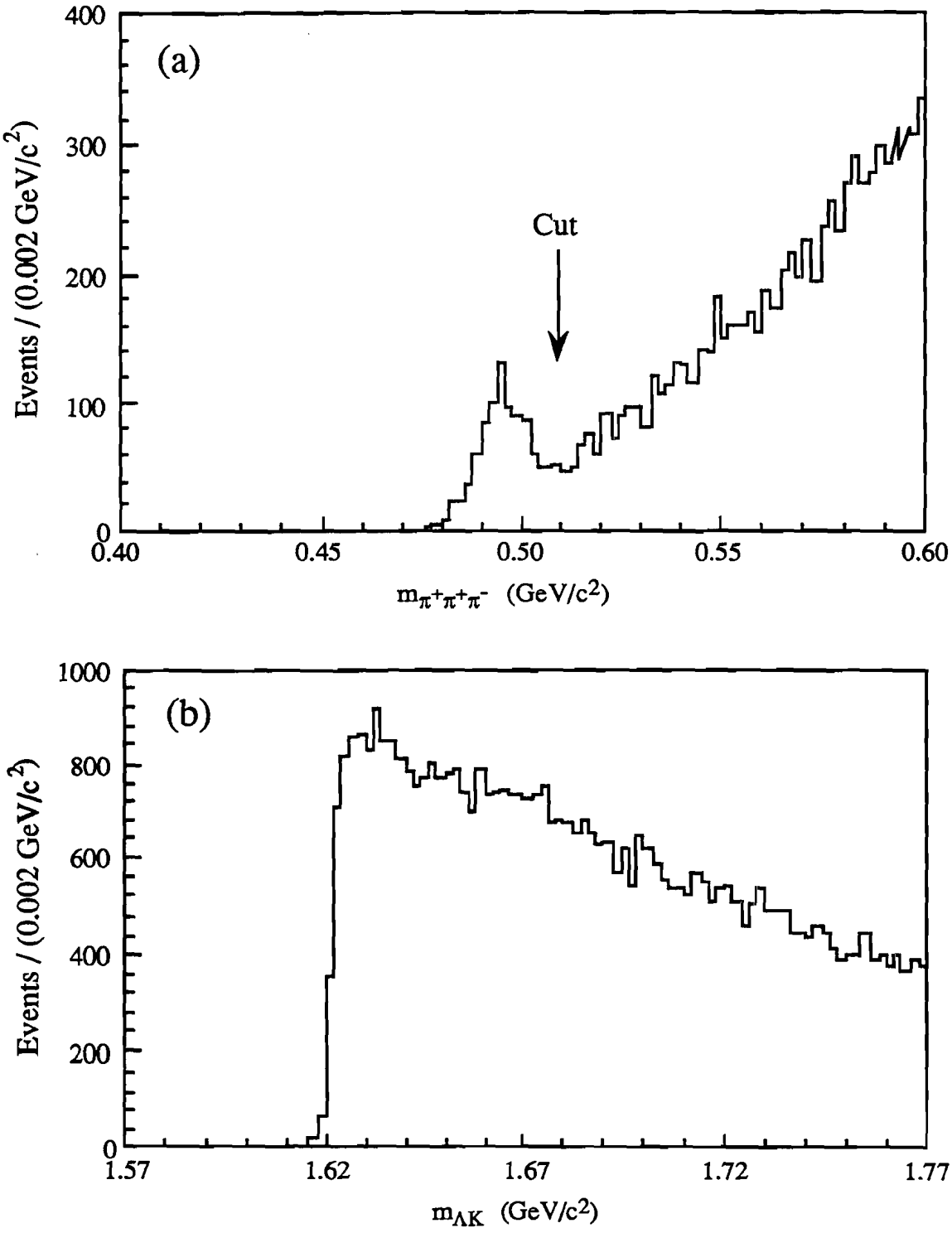

Figure 3.7 $\bar{\Xi}^+$ candidates after Cut 7 reconstructed under the hypothesis (a) $K^+ \rightarrow \pi^+\pi^+\pi^-$ (b) $\bar{\Omega}^+ \rightarrow \bar{\Lambda}^0 K^+$.

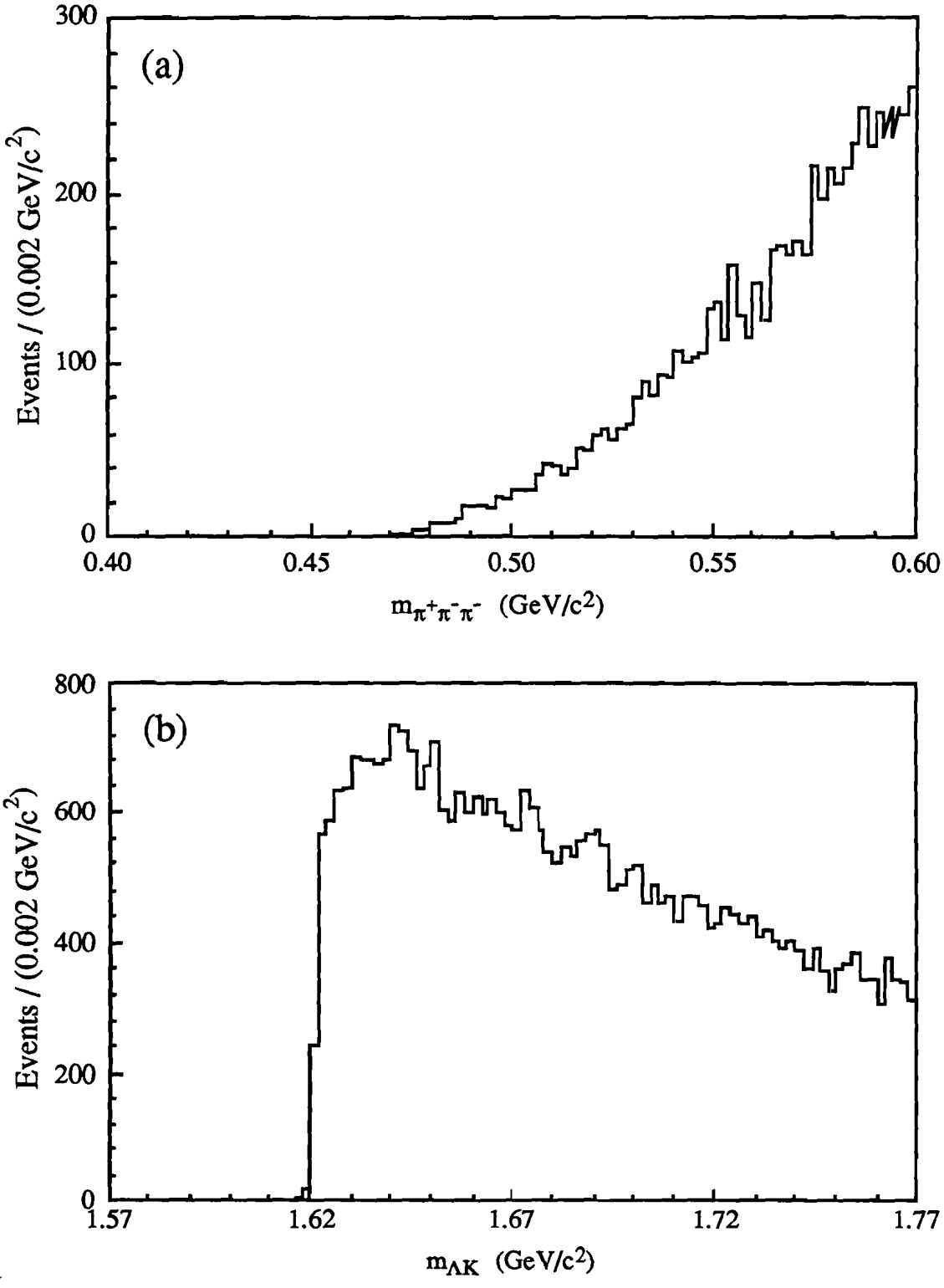

Figure 3.8 Ξ^- candidates after Cut 7 reconstructed under the hypothesis (a) $K^- \rightarrow \pi^+\pi^-\pi^-$ (b) $\Omega^- \rightarrow \Lambda^0 K^-$.

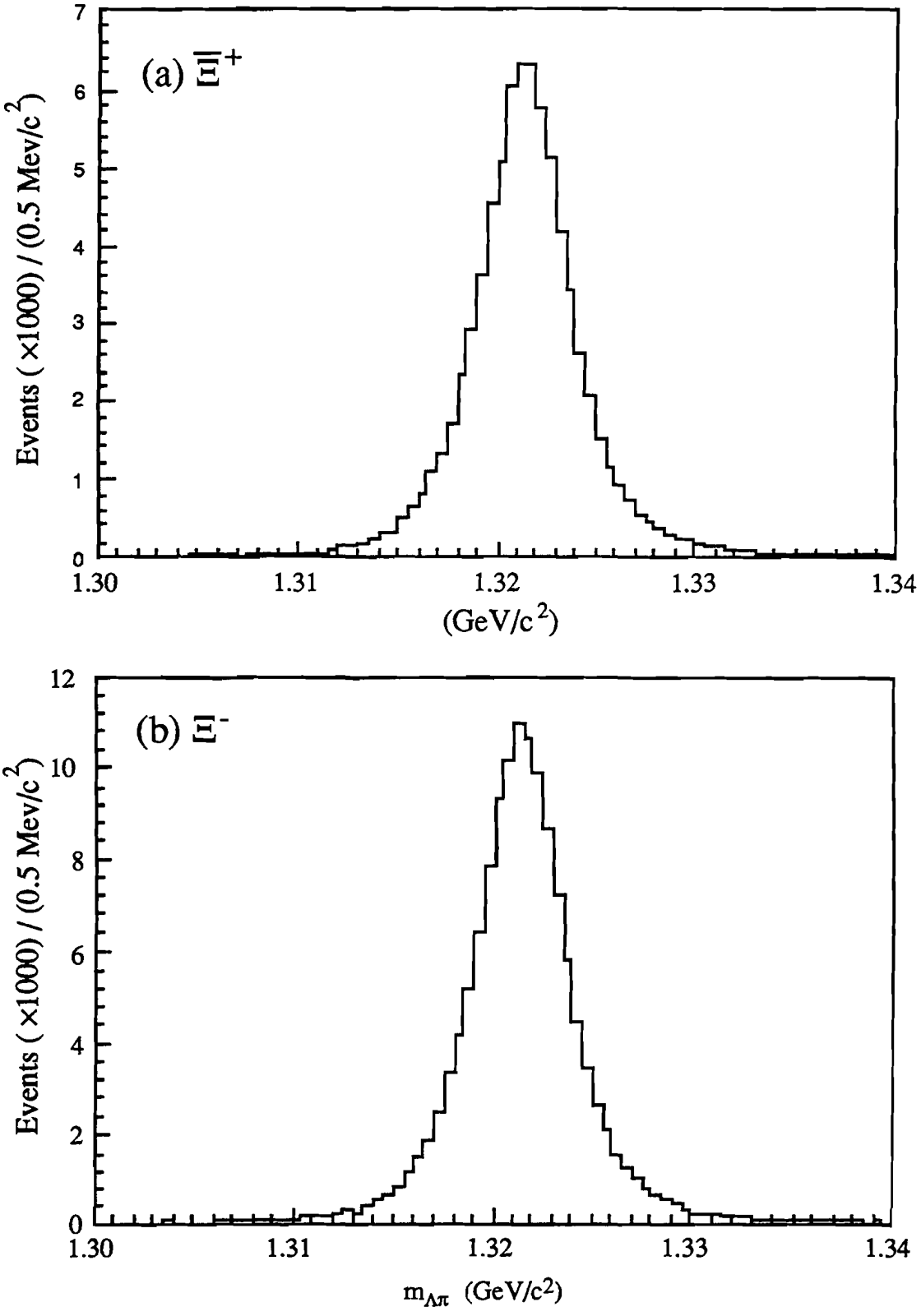

Figure 3.9 (a) $m_{\bar{\Lambda}\pi^+}$ (b) $m_{\Lambda\pi^-}$ invariant mass after all selection cuts except m_{Ξ} cut.

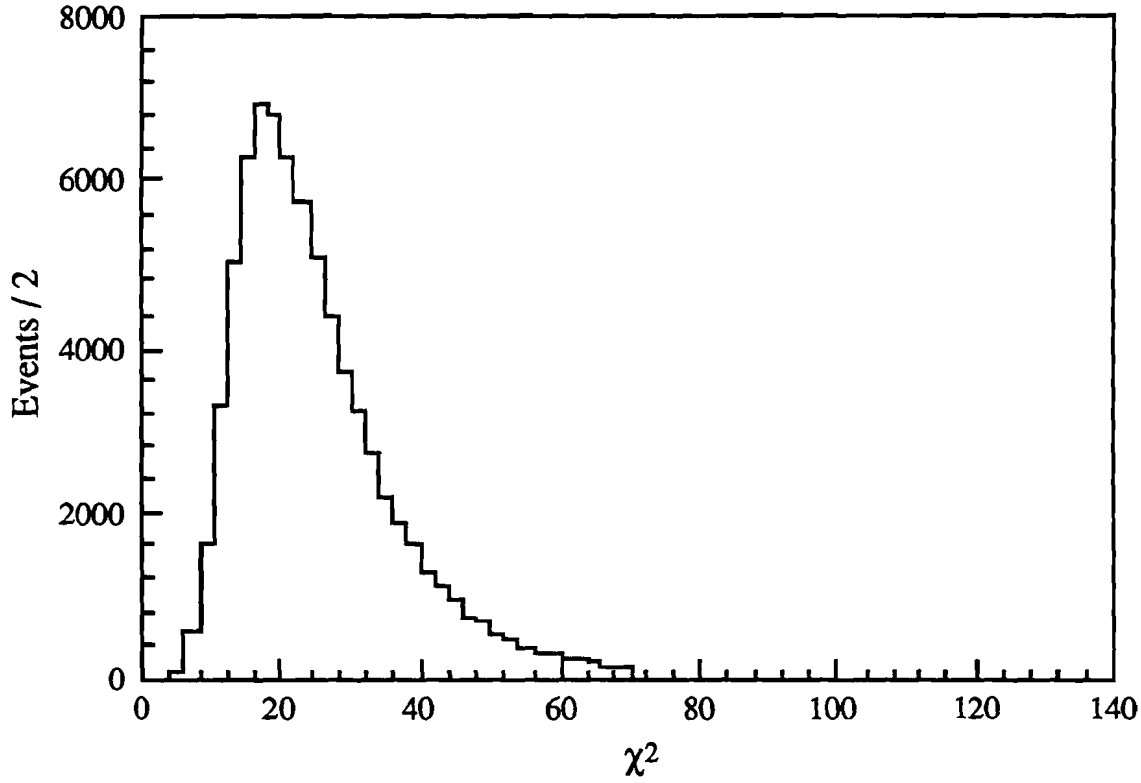

Figure 3.10 χ^2 distribution of $\bar{\Xi}^+$ events after all selection cut.

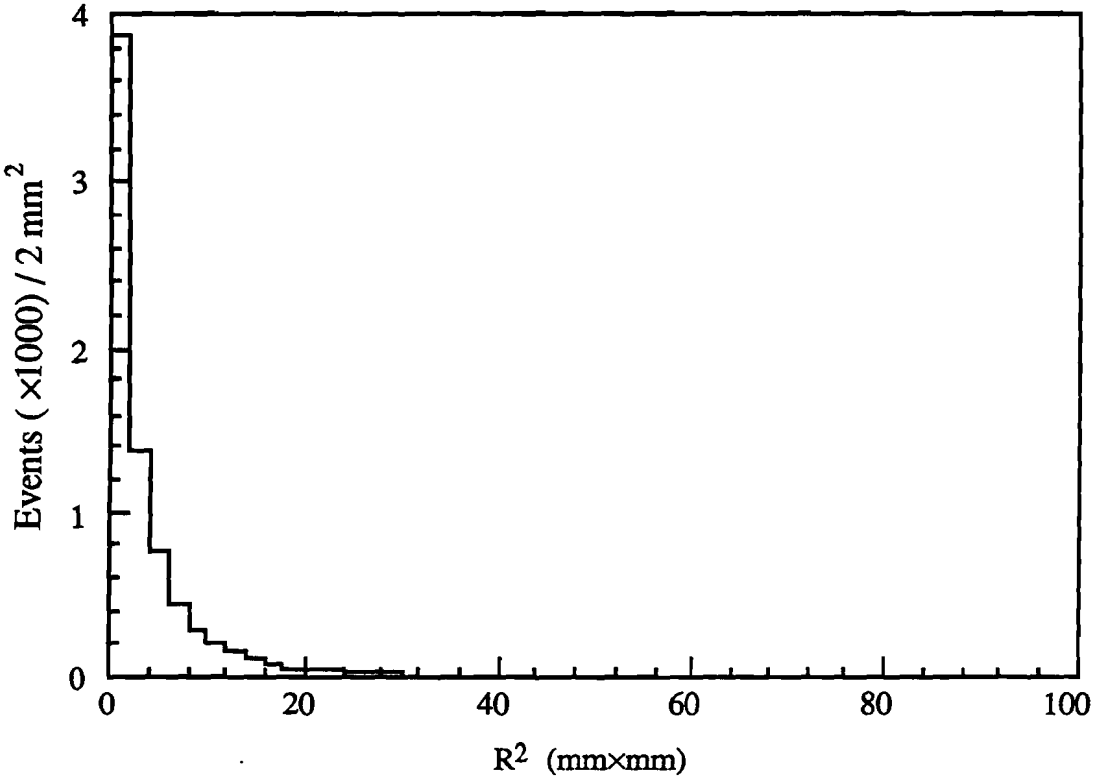

Figure 3.11 R^2 distribution of $\bar{\Xi}^+$ events after all selection cuts.

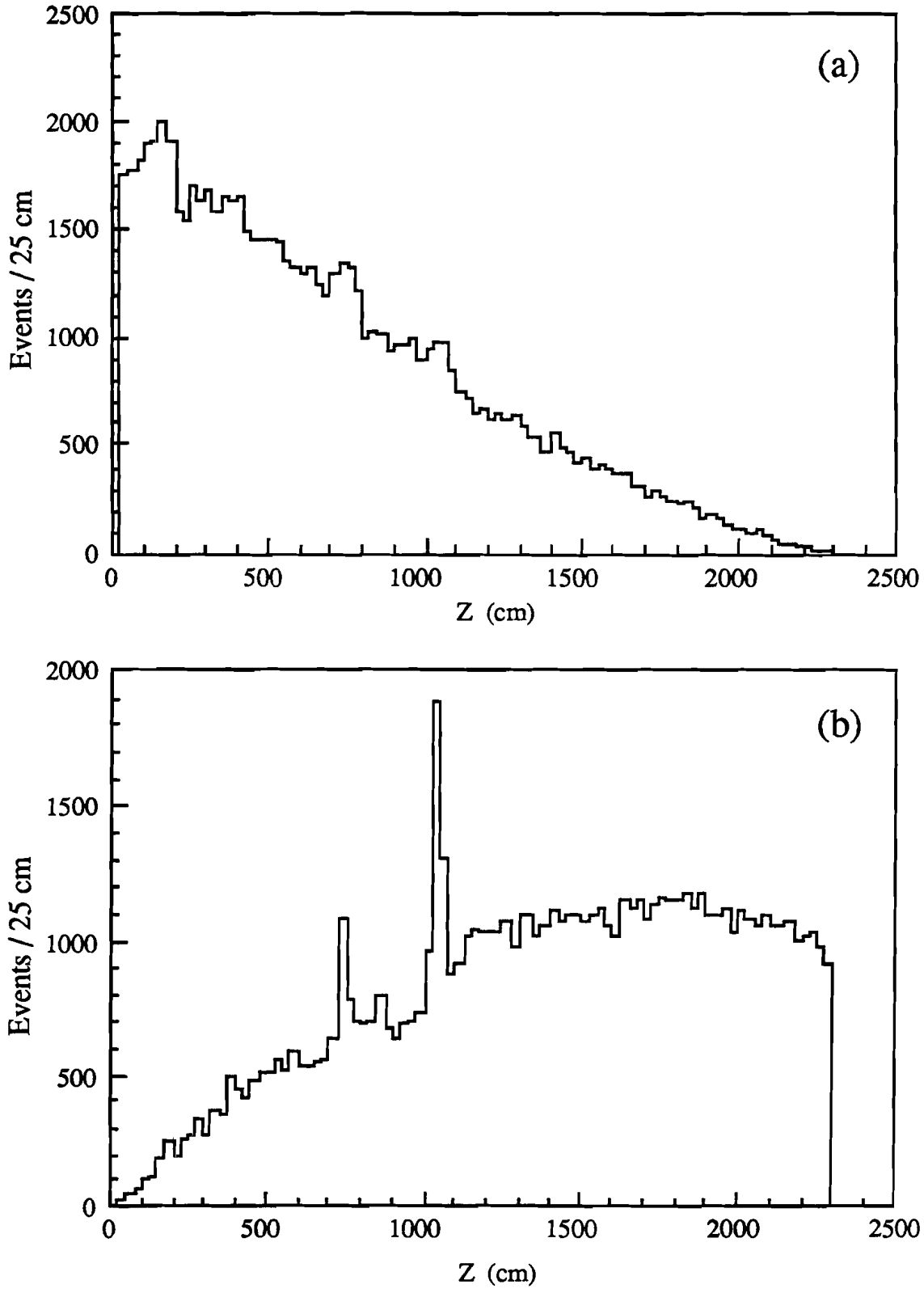

Figure 3.12 Decay vertex Z of (a) $\overline{\Xi}^+$ (b) $\overline{\Lambda}^0$ after all selection cuts.

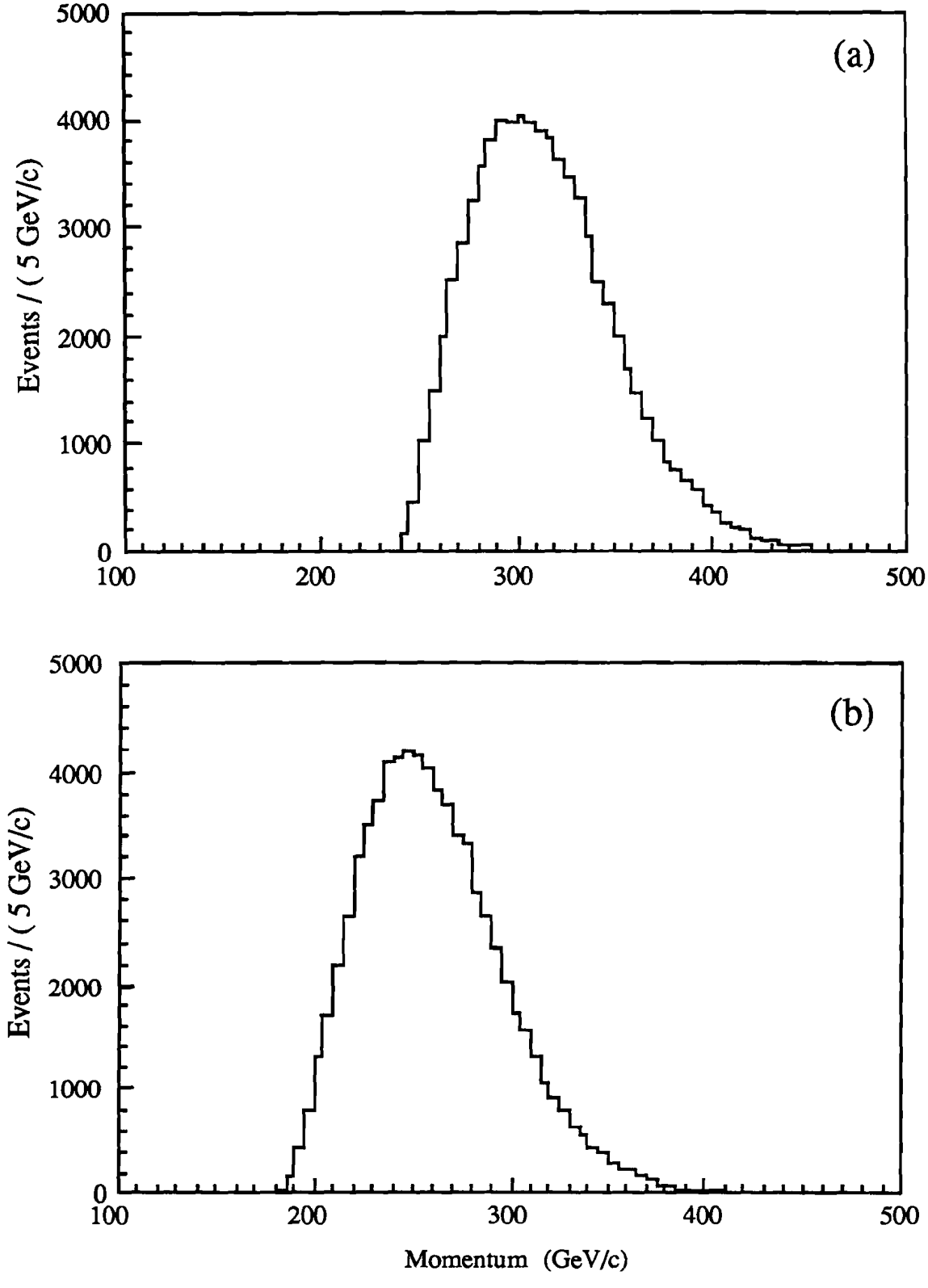

Figure 3.13 Momentum distribution of (a) $\bar{\Xi}^+$ (b) $\bar{\Lambda}^0$ after all selection cuts.

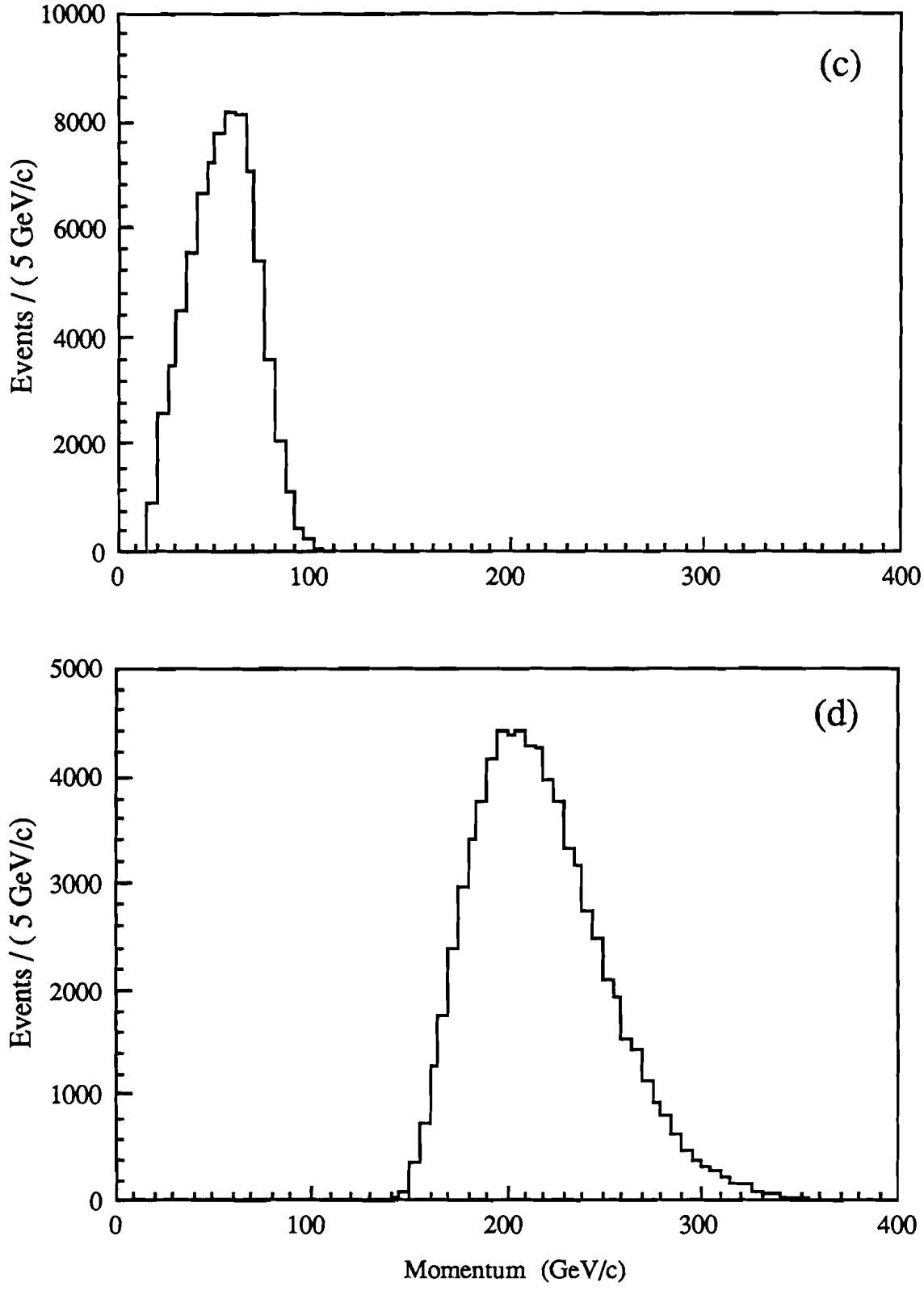

Figure 3.13 Momentum distribution of (c) π^+ from $\bar{\Xi}^+$ (d) $\bar{p}$ after all selection cuts.

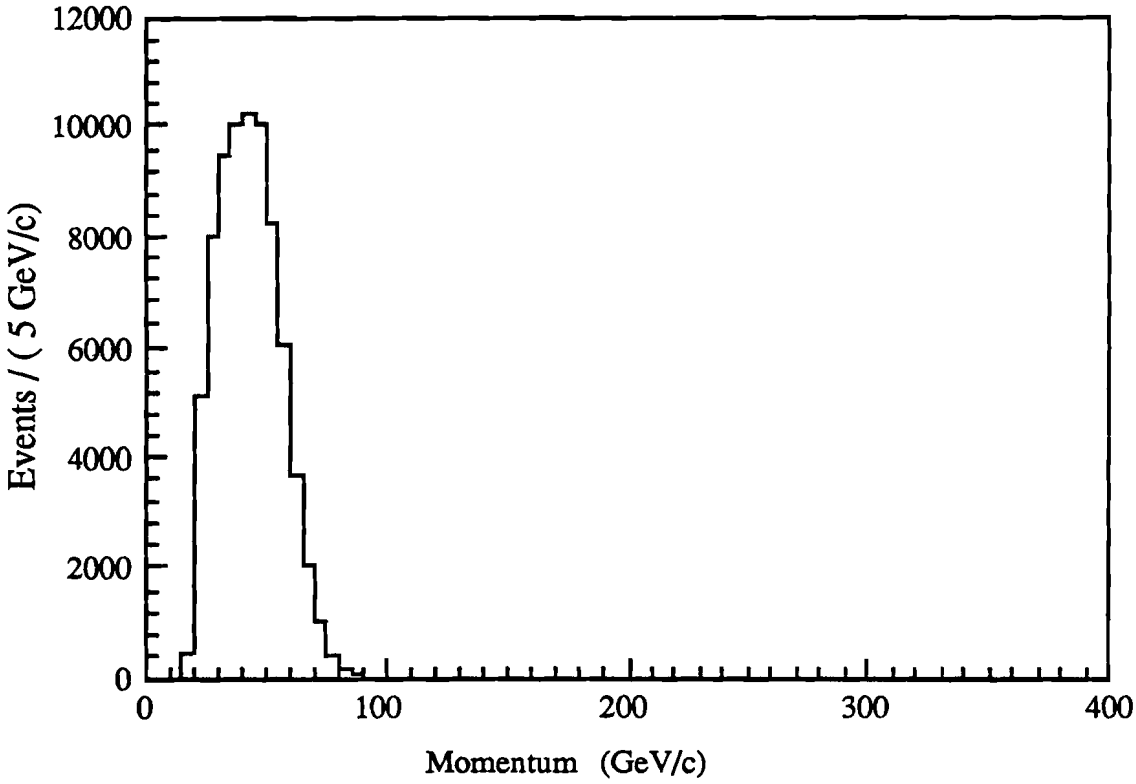

Figure 3.13 (e) Momentum distribution of π^+ from $\overline{\Lambda}^0$after all selection cuts.

CHAPTER 4

POLARIZATION ANALYSIS

4.1 Introduction

After a clean sample of Ξ's was selected, the immediate question was how to extract the polarization signal from the reconstructed information. The idea was fairly simple. In the Ξ decay sequences : $\Xi \rightarrow \Lambda\, \pi$, $\Lambda \rightarrow p\, \pi$, the polarization of the parent P_Ξ was related to that of its daughter P_Λ which was determined from the decay proton distribution. In this chapter, the relation between P_Ξ and P_Λ is first described. A quick and intuitive analysis of the Ξ polarization follows. Lastly, a polarization analysis method, the hybrid Monte Carlo technique, will be discussed in detail.

4.2 Ξ Polarization

The decay of $\Xi \rightarrow \Lambda\, \pi$, $\Lambda \rightarrow p\, \pi$ can be formulated in a more general case, a spin 1/2 particle decaying weakly into spin 1/2 and spin 0 particles.

$$\text{spin } 1/2 \rightarrow \text{spin } 1/2 + \text{spin } 0 \qquad (4.1)$$

The total angular momenta of the initial and final states are :

$$J_{in} = 1/2 \qquad (4.2)$$

$$\begin{aligned} J_f &= L + S \\ &= L + 1/2 + 0 \\ &= L + 1/2 \end{aligned} \qquad (4.3)$$

where **L** is the orbital angular momentum of the two-particle final state, and **S** is the spin of the daughter particles. Conservation of the total angular momentum in the decay process requires $J_{in} = J_f$. This constrains **L** to be $L = 0$ (called s-wave) or $L = 1$ (p-wave). Therefore the final state is a mixture of s and p waves, i.e.,

$$\Psi_f = A_s\Psi_s + A_p\Psi_p \qquad (4.4)$$

where Ψ is a state wave function. A_s and A_p are amplitudes, which are complex numbers in general, of the s and p state wave functions respectively.

Two useful relations can be derived for the decay of the type (4.1). The first one is the relation between the polarization of the parent and that of its daughter particle. In the case of Ξ decay [25]

$$\mathbf{P}_\Lambda = \frac{\alpha_\Xi \hat{\mathbf{\Lambda}} + \gamma_\Xi \mathbf{P}_\Xi + (1-\gamma_\Xi)(\mathbf{P}_\Xi \cdot \hat{\mathbf{\Lambda}})\hat{\mathbf{\Lambda}} + \beta_\Xi \hat{\mathbf{\Lambda}} \times \mathbf{P}_\Xi}{1 + \alpha_\Xi \mathbf{P}_\Xi \cdot \hat{\mathbf{\Lambda}}} \qquad (4.5)$$

where $\hat{\mathbf{\Lambda}}$ is the momentum unit vector of the Λ in the Ξ rest frame, $\mathbf{P}_\Lambda$ and $\mathbf{P}_\Xi$ are the polarization vectors of Λ and Ξ in their own rest frames respectively, α_Ξ, β_Ξ and γ_Ξ are asymmetry parameters of Ξ which are defined as

$$\alpha_\Xi = \frac{2\mathbf{Re}(A_s^* A_p)}{|A_s|^2 + |A_p|^2}$$

$$\beta_{\Xi} = \frac{2\,\mathrm{Im}(A_s^* A_p)}{|A_s|^2 + |A_p|^2}$$

$$\gamma_{\Xi} = \frac{|A_s|^2 - |A_p|^2}{|A_s|^2 + |A_p|^2} \qquad (4.6)$$

Note that

$$\alpha_{\Xi}^2 + \beta_{\Xi}^2 + \gamma_{\Xi}^2 = 1 \qquad (4.7)$$

The experimental values of these parameters[26] for Ξ^- are $\alpha_{\Xi^-} = -0.456 \pm 0.014$, $\gamma_{\Xi^-} = 0.89$ ($\beta_{\Xi^-} \approx 0$). In the case of $\bar{\Xi}^+$, $\alpha_{\bar{\Xi}^+} = -\alpha_{\Xi^-}$, $\beta_{\bar{\Xi}^+} = -\beta_{\Xi^-}$, and $\gamma_{\bar{\Xi}^+} = \gamma_{\Xi^-}$ as required by CP invariant.[27] If the β_{Ξ} term is neglected, Eq. (4.5) can be written as

$$\mathbf{P}_{\Lambda} = \frac{\alpha_{\Xi}\hat{\mathbf{\Lambda}} + \gamma_{\Xi}\mathbf{P}_{\Xi} + (1-\gamma_{\Xi})(\mathbf{P}_{\Xi}\cdot\hat{\mathbf{\Lambda}})\hat{\mathbf{\Lambda}}}{1 + \alpha_{\Xi}\mathbf{P}_{\Xi}\cdot\hat{\mathbf{\Lambda}}} \qquad (4.8)$$

The second general relation is the distribution of the daughter in the parent's rest frame.

$$\frac{dN}{d\Omega} = \frac{1}{4\pi}(1 + \alpha\mathbf{P}\cdot\hat{\mathbf{n}}) \qquad (4.9)$$

$$= \frac{1}{4\pi}(1 + \alpha P_z\cos\theta + \alpha P_x\sin\theta\cos\varphi + \alpha P_y\sin\theta\sin\varphi) \qquad (4.10)$$

where $\mathbf{P}$ is the polarization of the parent, and $\hat{\mathbf{n}}$ is the momentum unit vector of the daughter in the parent's rest frame. Eq. (4.10) is the same equation as Eq. (4.9) expressed in spherical coordinates. θ is the angle between the z-axis and $\hat{\mathbf{n}}$, and φ is the azimuthal angle. Integrating both sides of Eq. (4.10) with respect to φ from 0 to 2π

$$\int_0^{2\pi} \frac{dN}{d\Omega} d\varphi = \frac{dN}{d\cos\theta} = \frac{1}{2}(1 + \alpha P_z\cos\theta) \qquad (4.11)$$

Since any axis can be chosen as the z-axis, we have

$$\frac{dN}{d\cos\theta_i} = \frac{1}{2}(1 + \alpha P_i \cos\theta_i) \qquad i = x, y, z \qquad (4.12)$$

In the case of $\Lambda \rightarrow p\,\pi$

$$\frac{dN}{d\cos\theta_i} = \frac{1}{2}(1 + \alpha_\Lambda P_{\Lambda i} \cos\theta_i) \qquad (4.13)$$

where $\cos\theta$ is the direction cosine of p in Λ's rest frame. Therefore $\mathbf{P}_\Lambda$ can be determined from the distribution of the daughter proton, and then one can determine $\mathbf{P}_\Xi$ by using Eq. (4.8).

4.3 A qualitative and Simple analysis

4.3.1 A qualitative analysis

It has been shown that $\mathbf{P}_\Xi$ can be determined from the proton distribution in the Λ rest frame, which has the form

$$\frac{dN}{d\cos\theta} = \frac{1}{2}(1 + \alpha P \cos\theta) \qquad (4.14)$$

Since Eq. (4.14) is a linear equation, αP is just the slope of a straight line. Figure 4.1 shows $dN/d(\cos\theta)$ vs. $\cos\theta$ in different cases of αP. But this is only true when the geometric acceptance and reconstruction efficiency of Ξ are 100%.

In reality, the $\cos\theta$ distribution of the proton was convoluted with the acceptance and resolution of the apparatus in the observed $\cos\theta$ distribution. Figure 4.2 shows the $\cos\theta$ distribution of a sample of unpolarized Monte Carlo events after reconstruction. These $\cos\theta$ distributions need some explanation. The dip at $\cos\theta_x \approx 0$ corresponded to $\cos\theta_z \approx \pm 1$, i.e., the proton and pion lay in the proximity of the $\pm$ z-axis

in the Λ rest frame. After the momenta of p and π were transformed back to the lab frame, the opening angle between them was very small. Due to the finite resolution of the detectors and the reconstruction program algorithm, most of these events could not be reconstructed efficiently. Furthermore, a forward proton in the Λ rest frame ($\cos\theta_z = 1$) implied a very low momentum pion in the lab frame, which would be most likely buried inside the magnet M2. But a backward-going proton ($\cos\theta = -1$) meant a high momentum pion in the lab which would have a higher chance to pass through M2. This explains why there were more losses at $\cos\theta_z \approx 1$ than at -1 in Figure 4.2 (b). These kind of failed events corresponded to classes 7, 8, and 9 described in Table 3.1. The high (low) population in $\cos\theta_x < 0$ ($\cos\theta_x > 0$) was also due to the spectrometer acceptance, not a polarization effect. When the proton traveled to $+x$ (i.e., $\cos\theta_x > 0$), the pion traveled to - x. Since M2 would bend the pion toward - x, many of these pions could not fall within the active area of C8 or they might not get through M2. These kind of events consisted of class 8 and 10 failures. But those pions which went to + x, corresponding to $\cos\theta < 0$ of the proton, would usually get through M2.

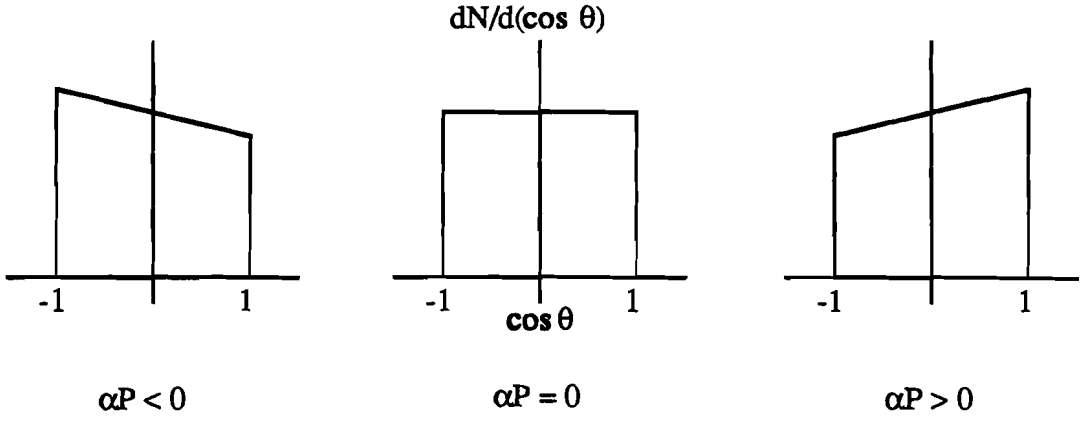

Figure 4.1 $(1+\alpha P \cos\theta)$ vs. $\cos\theta$ for $\alpha P < 0$, $\alpha P = 0$, $\alpha P > 0$.

Since the observed $\cos\theta$ distribution was distorted by the acceptance, it was not so straightforward to measure αP. But a qualitative analysis can still be carried out easily. Since the polarization vector will flip sign when the production angle is reversed, the difference in the $\cos\theta$ distributions between the positive and negative

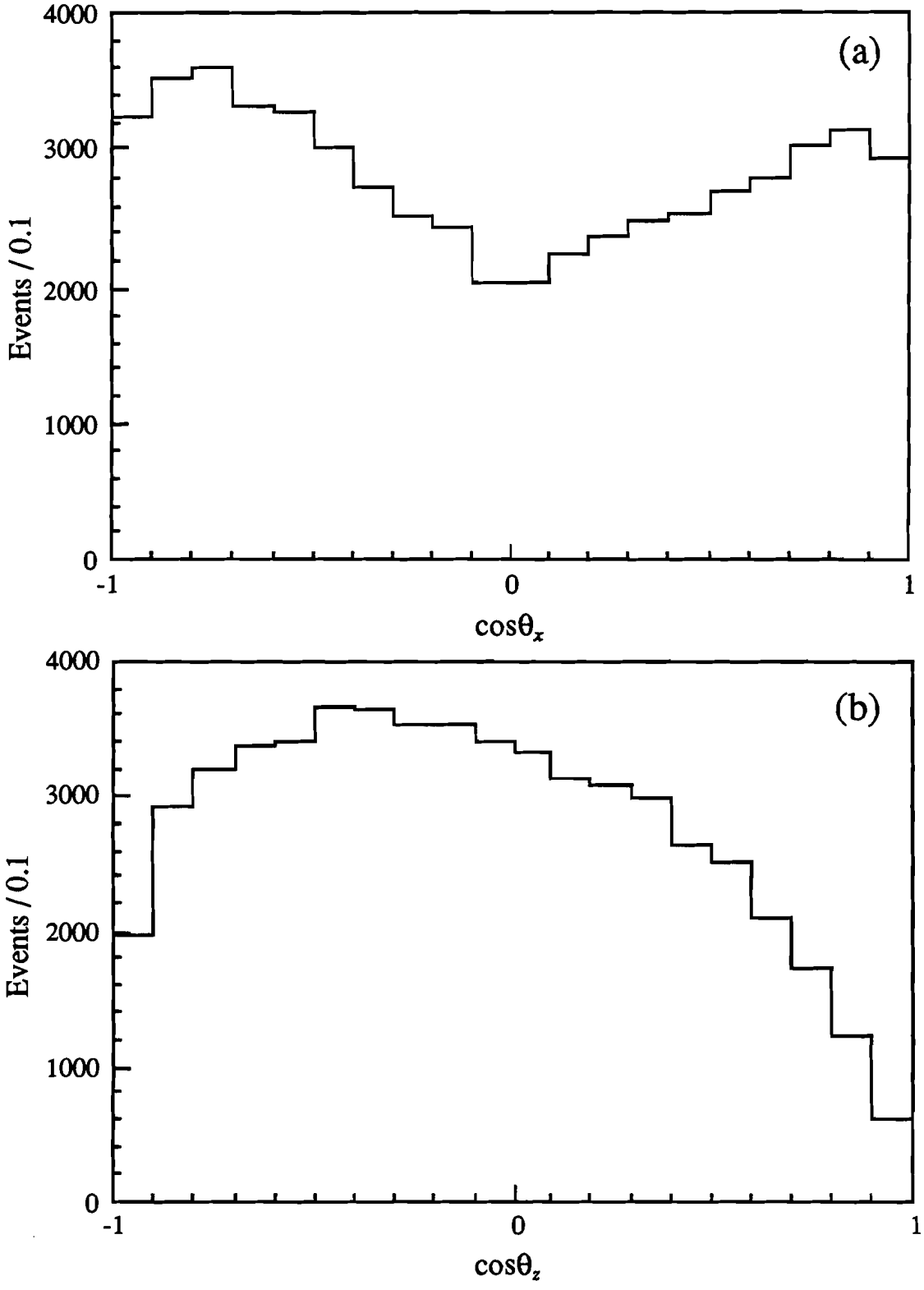

Figure 4.2 Reconstructed (a) $\cos\theta_x$ (b) $\cos\theta_z$ distribution of unpolarized Monte Carlo events.

production angle data would indicate the presence of polarization. Figure 4.3 shows the comparison of the cosθ distribution of two samples with opposite production angles and perfect geometric acceptance and reconstruction efficiency. It is clear that there is an excess of events for $\cos\theta < 0$ when $\alpha P < 0$ but the opposite when $\alpha P > 0$.

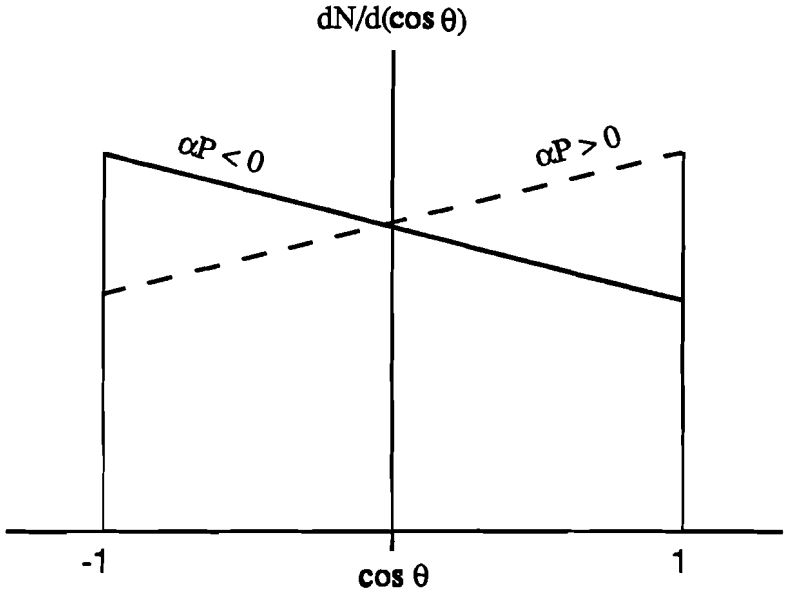

Figure 4.3 Comparison of $(1 + \alpha P \cos\theta)$ of two samples with equal but opposite production angles and perfect geometric acceptance and reconstruction efficiency.

In Figure 4.4(a) and (b) we compare the observed $\cos\theta_x$ distribution for the positive and negative production angles for $\bar{\Xi}^+$ and Ξ^- decays. In these figures the positive angle data were normalized to the negative angle data. There were 32,000 (38,000) $\bar{\Xi}^+$'s and 62,000 (60,000) Ξ^-'s for the positive (negative) angle in our data samples. The differences in the $\cos\theta_x$ distribution between the two angles show an unambiguous polarization signal for both $\bar{\Xi}^+$ and Ξ^-.

As a check, 42,000 (48,000) $K^+ \rightarrow \pi^+\pi^+\pi^-$ events for the positive (negative) production angle, collected concurrently with the $\bar{\Xi}^+$, were reconstructed with the π^- and

(i) a randomly chosen π^+

(ii) the lower momentum π^+,

to form a "particle" Q. The $\cos\theta_x$ distributions of the π^- in the Q rest frame are shown in Figure 4.4 (c) and (d) for combinations (i) and (ii). As expected, no difference is observed between the positive and negative angles since K^+ is a spin 0 particle.

4.3.2 A Sample Calculation

Since the observed $\cos\theta$ distribution was convoluted with acceptance and resolution, Eq. (4.14) should be modified as follows

$$N_j^{\pm}(\cos\theta) = \frac{N}{4\pi} F_j^{\pm}(\cos\theta)(1 \pm \alpha P\cos\theta) \tag{4.15}$$

where $F_j(\cos\theta)$ is the acceptance function in the j^{th} $\cos\theta$ bin which accounts for the distortion of $\cos\theta$ distribution from a linear distribution, and "±" means 'positive' and 'negative' production angles. N_j is the number of particles in the j^{th} bin (after appropriate normalization), and N is the total number of events. From Eq. (4.15) we have

$$\frac{N^+ - N^-}{N^+ + N^-} = \frac{F^+(1+\alpha P\cos\theta) - F^-(1-\alpha P\cos\theta)}{F^+(1+\alpha P\cos\theta) + F^-(1-\alpha P\cos\theta)}$$

If the acceptance of the spectrometer is the same with respect to the production angle, i.e., $F^+(\cos\theta) = F^-(\cos\theta)$, then

$$R \equiv \frac{N^+ - N^-}{N^+ + N^-} = \alpha P\cos\theta \tag{4.16}$$

Again, this is a linear equation in $\cos\theta$. In Figure 4.5, R is plotted against $\cos\theta_x$ for (a) $\bar{\Xi}^+$, (b) Ξ^-, (c) K^+ for case i, and (d) K^+ for case ii. The fit to a straight line is excellent. The chi-square per degree of freedom is shown in each figure.

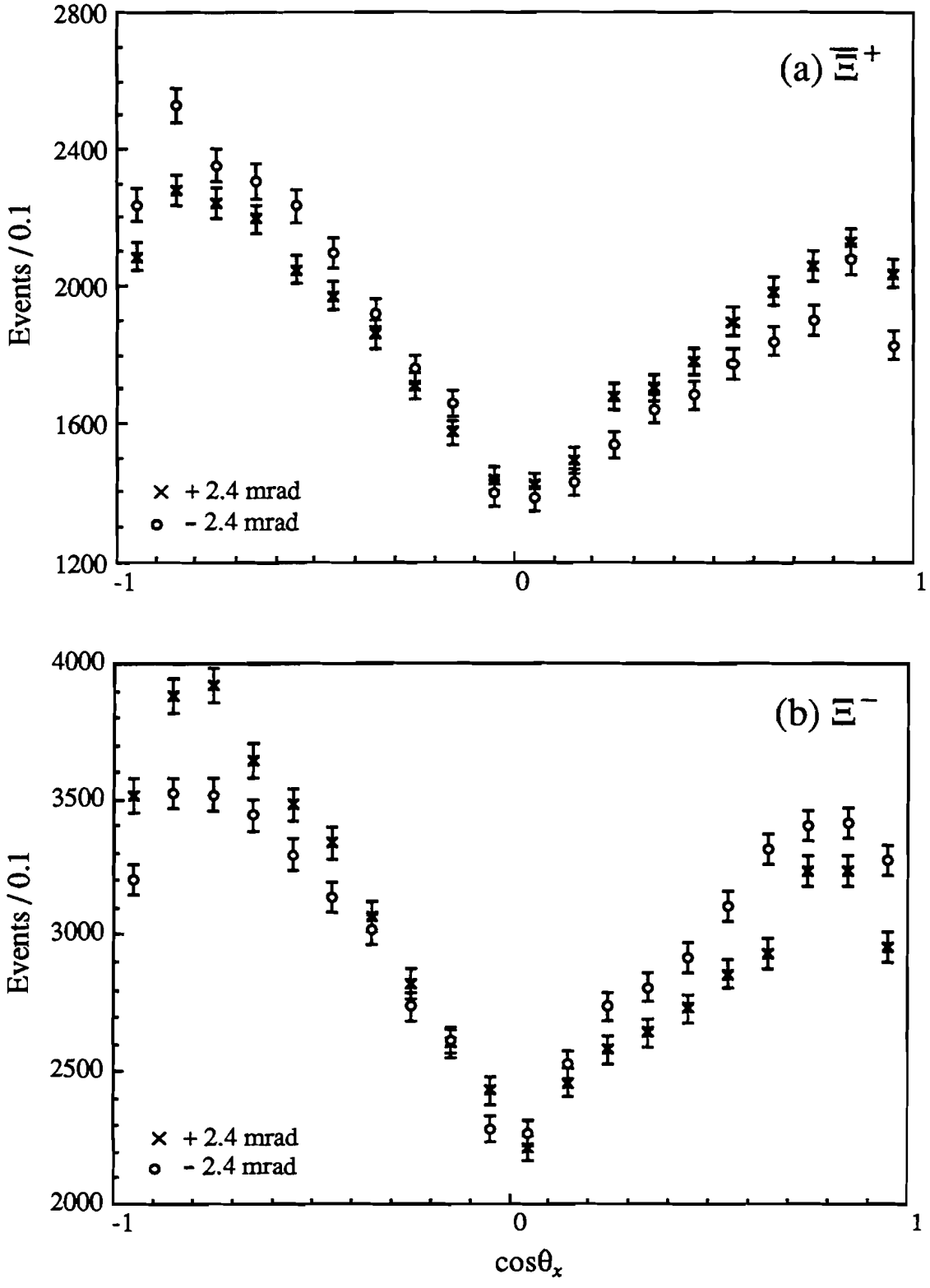

Figure 4.4 Comparison of $\cos\theta_x$ between '±' production angles for (a) $\bar{\Xi}^+$ (b) Ξ^-.

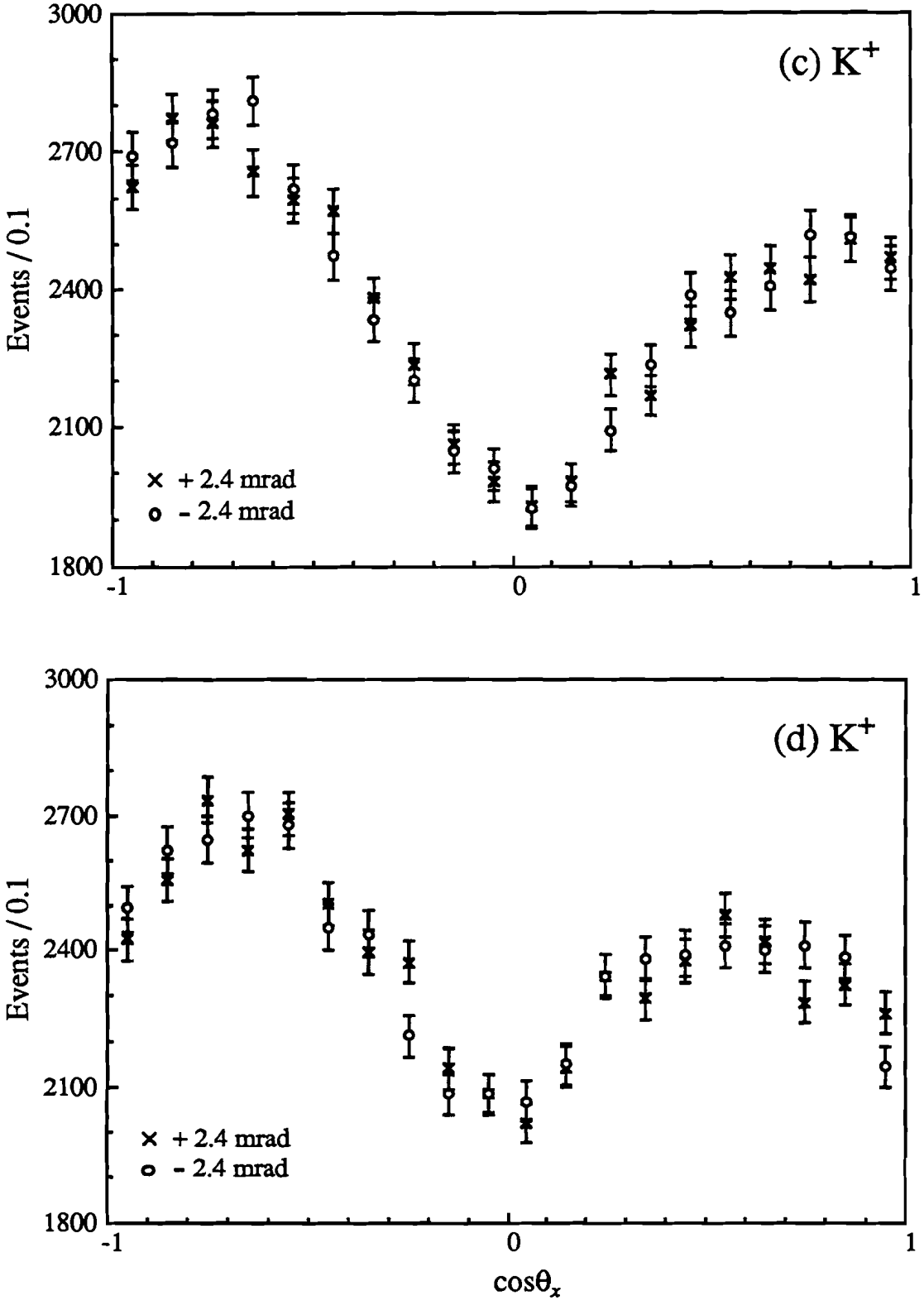

Figure 4.4 $Cos\theta_x$ comparison for '±' production angles of K^+ in (c) case i (d) case ii.

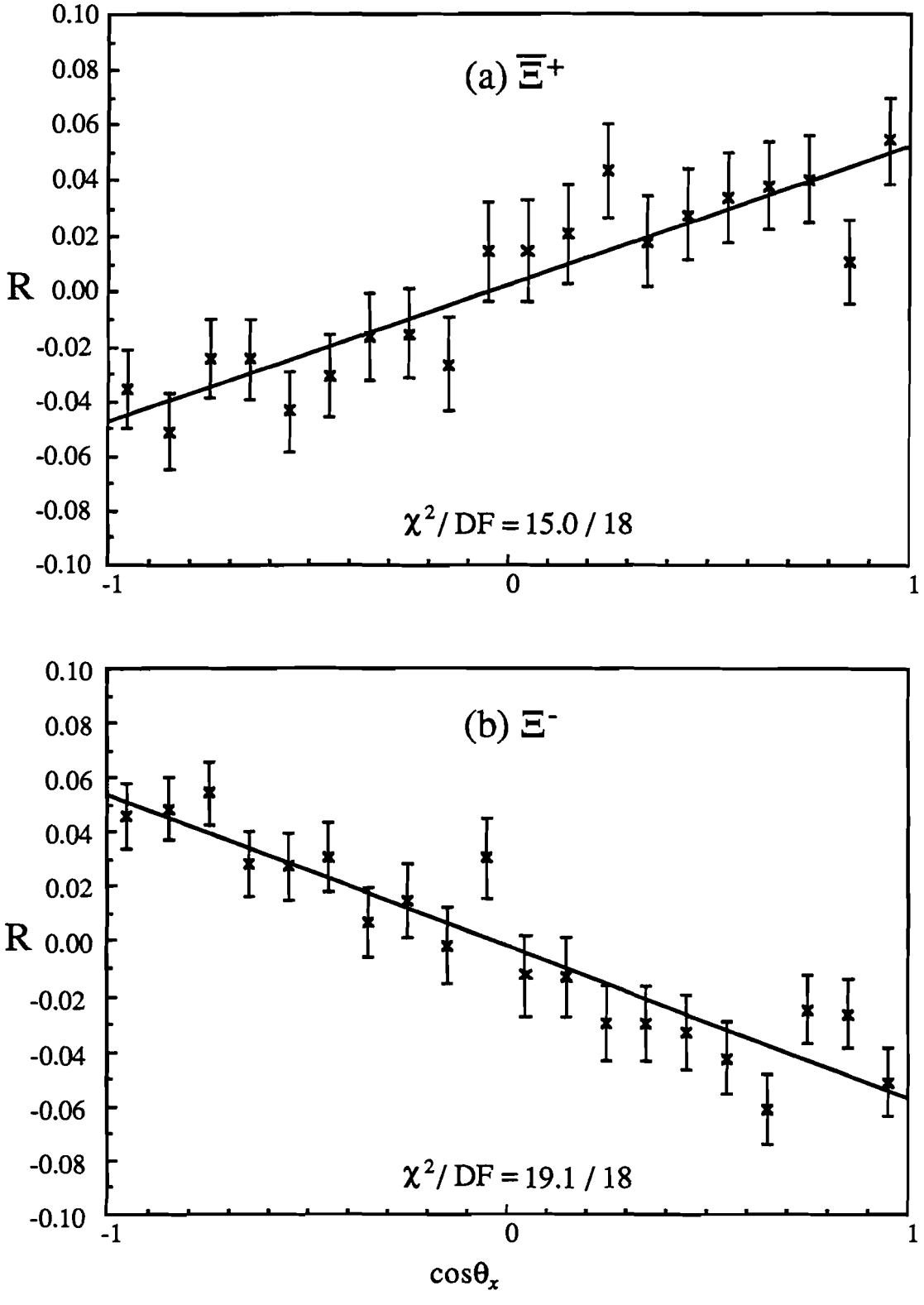

Figure 4.5 R vs. cosθ$_x$ for (a) $\bar{\Xi}^+$ (b) Ξ^-. R is defined as $(N^+-N^-)/(N^++N^-)$.

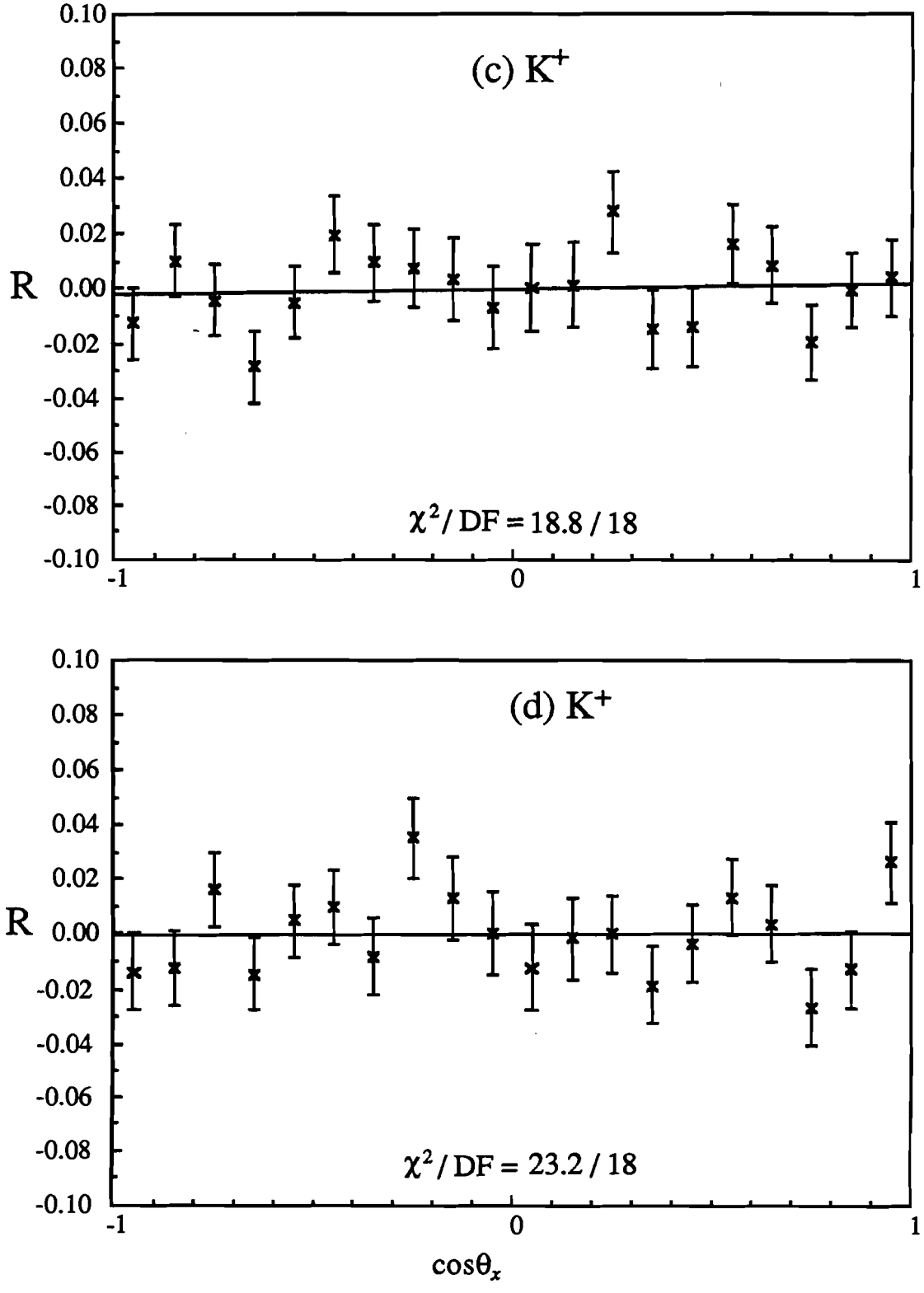

Figure 4.5 R vs. $\cos\theta_x$ for K^+ in (c) case i (d) case ii.

The drawback of this method is that it cannot take the kinematic effects into account and may give a false signal. For example, in this experiment protons hit the target at +2.4 mrad in the *yz*-plane, i.e., the beam shooting upward (+*y* direction). Therefore most of the massive particles like Ξ, Λ and proton tend to travel along this direction, corresponded to a higher concentration of events at $\cos\theta_y > 0$. Figure 4.6 shows the *y*-component of the Ξ momentum. Similarly, there were more events for $\cos\theta_y < 0$ when the production angle was reversed. When Eq. (4.16) was applied to the $\cos\theta_y$ distribution, it would yield a large value of αP_y (the slope). But this would violate parity conservation since $\mathbf{P}_y$ was not normal to the production plane. Fig 4.7 shows $\alpha P_y \cos\theta_y$ vs. $\cos\theta_y$ and the straight line fit for Ξ^-, $\bar{\Xi}^+$ and K^+. This shows Ξ^- and $\bar{\Xi}^+$ have a large polarization signal in the *y* component as explained above. The same sign of slope is due to kinematic effects (only depends on production angle), not physics. On the other hand, the αP_y for K^+ in case (i) and (ii) are both close to zero. This occurs since the three daughter particles have equal mass so that each has equal probability to go to any direction after a Lorentz boost. Again this is a kinematic effect.

4.4 Hybrid Monte Carlo Method

4.4.1 The Algorithm

The idea of using a Monte Carlo (MC) method[28] to determine the asymmetry αP is quite straightforward. A sample of unpolarized MC events (uniform distribution in $\cos\theta$) was first generated. The geometric and reconstruction acceptance were folded into the event generator. By comparing the $\cos\theta$ distribution of the MC and real event sample, the symmetry αP was extracted when the MC sample was required to have the same $\cos\theta$ distribution as real data.

A standard Monte Carlo simulates all variables in an experiment, e.g., decay distribution, production angle, and momentum distribution, etc. There are at least two disadvantages of using such a generation method. First, it is very time consuming since most of the generated events will be lost because of the acceptances of the

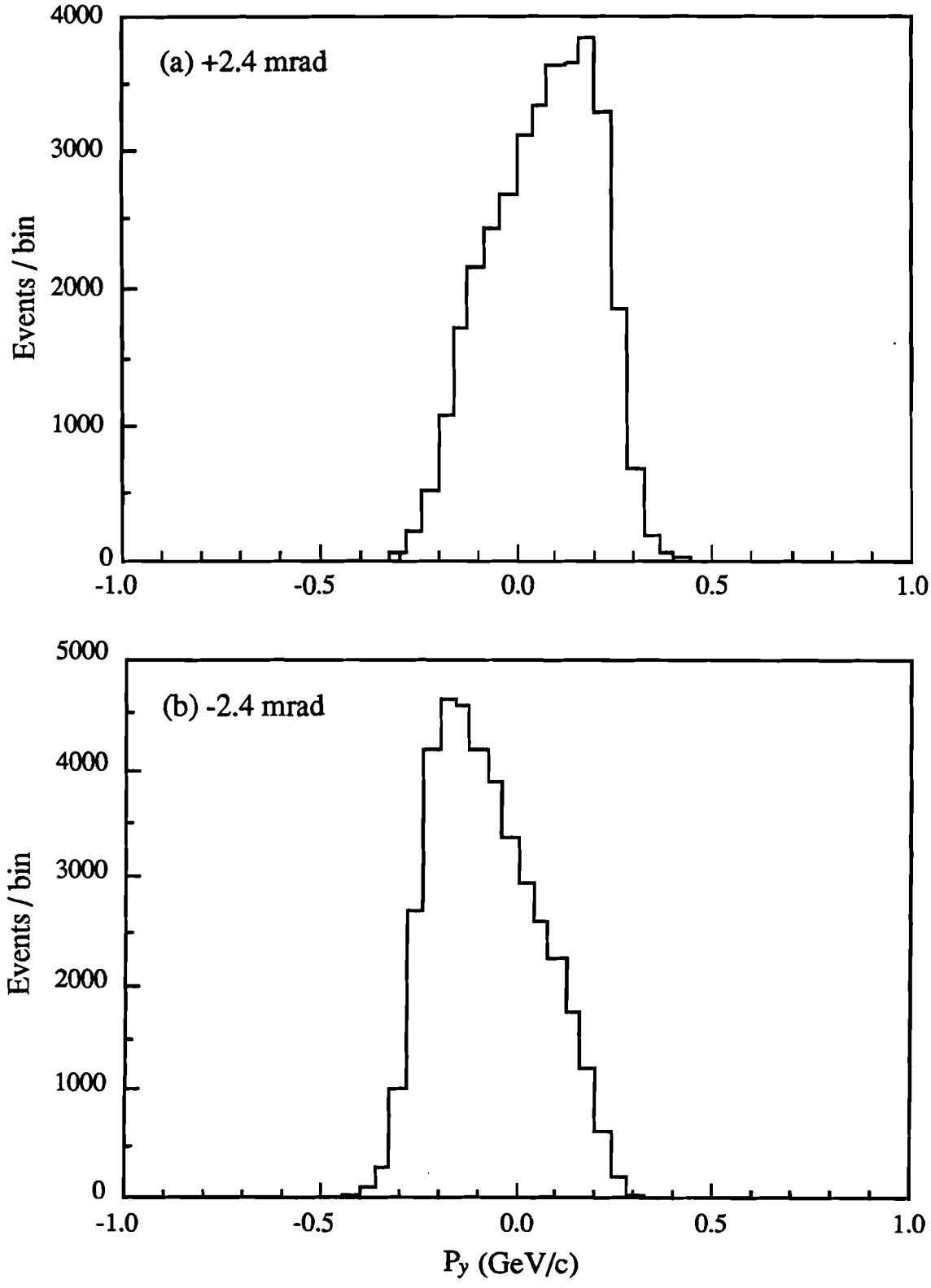

Figure 4.6 y-component of $\bar{\Xi}^+$ momentum at (a) +2.4 (b) -2.4 mrad.

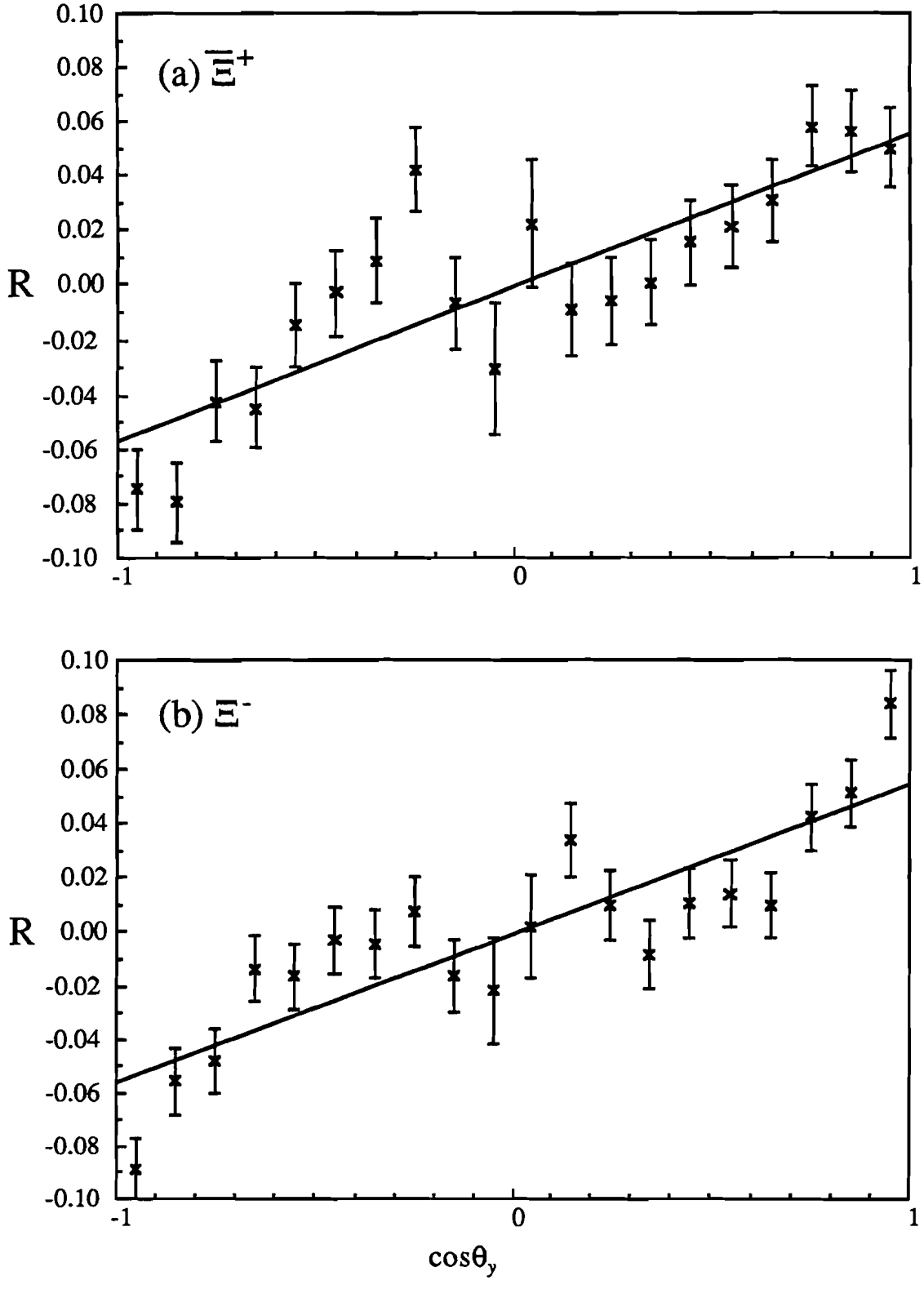

Figure 4.7 R vs. $\cos\theta_y$ for (a) $\bar{\Xi}^+$ (b) Ξ^-. R is defined as $(N^+-N^-)/(N^++N^-)$.

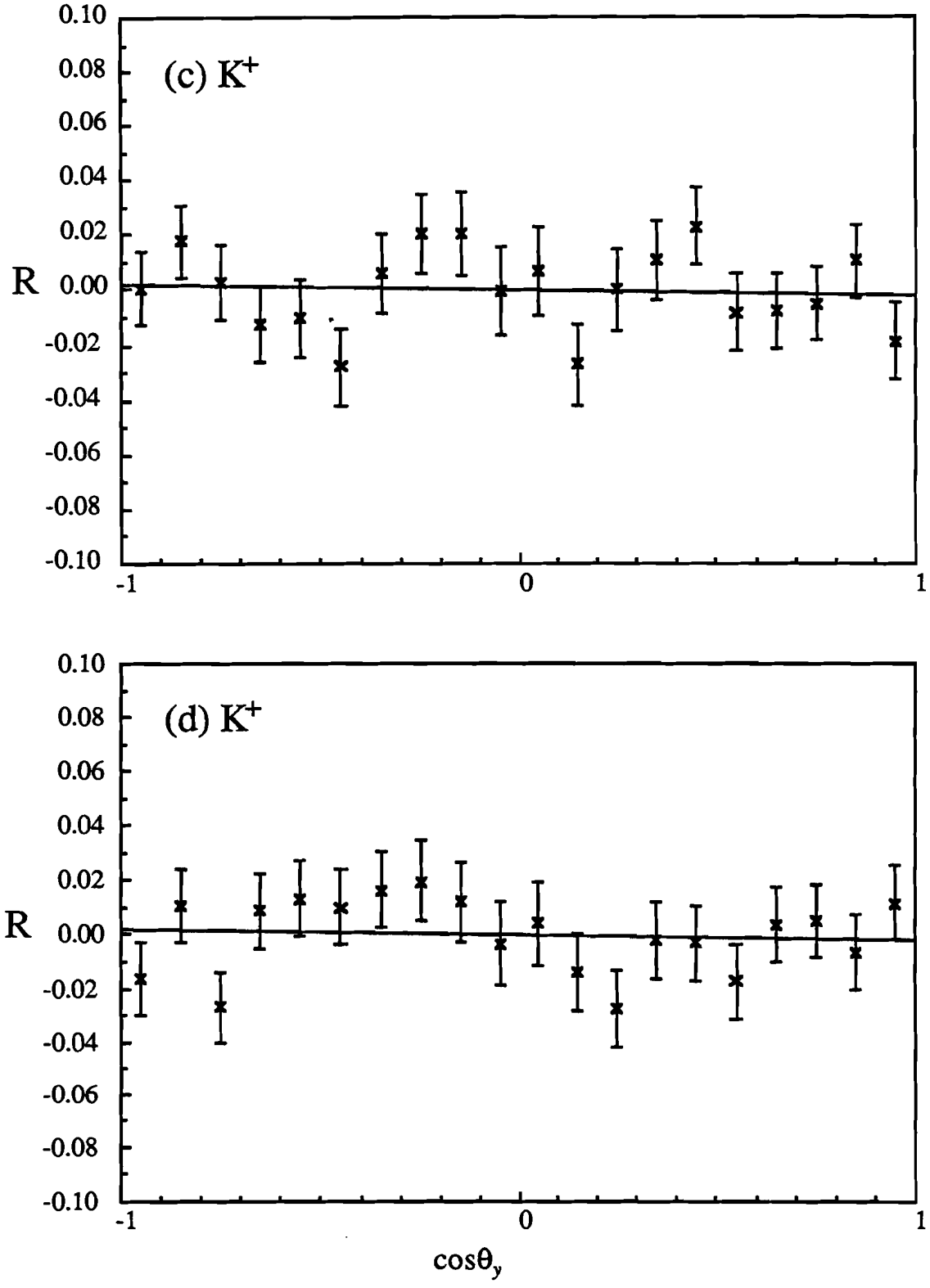

Figure 4.7 R vs. $\cos\theta_y$ for K^+ in (c) case i (d) case ii.

collimator, the spectrometer and the reconstruction. Second, some variables are simply not known a priori, e.g., the production cross sections of the particles we want to study. The goal of a Hybrid Monte Carlo is to simulate the variables which are important to the physics result, and the remaining variables are simply taken from the data. In our case, αP was the variable we wished to determine, and the rest of the variables were taken from the data. From here on, HMC means Hybrid Monte Carlo, and HMC events are called " fake " events.

Figure 4.8 shows the logic flow of the polarization analysis. The real event part was well described in the last chapter except the 'Acceptance Cut'. This cut required that events had to clear the geometrical aperture of the detectors and the software trigger logic. Therefore, almost all the real events passed through this cut. This cut was basically set up for the fake events.

For each real event, some number of fake events were generated. The $\cos\theta$ (of each fake event) of the proton in the Λ rest frame (with respect to x, y, or z axis, one at a time) was generated randomly from -1 to 1. With the azimuthal angle φ of the proton in the Λ rest frame, as well as the momentum of Λ and Ξ taken from the real data, the momentum of the daughter of Λ, namely p and π, in the lab could be calculated. These momenta together with the reconstructed momentum of the decay π from Ξ, as well as the decay vertex positions of Ξ and Λ were used to determine the x and y hit positions and then the corresponding wire numbers (digitization) of all the charged tracks in the detectors. These fake events would then go through the same analysis programs (reconstruction, selection and acceptance cut) as the real data. If the fake event was accepted, its reconstructed $\cos\theta$ of the proton in the Λ rest frame would be stored in a summing array for the determination of αP after all the real events were processed. Five such fake events were generated for each real event. Five is an arbitrary number; it only means the fake sample is 5 times bigger than the real one, it can be any reasonable number. Since the generated fake event might fail in any step of the process, 200 tries were allowed before 5 fake events were accepted. Otherwise, these fake events and the corresponding real event were discarded from the analysis. About 1% of real events were rejected this way.

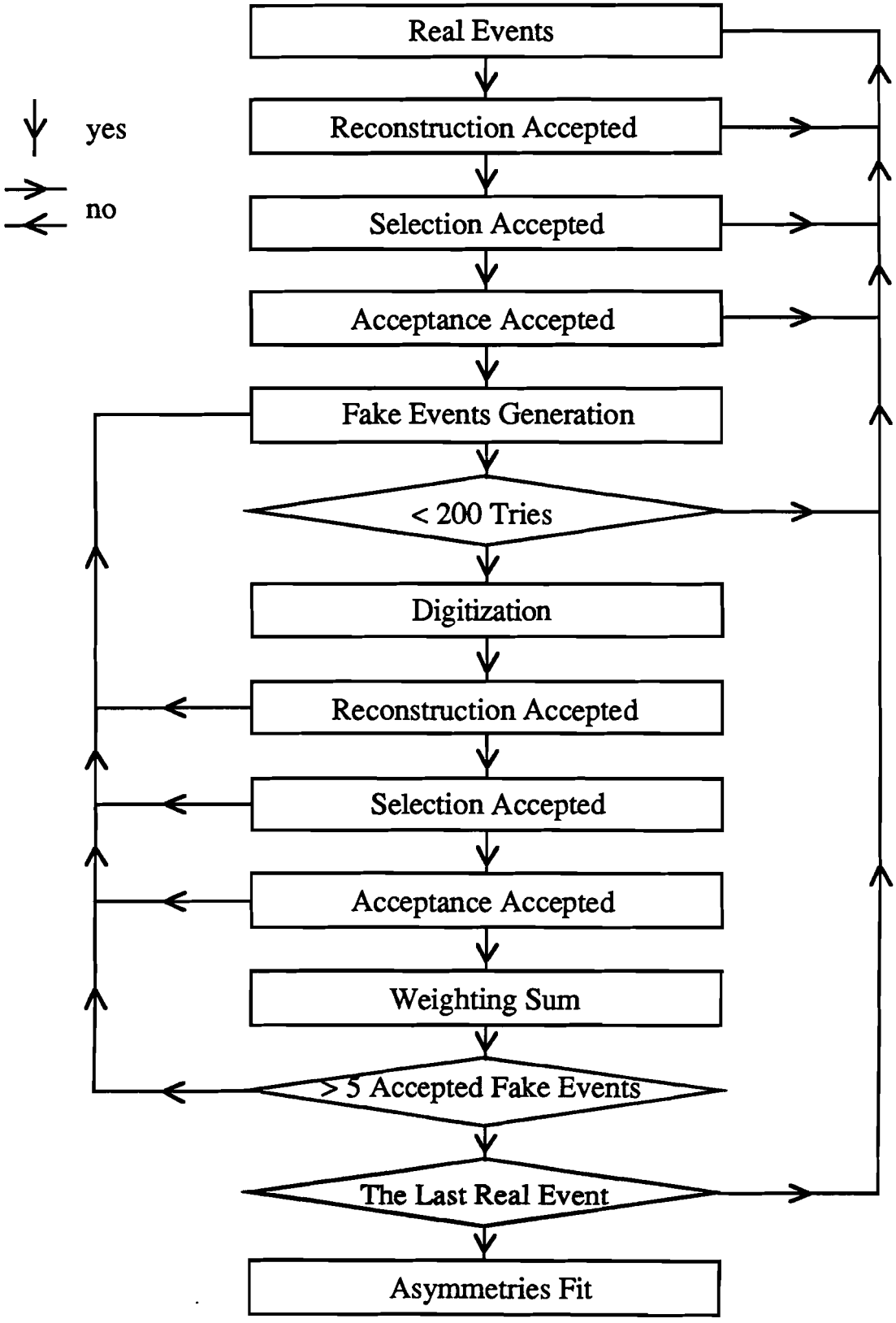

Figure 4.8 Flow chart of the polarization analysis.

4.4.2 Mathematical formalism

A quantitative determination of αP is described as follows. As mentioned previously, $\mathbf{P}_\Xi$ can be determined from $\mathbf{P}_\Lambda$ through Eq. (4.8). But there is a practical difficulty in using this equation because $\mathbf{P}_\Xi$ is unknown and appears in both the numerator and denominator. This makes Eq. (4.8) difficult to use. Since some terms contribute more than the others, as discussed below, this suggests that an iteration method is possible. In the first iteration, $\mathbf{P}_\Xi$ can be related to $\mathbf{P}_\Lambda$ in a simpler form if some approximations are made. In the second iteration, the Ξ polarization, say $\mathbf{P}'_\Xi$, will be used in the smaller terms (treated as perturbative terms) of Eq. (4.8) to determine a new value of the Ξ polarization, say $\mathbf{P}''_\Xi$. In principle, this iteration process can be repeated as many times as we want in order to get the most accurate answer. In practice, $\mathbf{P}_\Xi$ converged very rapidly so that only two iterations were necessary. The results from the first three successive iterations are shown in Chapter 5.

1) First Iteration

In order to relate $\mathbf{P}_\Lambda$ and $\mathbf{P}_\Xi$ in a simple way in the first iteration, two approximations were made to Eq. (4.8)

i) $(1 - \gamma_\Xi)$ term was neglected as $1 - \gamma_\Xi \approx 0.1$

ii) Since the production polarization of all the hyperons is of the order of 0.1 in the same x_F and p_t regions, $\mathbf{P}_\Xi$ was taken to be the same order of magnitude. This implied $|\alpha_\Xi \mathbf{P}_\Lambda \cdot \hat{\mathbf{\Lambda}}| \ll 1$. Thus Eq. (4.8) was reduced to

$$\mathbf{P}_\Lambda = \alpha_\Xi \hat{\mathbf{\Lambda}} + \gamma_\Xi \mathbf{P}_\Xi \tag{4.17}$$

From Eq. (4.17), the component of $\mathbf{P}_\Lambda$ along the ith axis is

$$\begin{aligned} \mathbf{P}_{\Lambda i} &= \mathbf{P}_\Lambda \cdot \hat{i} \\ &= \alpha_\Xi \hat{\mathbf{\Lambda}} \cdot \hat{i} + \gamma_\Xi \mathbf{P}_\Xi \cdot \hat{i} \\ &= \alpha_\Xi \cos\theta_{\Lambda i} + \gamma_\Xi \mathbf{P}_{\Xi i} \end{aligned} \tag{4.18}$$

where $\cos\theta_{\Lambda i}$ is the direction cosine of Λ in the Ξ rest frame along the i axis. Eq. (4.13) can be written as

$$I(\cos\theta_i) = \frac{1}{2}(1 + \alpha_\Lambda P_{\Lambda i}\cos\theta_i) \tag{4.19}$$

where $I(\cos\theta_i)$ is the short form for $dN/d(\cos\theta_i)$, and $\cos\theta_i$ is the direction cosine of the proton in the Λ rest frame, with $i = x, y, z$ axis. Substituting Eq. (4.18) into Eq. (4.19), we have

$$I(\cos\theta_i) = \frac{1}{2}[1 + (\alpha_\Lambda \alpha_\Xi \cos\theta_{\Lambda i} + \alpha_\Lambda \gamma_\Xi P_{\Xi i})\cos\theta_i] \tag{4.20}$$

This is the distribution we want to use to compare the fake and the real events. Since the $\cos\theta$ of fake events were generated randomly, they should show no asymmetry. By requiring $I(\cos\theta_f)$ equal to $I(\cos\theta_r)$, where ' f ' and ' r ' refer to 'fake' and 'real' event respectively, αP_Ξ can be obtained. However, since all the variables except the $\cos\theta$ of the fake events were taken from the real data, the distribution $I(\cos\theta_f)$ might be polarized through the $\cos\theta$ dependence of the apparatus acceptance. Therefore, $I(\cos\theta_f)$ must be weighted by the same distribution factor of the real event to remove the bias before the comparison was made. From Eq. (4.20), a weight

$$W_{jk}(\cos\theta_r) = \frac{1 + (\alpha_\Lambda \alpha_\Xi \cos\theta_{\Lambda i,j} + \alpha_\Lambda \gamma_\Xi P_{\Xi i})\cos\theta_{f,jk}}{1 + (\alpha_\Lambda \alpha_\Xi \cos\theta_{\Lambda i,j} + \alpha_\Lambda \gamma_\Xi P_{\Xi i})\cos\theta_{r,j}} \tag{4.21}$$

was attached to the distribution of the fake event k generated from the real event j. If we define

$$\begin{aligned} A_j &= \alpha_\Lambda \alpha_\Xi \cos\theta_{\Lambda i,j} \\ C_j &= \cos\theta_{r,j} \\ C_{jk} &= \cos\theta_{f,jk} \\ G &= \alpha_\Lambda \gamma_\Xi P_{\Xi i} \end{aligned}$$

then Eq. (4.21) becomes

$$W_{jk} = \frac{1+(A_j+G)C_{jk}}{1+(A_j+G)C_j}$$

$$= \frac{1+(A_j+G)C_{jk}}{(1+A_jC_j)(1+\frac{G}{1+A_jC_j}C_j)} \tag{4.22}$$

Since $x \equiv \left|\frac{G}{1+A_jC_j}\right| < 1$, $(1+x)^{-1}$ can be expanded as a Taylor series. Eq. (4.22) can be written as

$$W_{jk} = \frac{1+A_jC_{jk}}{1+A_jC_j} + \frac{C_{jk}-C_j}{(1+A_jC_j)^2}G - \frac{C_j(C_{jk}-C_j)}{(1+A_jC_j)^3}G^2 + \frac{C_j^2(C_{jk}-C_j)}{(1+A_jC_j)^4}G^3 - \cdots\cdots \tag{4.23}$$

In Eq. (4.23) , the weight W_{jk} was expressed as a power series of the unknown $G=\alpha_\Lambda\gamma_\Xi P_{\Xi i}$, and the coefficients were calculated on an event by event basis. The $W_{jk}(\cos\theta)$ was divided in 20 $\cos\theta$ bins with 0.1 bin width (again, it can be any number of bins). After summing over the sample, the $\cos\theta$ distribution of the fake event sample at the l^{th} $\cos\theta$ bin along the i^{th} axis can be written as,

$$W_l(\cos\theta) = \frac{\sum_{jk} W_{jk,l}(\cos\theta)}{\sum_{jk,l=1,20} W_{jk,l}(\cos\theta)} \tag{4.24}$$

where j is summed over all the real events and k over the 5 fake events. If the number of fake events was normalized to the total number of real events N, and $N = \sum_{l=1,20} N_l$ (N_l is the number of real events in bin l), a χ^2 in each $\cos\theta$ bin could be formed by comparing the number of events in each sample. The χ^2 in the l^{th} bin is

$$\chi^2_l(\mathrm{G}) = \frac{(\mathrm{N}_l - \mathrm{N}\times \mathrm{W}_l)^2}{\mathrm{N}_l} \tag{4.25}$$

The total χ^2 over 20 bins is

$$\chi^2(\mathrm{G}) = \sum_{l=1,20} \chi^2_l(\mathrm{G}) \tag{4.26}$$

Since χ^2 is only a function of the unknown variable $\mathrm{G}=\alpha_\Lambda \gamma_\Xi \mathrm{P}_{\Xi i}$, G is determined by minimizing the χ^2 function, and then $\mathbf{P}_\Xi$ can be determined.

2) Second Iteration

The second order approximation could be carried out as soon as $\mathbf{P}_\Xi$ was determined from the first iteration. Insert $\mathbf{P}'_\Xi$, the first order approximation of $\mathbf{P}_\Xi$, into the small contribution terms of $\mathbf{P}_\Xi$ in Eq. (4.8)

$$\mathbf{P}_\Lambda = \frac{\alpha_\Xi \hat{\mathbf{\Lambda}} + \gamma_\Xi \mathbf{P}_\Xi + (1-\gamma_\Xi)(\mathbf{P}'_\Xi \cdot \hat{\mathbf{\Lambda}})\hat{\mathbf{\Lambda}}}{1+\alpha_\Xi \mathbf{P}'_\Xi \cdot \hat{\mathbf{\Lambda}}} \tag{4.27}$$

and then insert Eq. (4.27) into Eq. (4.19)

$$\mathrm{I}(\cos\theta_i) = \frac{1}{2}\left\{1 + \frac{\alpha_\Lambda \alpha_\Xi \cos\theta_{\Lambda i} + \alpha_\Lambda \gamma_\Xi \mathrm{P}_{\Xi i} + \alpha_\Lambda (1-\gamma_\Xi)\mathbf{P}'_\Xi \cdot \hat{\mathbf{\Lambda}} \cos\theta_{\Lambda i}}{1+\alpha_\Xi \mathbf{P}'_\Xi \cdot \hat{\mathbf{\Lambda}}} \cos\theta_i\right\}$$

$$= \frac{1}{2}\left\{1 + \frac{(1+\frac{1-\gamma_\Xi}{\alpha_\Xi}\mathbf{P}'_\Xi \cdot \hat{\mathbf{\Lambda}})\alpha_\Lambda \alpha_\Xi \cos\theta_{\Lambda i} + \alpha_\Lambda \gamma_\Xi \mathrm{P}_{\Xi i}}{1+\alpha_\Xi \mathbf{P}'_\Xi \hat{\mathbf{\Lambda}}} \cos\theta_i\right\} \tag{4.28}$$

Define

$$\mathrm{R}_i = 1 + \frac{1-\gamma_\Xi}{\alpha_\Xi} \mathbf{P}'_\Xi \cdot \hat{\mathbf{\Lambda}}$$

$$F_i = \frac{1}{1+\alpha_\Xi \mathbf{P}'_\Xi \cdot \hat{\Lambda}}$$

$$A_i = R_i F_i \alpha_\Lambda \alpha_\Xi \cos\theta_{\Lambda i}$$

then

$$I(\cos\theta_i) = \frac{1}{2}\{1 + (A_i + F_i G)\cos\theta_i\} \tag{4.29}$$

Similarly, the weight factor is

$$W_{jk} = \frac{1+(A_j + F_j G)C_{jk}}{1+(A_j + F_j G)C_j}$$

$$= \frac{1+A_j C_{jk}}{1+A_j C_j} + \frac{(C_{jk}-C_j)F_j}{(1+A_j C_j)^2}G - \frac{C_j(C_{jk}-C_j)F_j^2}{(1+A_j C_j)^3}G^2 + \frac{C_j^2(C_{jk}-C_j)F_j^3}{(1+A_j C_j)^4}G^3 - \cdots \tag{4.30}$$

A new $\chi^2(G)$ can be formed in the same way as Eq. (4.25) and (4.26) to extract $G = \alpha_\Lambda \gamma_\Xi P_{\Xi i}$ by minimizing $\chi^2(G)$. As mentioned before, this iteration process can be repeated until P_Ξ converges.

4.5 Biases

In principle, the polarization can be determined from either the positive or negative production angle data set, whereas the naive ratio method requires both data samples. In reality, the measured asymmetries are not necessarily the real polarization signal itself; a false signal called " bias " may appear. The measured asymmetries A can be rewritten as

$$A = B + \alpha_\Lambda \gamma_\Xi P_\Xi \tag{4.31}$$

The bias was due to difficulties in reconstructing events with narrow opening angles (of Λ decay) that were not totally reproduced in the HMC simulation as described earlier. Thus the bias was independent of the production angle. There are two ways to reduce these biases. First, we take advantage of the sign flip of polarization when the production angle is reversed. The asymmetries measured for positive and negative production angle are,

$$A^+ = B + \alpha_\Lambda \gamma_\Xi P_\Xi$$
$$A^- = B - \alpha_\Lambda \gamma_\Xi P_\Xi$$

By taking the difference of A^+ and A^-, $\alpha_\Lambda \gamma_\Xi P_\Xi$ can be extracted, and the bias canceled. By taking the sum of A^+ and A^-, B can be calculated. Therefore,

$$\alpha_\Lambda \gamma_\Xi P_{\Xi i} = \frac{A^+ - A^-}{2} \tag{4.32}$$

$$B = \frac{A^+ + A^-}{2} \tag{4.33}$$

The second way to reduce biases is to cut out the very narrow opening angle events. This cut removed about 3.5% of the accepted events.

4.6 Determination of Magnetic Moment

From Section 1.5, Eq. (1.7), the magnetic moment μ is related to the precession angle as

$$\phi = \frac{2}{\beta}(\mu - \frac{q}{2mc}) \int B dl \tag{4.34}$$

where q and m are the charge and mass of the Ξ respectively, and $\beta = v/c \approx 1$ in this experiment. The precession angle is simply determined by

$$\tan\phi = \frac{\alpha_\Lambda \gamma_\Xi P_{\Xi z}}{\alpha_\Lambda \gamma_\Xi P_{\Xi x}} \tag{4.35}$$

The precession angle measured in this way may not have exactly the same value for different Ξ momentum bins. Since ϕ in Eq. (4.34) does not depend on momentum there should be only one physical precession angle for the entire sample. Therefore we can construct a chi-square function, which is a function of the unknown ϕ, $\alpha_\Lambda \gamma_\Xi P_\Xi$ at target, and x and z biases, to constrain the data in all momentum bins to yield the same ϕ. The chi-square function is

$$\chi^2 = \sum_j \left\{ \frac{\left[A_x(j) - B_x(j) \pm P_0(j)\cos\phi\right]^2}{\sigma_x{}^2(j)} + \frac{\left[A_z(j) - B_z(j) \pm P_0(j)\sin\phi\right]^2}{\sigma_z{}^2(j)} \right\} \tag{4.36}$$

where A and σ are the measured asymmetry and its statistical uncertainty, and j is the index of the momentum bin. The unknown variables in Eq. (4.36) are the polarization at the target P_0, the bias B, and the precession angle ϕ. All the unknowns were determined by minimizing this χ^2 function and then μ was determined by Eq. (4.34). The asymmetries of the y-component (in this experiment) were not included in this fit since it violated parity conservation. The measurement in the y-component was used as a consistent check of the polarization determination. The y-component asymmetry was indeed consistent with zero and will be shown in the next chapter.

CHAPTER 5

RESULTS AND CONCLUSIONS

5.1 Introduction

In this last chapter, the results of the magnetic moments and production polarization are presented based on a sample of 70,000 $\bar{\Xi}^+$ (122,000 Ξ^-). The results from three successive iterations are first given in order to justify the iteration technique of the polarization measurements. The ambiguities of the magnetic moments and polarization are discussed next in detail. Then the final results are presented after the ambiguities are resolved. The systematic uncertainties are also discussed.

It should be emphasized again (see page 20) that the Ξ^- measurements will be an important cross check for the $\bar{\Xi}^+$ results. Therefore, all the measurements in both samples will be presented together for comparison.

5.2 Iterative Results

Since the polarizations were determined from a iteration process, it is important to understand how fast the answers converged. Tables 5.1, 5.2, 5.3 show

the three iterative values of $\alpha_{\bar{\Lambda}}\gamma_{\bar{\Xi}^+}P_{\bar{\Xi}}$. Each table shows the χ^2 (in 19 degrees of freedom) of the polarization fit for the '+' and '-' production angle data, and the biases B_i calculated from the measured asymmetries by Eqs. (4.32) and (4.33) in three momentum bins, where $i = x$, y, and z axis. Similarly, Tables 5.4, 5.5, 5.6 show the same measurements for Ξ^- for two iterations.

In general, the magnitudes of $\alpha_{\bar{\Lambda}}\gamma_{\bar{\Xi}^+}P_{\bar{\Xi}}$ increased by about 0.5% at the second iteration but stayed almost the same at the third iteration. That means that this iteration process converged very fast such that the third iteration was unnecessary. All the results presented from now on are based on two iterations.

5.3 Ambiguities of μ_Ξ and P_Ξ

From Eq. (4.34), μ_Ξ can be calculated if the precession angle, ϕ, is known. However, ϕ is not uniquely determined since, by Eq. (4.35),

$$\phi = \tan^{-1}\left(\frac{\alpha_\Lambda \gamma_\Xi P_{\Xi z}}{\alpha_\Lambda \gamma_\Xi P_{\Xi x}}\right) \tag{5.1}$$

is multiple-valued for a given P_x and P_z. Figure 5.1 shows the four possible ϕ's at the lowest order for a given P_x and P_z, where $\mathbf{P}_{\text{initial}}$ is the polarization at the target (either parallel or anti-parallel to x-axis); $\mathbf{P}_{\text{final}} = P_x\hat{x} + P_z\hat{z}$ is the polarization vector after precession in the hyperons rest frame; $\zeta \equiv \left|\tan^{-1}\left(\frac{\alpha_\Lambda \gamma_\Xi P_{\Xi z}}{\alpha_\Lambda \gamma_\Xi P_{\Xi x}}\right)\right|$ with $\zeta < 90^0$; and "+" and "-" mean the polarization vector precesses "clockwise" and "counter-clockwise" respectively.

$\mathbf{P}_{\text{final}}$ is the same for all cases in Figure 5.1. The polarization vector at the target is anti-parallel to the x-axis in (a) and (b), but parallel to the x-axis in (c) and (d). Since the magnetic moment is directly related to ϕ, there are also four solutions at

1st Iteration

GeV/c	$\alpha_{\bar{\Lambda}}\gamma_{\bar{\Xi}^+}P_x$	B_x	P_x	χ^2 (+)	χ^2 (-)
277	.0537 ± 0.0117	-.0107	-.0940 ± 0.0205	18.7	22.0
312	.0275 ± 0.0110	.0069	-.0481 ± 0.0192	8.5	20.6
358	.0703 ± 0.0112	.0305	-.1231 ± 0.0197	14.3	21.4

2nd Iteration

GeV/c	$\alpha_{\bar{\Lambda}}\gamma_{\bar{\Xi}^+}P_x$	B_x	P_x	χ^2 (+)	χ^2 (-)
277	.0564 ± 0.0117	-.0104	-.0986 ± 0.0205	18.7	22.0
312	.0290 ± 0.0110	.0068	-.0507 ± 0.0192	8.5	20.6
358	.0736 ± 0.0112	.0304	-.1288 ± 0.0197	14.3	21.4

3rd Iteration

GeV/c	$\alpha_{\bar{\Lambda}}\gamma_{\bar{\Xi}^+}P_x$	B_x	P_x	χ^2 (+)	χ^2 (-)
277	.0565 ± 0.0117	-.0104	-.0989 ± 0.0205	18.7	22.0
312	.0290± 0.0110	.0068	-.0508 ± 0.0192	8.5	20.6
358	.0738 ± 0.0112	.0304	-.1291 ± 0.0197	14.3	21.4

Table 5.1 $\alpha_{\bar{\Lambda}}\gamma_{\bar{\Xi}^+}P_x$, B_x and χ^2 for three iterations

1st Iteration

GeV/c	$\alpha_{\bar{\Lambda}}\gamma_{\bar{\Xi}^+}P_y$	B_y	P_y	χ^2 (+)	χ^2 (-)
277	.0049 ± 0.0114	.0096	-.0086 ± 0.0199	30.0	39.2
312	.0078 ± 0.0113	.0052	-.0137 ± 0.0198	23.3	21.7
358	.0129 ± 0.0113	-.0114	-.0226 ± 0.0197	15.9	19.3

2nd Iteration

GeV/c	$\alpha_{\bar{\Lambda}}\gamma_{\bar{\Xi}^+}P_y$	B_y	P_y	χ^2 (+)	χ^2 (-)
277	.0051 ± 0.0113	.0096	-.0089 ± 0.0199	30.0	39.2
312	.0081 ± 0.0113	.0051	-.0141 ± 0.0198	23.3	21.7
358	.0134 ± 0.0113	-.0114	-.0235 ± 0.0197	15.9	19.3

3rd Iteration

GeV/c	$\alpha_{\bar{\Lambda}}\gamma_{\bar{\Xi}^+}P_y$	B_y	P_y	χ^2 (+)	χ^2 (-)
277	.0051 ± 0.0113	.0096	-.0090 ± 0.0199	30.0	39.2
312	.0081 ± 0.0113	.0051	-.0142 ± 0.0198	23.3	21.7
358	.0135 ± 0.0113	-.0114	-.0236 ± 0.0197	15.9	19.3

Table 5.2 $\alpha_{\bar{\Lambda}}\gamma_{\bar{\Xi}^+}P_y$, B_y and χ^2 for three iterations

1st Iteration

GeV/c	$\alpha_{\bar{\Lambda}}\gamma_{\bar{\Xi}^+}P_z$	B_z	P_z	χ^2 (+)	χ^2 (-)
277	-.0021 ± 0.0156	.0065	.0037 ± 0.0272	23.6	37.2
312	-.0304 ± 0.0135	.0209	.0532 ± 0.0237	18.2	36.2
358	-.0154 ± 0.0128	.0532	.0269 ± 0.0224	17.2	31.2

2nd Iteration

GeV/c	$\alpha_{\bar{\Lambda}}\gamma_{\bar{\Xi}^+}P_z$	B_z	P_z	χ^2 (+)	χ^2 (-)
277	-.0026 ± 0.0156	.0065	.0045 ± 0.0272	23.7	37.1
312	-.0316 ± 0.0135	.0211	.0554 ± 0.0236	18.2	36.2
358	-.0161 ± 0.0128	.0532	.0281 ± 0.0223	17.2	31.2

3rd Iteration

GeV/c	$\alpha_{\bar{\Lambda}}\gamma_{\bar{\Xi}^+}P_z$	B_z	P_z	χ^2 (+)	χ^2 (-)
277	-.0026 ± 0.0156	.0065	.0046 ± 0.0272	23.7	37.1
312	-.0317 ± 0.0135	.0211	.0554 ± 0.0236	18.2	36.2
358	-.0161 ± 0.0127	.0532	.0282 ± 0.0223	17.2	31.2

Table 5.3 $\alpha_{\bar{\Lambda}}\gamma_{\bar{\Xi}^+}P_z$, B_z and χ^2 for three iterations

1st Iteration

GeV/c	$\alpha_\Lambda\gamma_\Xi$-P_x	B_x	P_x	χ^2 (+)	χ^2 (-)
283	-.0638 ± 0.0086	-.0056	-.1116 ± .0150	23.4	10.1
323	-.0475 ± 0.0083	.0273	-.0832 ± .0145	18.2	29.2
373	-.0516 ± 0.0085	.0180	-.0904 ± .0149	24.8	20.5

2nd Iteration

GeV/c	$\alpha_\Lambda\gamma_\Xi$-P_x	B_x	P_x	χ^2 (+)	χ^2 (-)
283	-.0670 ± 0.0086	-.0056	-.1173 ± .0150	23.4	10.1
323	-.0499 ± 0.0083	.0273	-.0874 ± .0145	18.1	29.2
373	-.0540 ± 0.0085	.0179	-.0946 ± .0150	24.8	20.5

Table 5.4 $\alpha_\Lambda\gamma_\Xi$-P_x , B_x and χ^2 for two iterations

1st Iteration

GeV/c	$\alpha_\Lambda\gamma_\Xi$-P_y	B_y	P_y	χ^2 (+)	χ^2 (-)
283	-.0018 ± 0.0085	-.0111	-.0032 ± .0150	33.4	30.3
323	.0087 ± 0.0086	.0029	.0153 ± .0150	55.4	16.5
373	.0010 ± 0.0085	.0135	.0018 ± .0150	27.8	34.6

2nd Iteration

GeV/c	$\alpha_\Lambda\gamma_\Xi$-P_y	B_y	P_y	χ^2 (+)	χ^2 (-)
283	-.0018 ± 0.0085	-.0111	-.0032 ± .0149	33.4	30.3
323	.0091 ± 0.0085	.0029	.0158 ± .0150	55.4	16.5
373	.0011 ± 0.0085	.0136	.0019 ± .0150	27.7	34.6

Table 5.5 $\alpha_\Lambda\gamma_\Xi$-P_y, B_y and χ^2 for two iterations

1st Iteration

GeV/c	$\alpha_\Lambda\gamma_\Xi$-P_z	B_z	P_z	χ^2 (+)	χ^2 (-)
283	.0087 ± 0.0115	-.0199	.0153 ± .0202	29.9	14.5
323	.0015 ± 0.0098	.0355	.0027 ± .0171	39.1	29.6
373	.0170 ± 0.0094	.0475	.0298 ± .0164	36.0	32.4

2nd Iteration

GeV/c	$\alpha_\Lambda\gamma_\Xi$-P_z	B_z	P_z	χ^2 (+)	χ^2 (-)
283	.0094 ± 0.0115	-.0199	.0165 ± .0201	29.9	14.6
323	.0019 ± 0.0098	.0354	.0033 ± .0171	39.1	29.7
373	.0178 ± 0.0094	.0476	.0312 ± .0164	36.0	32.4

Table 5.6 $\alpha_\Lambda\gamma_\Xi$-P_z , B_z and χ^2 for two iterations

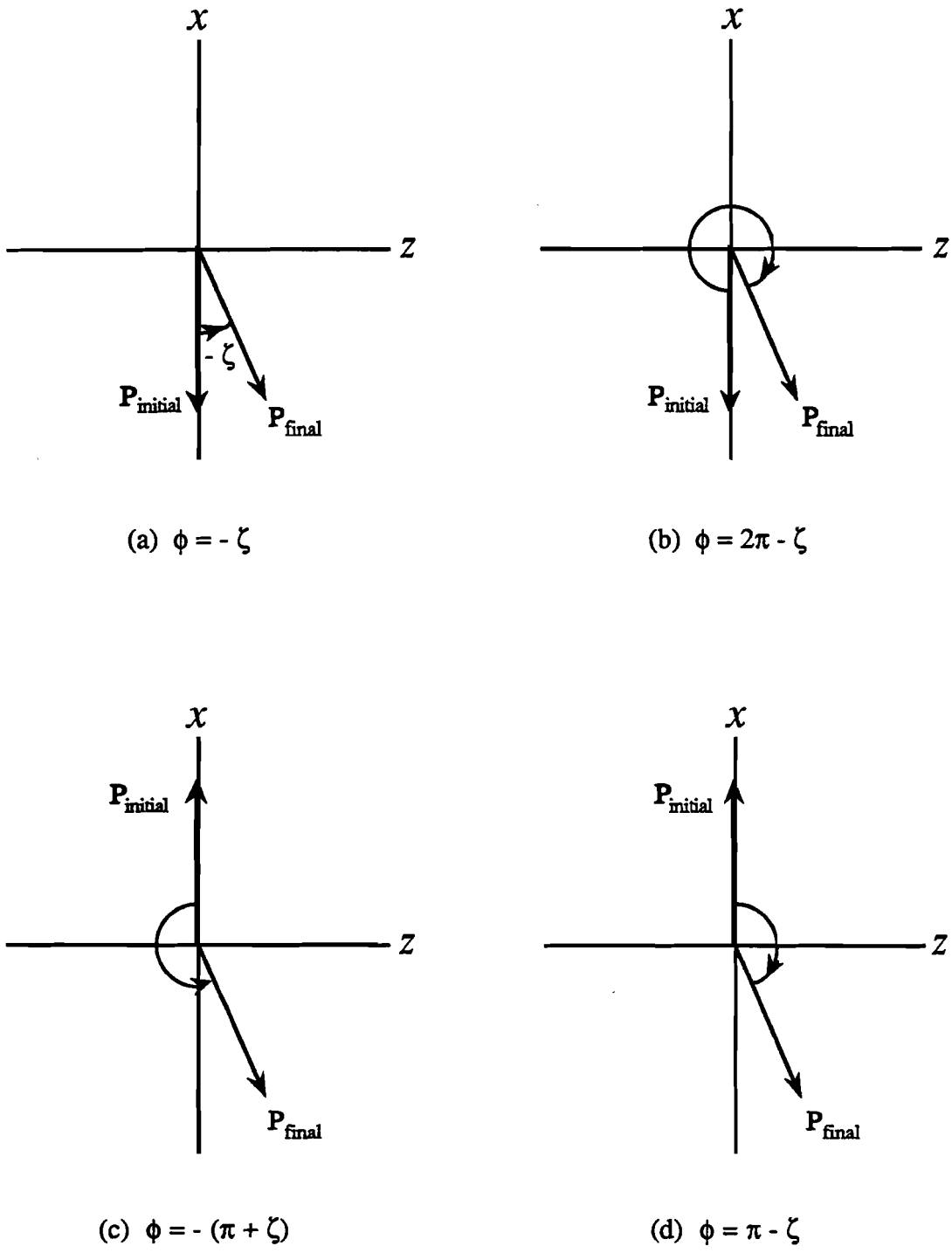

Figure 5.1 Four lowest order solutions of possible angle ϕ for given P_x and P_z.

the lowest order. This ambiguity can be resolved uniquely if data is taken at more than one field integral ∫Bdl, since the precession angles are different for different fields but the magnetic moment is not. This can be used to fix the polarization at the target uniquely.

Since the $\bar{\Xi}^+$ data were taken only at one ∫Bdl, the ambiguity could not be resolved. However, its magnetic moment can be determined by applying a more stringent constraint to be described later.

5.4 μ_Ξ and P_Ξ results

The four lowest-order magnetic moments for $\bar{\Xi}^+$ and Ξ^- were obtained by using a χ^2 fit of Eq. (4.36), and are listed in Table 5.7. Figures 5.2 and 5.3 show the corresponding polarization for Table 5.7.

$\phi_{\bar{\Xi}^+}$ (degree)	$\mu_{\bar{\Xi}^+}$ (n.m.)	ϕ_{Ξ^-} (degree)	μ_{Ξ^-} (n.m.)
-14.8	0.657	-9.9	-0.674
345.2	1.938	350.1	-1.960
-194.8	0.014	-189.9	-0.032
165.2	1.295	170.1	-1.317

n. m. = nuclear magneton

Table 5.7 Four lowest-order solutions of the magnetic moment for the $\bar{\Xi}^+$ and Ξ^-.

The magnetic moment of Ξ^- was taken to be -0.674 ± 0.021 n.m. since this is the one closest to the two previous measurements,[9,24] which were -0.69±0.04±0.02 and -0.670±0.036±0.036 n.m. In the case of $\mu_{\bar{\Xi}^+}$, the solution with $\mu_{\bar{\Xi}^+}$ closest to $-\mu_{\Xi^-}$ was chosen since the CPT theorem requires the magnetic moment of the particle and

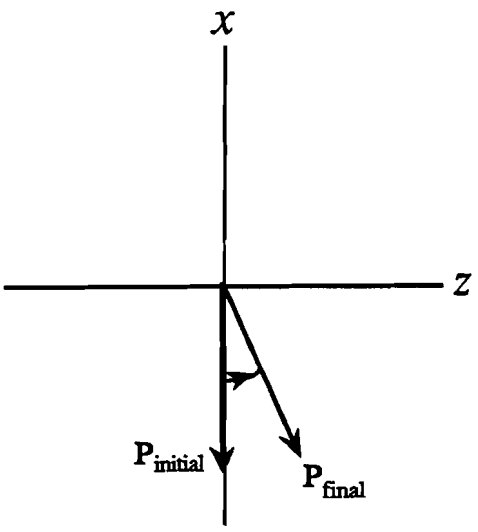

(a) $\mu_{\Xi^-} = -0.674$

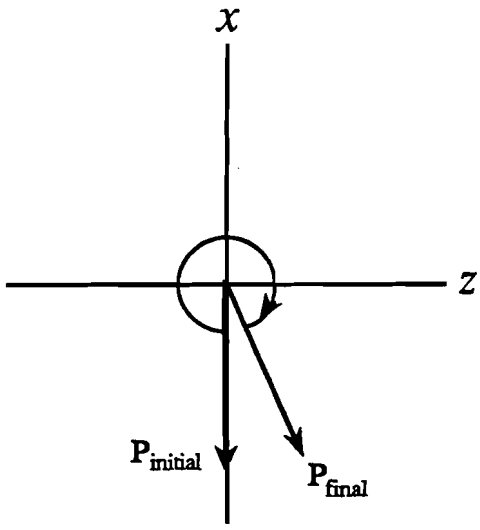

(b) $\mu_{\Xi^-} = -1.960$

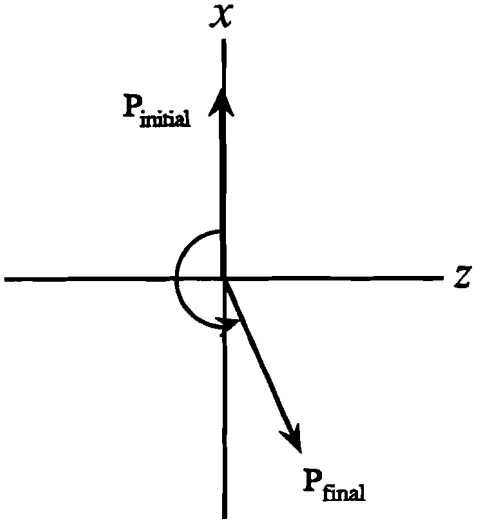

(c) $\mu_{\Xi^-} = -0.032$

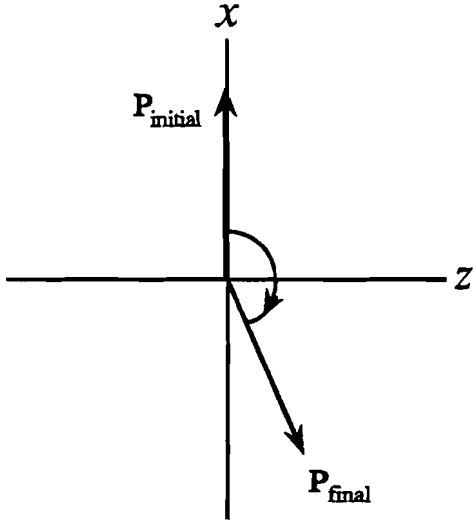

(d) $\mu_{\Xi^-} = -1.317$

Figure 5.2 Four lowest order solutions of possible μ_{Ξ^-}.

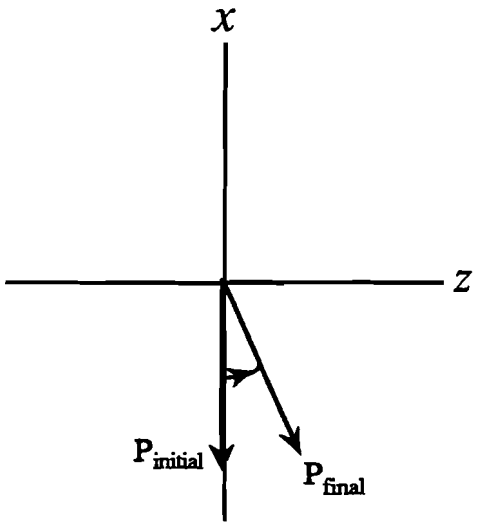

(a) $\mu_{\Xi^+} = 0.657$

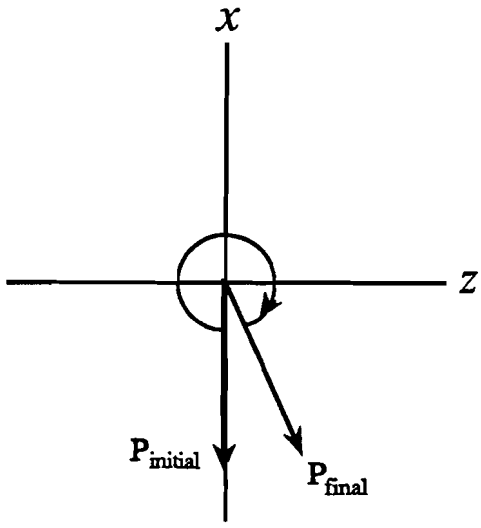

(b) $\mu_{\Xi^+} = 1.938$

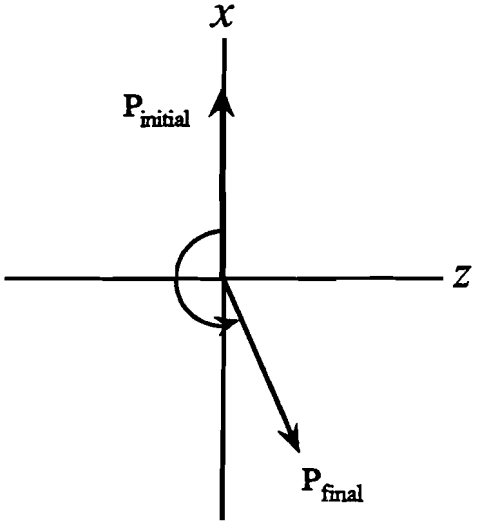

(c) $\mu_{\Xi^+} = 0.014$

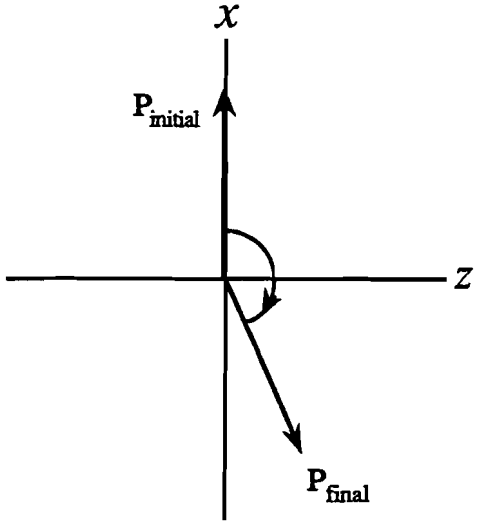

(d) $\mu_{\Xi^+} = 1.295$

Figure 5.3 Four lowest order solutions of possible μ_{Ξ^+}.

its anti-particle to have the same magnitude but opposite sign. Therefore, the most reasonable choice of $\mu_{\bar{\Xi}^+}$ was -0.657 ± 0.028 n.m.

Once the magnetic moment was fixed, the sign of the polarization at the target was also determined as can be seen in Figures 5.2 and 5.3. Table 5.8 (a) and (b) show all the fitted parameters by using the χ^2 fit of Eq. (4.36) for $\bar{\Xi}^+$ and Ξ^-.

(a) $\bar{\Xi}^+$

GeV/c	B_x	B_z	$\alpha_{\bar{\Lambda}}\gamma_{\bar{\Xi}^+}P_{\bar{\Xi}^+}$	$P_{\bar{\Xi}^+}$
277	-0.011 ± 0.012	0.005 ± 0.016	0.057 ± 0.012	-0.099 ± 0.021
312	0.007 ± 0.011	0.023 ± 0.014	0.034 ± 0.011	-0.060 ± 0.020
358	0.030 ± 0.011	0.053 ± 0.013	0.076 ± 0.011	-0.132 ± 0.020

(b) Ξ^-

GeV/c	B_x	B_z	$\alpha_{\Lambda}\gamma_{\Xi^-}P_{\Xi^-}$	P_{Ξ^-}
283	-0.005 ± 0.009	-0.020 ± 0.012	-0.068 ± 0.009	-0.119 ± 0.015
323	0.027 ± 0.008	0.035 ± 0.010	-0.050 ± 0.008	-0.087 ± 0.015
373	0.018 ± 0.009	0.048 ± 0.010	-0.056 ± 0.009	-0.098 ± 0.015

Table 5.8 Fitted parameters in the χ^2 fit for (a) $\bar{\Xi}^+$ (b) Ξ^- sample in three momentum bins.

The chi-square of the fits were 3.6 per 2 degrees of freedom for the $\bar{\Xi}^+$ sample and 1.2 for the Ξ^- sample (since there were 12 data points and 10 unknown variables, which were 6 biases, 3 polarization at target and one precession angle).

The biases, the *y*-component of the polarization, and the polarization at target over the whole sample are shown in Table 5.9 (a) and (b) for $\bar{\Xi}^+$ and Ξ^- respectively.

The polarization along the y-axis were measured consistent with zero as expected by parity conservation.

	GeV/c	P_y	P_{tgt}
$\bar{\Xi}^+$	315.1	-.016 ± 0.011	-.097 ± 0.012
Ξ^-	325.5	0.005 ± 0.009	-0.102 ± 0.010

	B_x	B_y	B_z
$\bar{\Xi}^+$	0.009 ± 0.007	0.001 ± 0.007	0.030 ± 0.008
Ξ^-	0.013 ± 0.005	0.002 ± 0.005	0.026 ± 0.006

Table 5.9 (a) polarization of y-component and at target (b) Bias in x, y and z axis for $\bar{\Xi}^+$ and Ξ^- over the whole sample.

Figure 5.4 shows the comparison of the polarization of the Ξ^- and the previous Ξ^- results at 400 GeV/c and a production angle of 5 mrad. In general, comparisons must be made by matching both x_F and p_t as polarization depends on both parameters. In Figure 5.4, events from each data set have approximately the same x_F at a given p_t since the production angle of the 400 GeV/c data is almost twice that of the 800 GeV/c data (the production angle is 2.4 mrad for the $\bar{\Xi}^+$ and Ξ^- data). The polarization of the Ξ^- in this experiment is seen to be consistent with that of the Ξ^- results at 400 GeV/c.

Systematic uncertainties in the polarization and the magnetic moment measurements were estimated by studying the change in the results when software cuts were varied. By far, the largest uncertainty, comparable to the statistical uncertainty, came from varying the cut on the Λ decay angle. The systematic uncertainties were estimated to be 0.01 for the polarization and 0.02 n.m. for μ_Ξ .

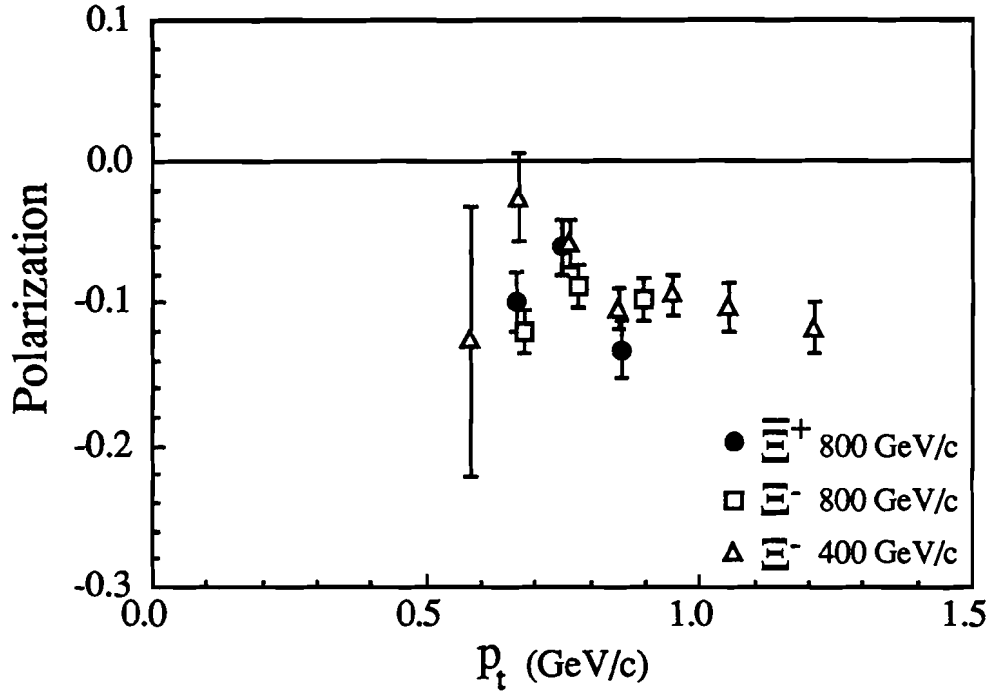

Figure 5.4 Comparison of the $\bar{\Xi}^+$ and Ξ^- polarization from this experiment with that of the Ξ^- data at 400 GeV/c and a production angle of 5 mrad.[7]

5.6 Conclusion

We have found that $\bar{\Xi}^+$'s produced by 800 GeV/c protons were polarized with an average polarization of

$$P_{\bar{\Xi}^+} = -0.097 \pm 0.012 \pm 0.009 \qquad \text{at } \langle x_F \rangle = 0.39,\ \langle p_t \rangle = 0.76 \text{ GeV/c}.$$

For comparison, the Ξ^- polarization was measured to be

$$P_{\Xi^-} = -0.102 \pm 0.012 \pm 0.010 \qquad \text{at } \langle x_F \rangle = 0.41,\ \langle p_t \rangle = 0.78 \text{ GeV/c}.$$

The significant polarization of $\bar{\Xi}^+$ definitely differs from the present understanding of the production polarization of hyperons produced by protons. It

indicates that spin effects cannot be ignored at high energy. Both $\bar{\Xi}^+$ and Ξ^- have negative polarizations and, within uncertainties, the magnitudes are equal disregarding their production mechanism. The agreement of the Ξ^- polarization at 400 and 800 GeV/c suggests that polarization is scaled with energy. Other results[12] also indicated that polarization did not vanish up to $p_t \leq 4$ GeV/c. It is a challenge to the perturbative QCD prediction,[29] which suggested that polarization would die out at high p_t, around $4 \sim 5$ GeV/c.

It is also obvious that polarization is not just a leading particle effect since there is no common quark between the $\bar{\Xi}^+$ and proton. None of the model mentioned in section 1.4 predicts the polarization of $\bar{\Xi}^+$. Even though these models may be modified to explain the $\bar{\Xi}^+$ polarization, it will be a new challenge to these models to invent a mechanism that will generate a polarized $\bar{\Xi}^+$ but not the $\bar{\Lambda}$ in the proton-nucleon interaction.

Due to the contrasting polarization results of the $\bar{\Xi}^+$ and $\bar{\Lambda}$, it will be very interesting to study the production polarization of $\bar{\Sigma}^+$ and $\bar{\Omega}^+$. As far as isospin is concern, Λ's and Ω's are singlet, Ξ's are doublet, and Σ's are triplet, polarization may be related to the hyperon's isospin since the production polarization is a product of strong interactions.

In addition, the observed $\bar{\Xi}^+$ polarization allows us to make the first measurement of the $\bar{\Xi}^+$ magnetic moment, and we obtained

$$\mu_{\bar{\Xi}^+} = 0.657 \pm 0.028 \pm 0.020 \text{ nuclear magnetons.}$$

For comparison, the Ξ^- magnetic moment was measured to be

$$\mu_{\Xi^-} = -0.674 \pm 0.021 \pm 0.020 \text{ nuclear magnetons.}$$

The nearness of the two measurements is in good agreement with the requirement of CPT invariant. There is still about $20 \sim 30$ % discrepancy in the Ξ^-

magnetic moment between the experimental values and the various theoretical predictions.[30-32]

REFERENCES

1. G. Bunce *et al.*, Phys. Rev. Lett. **36**, 1133 (1976).
2. C. Wilkinson *et al.*, Phys. Rev. Lett. **46**, 803 (1981).
3. C. Ankenbrandt *et al.*, Phys. Rev. Lett. **51**, 863 (1983).
4. K. Heller *et al.*, Phys. Rev. Lett. **51**, 2025 (1983).
5. L. Deck *et al.*, Phys. Rev. **D28**, 1 (1983).
6. Y. W. Wah *et al.*, Phys. Rev. Lett. **55**, 2551 (1985).
7. R. Rameika *et al.*, Phys. Rev. **D33**, 3172 (1986).
8. E. C. Dukes *et al.*, Phys. Lett. **193B**, 135 (1987).
9. L. H. Trost *et al.*, Phys. Rev. **D40**, 1703 (1989).
10. K. Heller *et al.*, Phys. Rev. Lett. **41**, 607 (1978).
11. F. Lomanno *et al.*, Phys. Lett. **96B**, 223 (1980).
12. B. Lundberg *et al.*, Phys. Rev. **D40**, 3557 (1989).
13. R. Rameika *et al.*, "Search for Polarization in $\bar{\Xi}^{o}$ Hyperons", in High Energy Spin Physics, 126 (1982), AIP Proceedings of the 8th International Symposium.
14. B. Andersson, G. Gustafson, and G. Ingelman, Phys. Lett. **85B**, 417 (1979).
15. T. DeGrand and H. I. Miettinen, Phys. Rev. **D23**, 1227 (1981), Phys. Rev. **D24**, 2419 (1981).
16. J. Szwed, Phys. Lett. **105B**, 403 (1981).
17 F. E. Paige, and D. P. Sidhu, Phys. Rev. **D14**, 2307 (1976).
18. V. Bargmann, L. Michal and V. L. Telegdi, Phys. Rev Lett. **2**, 435 (1959).
19. L. Schachinger *et al.*, Phys. Rev. Lett. **41**, 1348 (1978).
20. G. Zapalac *et al.*, Phys. Rev. Lett. **57**, 1526 (1986).
21. C. Wilkinson *et al.*, Phys. Rev. Lett. **58**, 855 (1987).
22. G. Bunce *et al.*, Phys. Lett. **86B**, 386 (1979).
23. P. T. Cox *et al.*, Phys. Rev. Lett. **46**, 877 (1981).

24. R. Rameika *et al.*, Phys. Rev. Lett. **52**, 581 (1984).

25. Particle Data Group. M. Aguilar-Benitez *et al.*, Phys. Lett. **170B**, 154 (1986).

26. Particle Data Group. G.P. Yost *et al.*, Phys. Lett. **204B**, 1 (1988).

27. T. D. Lee, Prelude in Theoretical Physics, p.5 (1966).

28. G. Bunce, Nucl. Instrum. Methods **172**, 553 (1980).

29. G. L. Kane, J. Pumplin and W. Repko, Phys. Rev. Lett. **41**, 1689 (1978).

30. A. De Rujula, Howard Georgi, and S. L. Glashow, Phys. Rev. **D12**, 147 (1975).

31 Joesph Cohen and H. J. Weber, Phys. Lett. **165B**, 229 (1985).

32 B. L. Ioffe and A. V. Smilga, Phys. Lett. **133B**, 436 (1983).